Universidade de São Paulo
Instituto de Astronomia, Geofísica e Ciências Atmosféricas
Departamento de Astronomia

Pedro Henrique Cezar Remião de Macedo

The many faces of the Seyfert galaxy NGC 5643

São Paulo
2022

Pedro Henrique Cezar Remião de Macedo

The many faces of the Seyfert galaxy NGC 5643

Thesis presented to the Department of Astronomy of the Instituto de Astronomia, Geofísica e Ciências Atmosféricas of the Universidade de São Paulo as a partial requirement to obtain a Master of Science degree.

Corrected version. The original version is available at the Unit.

Research field: Astronomy
Advisors : Prof. Dr. João E. Steiner,
Prof. Dr. Rodrigo Nemmen da Silva

São Paulo

2022

In memory of João Evangelista Steiner,

Acknowledgements

Primeiramente, agradeço à Natureza pela oportunidade de estar vivo e me sentir mais vivo ainda ao vislumbrar a sua beleza.

Agradeço a minha família pelo apoio e compreensão. Principalmente a minha mãe Neiva e minha avó Inês, que nunca desacreditaram a minha jornada.

Agradeço ao meu orientador, João Evangelista Steiner por confiar a mim esse projeto, me orientar e me inspirar. Agradeço também a oportunidade das monitorias nas suas disciplinas de "Astronomia - Uma Visão Geral". Eu cresci muito nesse tempo. Agradeço ao meu orientador Rodrigo Nemmen por ter me acolhido em seu grupo de pesquisa, me orientado e mentorado na pesquisa e na vida acadêmica. Seu apoio foi fundamental. Aproveito para agradecer aos membros do Grupo de Buracos Negros da USP, pelo acolhimento e apoio, em especial ao Fábio Cafardo, Ivan Almeida, Roberta Duarte e Raniere de Menezes. Agradeço imensamente o apoio e a orientação dos membros do grupo de pesquisa do meu orientador, João Steiner, que lideram o $DIVING^{3D}$ survey. A orientação de vocês foi essencial para que eu seguisse nesse projeto e hoje possa defendê-lo. Agradeço a Tiago Vecchi Ricci pela suas ideias, *feedbacks*, orientação e mentoria. A Roberto Bertoldo Menezes as diversas ajudas e apoio na pesquisa e na vida acadêmica. A Daniel May as ideias, apoio e momentos de descontração. A Patrícia da Silva pelas suas ideias, *feedbacks* e em especial a revisão desse manuscrito, agradeço de coração. A Catarina Aydar por me receber na USP, pela parceria nas disciplinas e na pesquisa, por todo apoio e ajuda nos momentos difíceis.

Agradeço também a outros pesquisadores que também foram essenciais nessa minha jornada. A Roderik Overzier pelas suas ideias e mentoria, direcionamentos na pesquisa e na vida acadêmica, apoio nos momentos difíceis e suas aulas sobre AGNs.

A Laerte Sodré Júnior pelos direcionamentos e apoio na pesquisa e na vida acadêmica. Agradeço a Victoria Reynaldi pela sua disponibilidade, apoio, ideias sobre a pesquisa e a vida, e sua colaboração. A Alberto Rodríguez Ardila pelas nossas conversas e ideias sobre a pesquisa. A Oli Dors pelo seu apoio, ideias e aulas. Agradeço o apoio e troca de ideias às e aos pesquisadores Daniel Ruschel Dutra, Natália Vale Asari, Cristina Ramos Almeida, David Rosario, Claudia Mendes de Oliveira, Beatriz Barbuy, Thaisa Storchi Bergmann, Richard Davies, Rogemar Riffel, David Williams, Darshan Kakkad, Rebecca Davies, Travis Fischer, Françoise Combes e Nadine Neumayer.

Agradeço também aos meus orientadores, mentores e colaboradores que tive durante a minha graduação na UFRGS. A Miriani Pastoriza agradeço pela sua orientação, ideias e mentoria. A Rogério Riffel pelo suas aulas, sua orientação e mentoria, e seu apoio na pesquisa e na vida acadêmica. Agradeço também às e aos pesquisadores Eduardo Luiz Damiani Bica, Marcia Bernardes Barbosa, Alan Alves Brito, Dinalva Aires de Sales, Charles Bonatto, Sandro Rembold, José Hernandez-Jimenez, Angela Krabbe, Ana Chies Santos e Adriano Pieres.

Agradeço aos meus professores no mestrado que contribuíram demais para o meu *background* em astronomia. Agradeço à Silvia Rossi, Reinaldo Santos de Lima, Alessandro Ederoclite, Sagi Ben-Ami, Rodrigo Nemmen, João Steiner e Roderik Overzier. Agradeço especialmente ao Gastão Bierrenbach Lima Neto, pelas suas aulas inspiradoras de Extragaláctica, seu apoio e a oportunidade de ter sido seu monitor na disciplina de "Astronomia - Uma Visão Geral II".

Agradeço ao apoio do Departamento de Astronomia, ao Instituto de Astronomia, Geofísica e Ciências Atmosféricas (IAG) e a Universidade de São Paulo por essa oportunidade única que me foi dada. Agradeço o apoio da Comissão Coordenadora de Programa de Astronomia (CCP), a Comissão de Pós-Graduação (CPG) e demais comissões do IAG. Agradeço ao corpo técnico e administrativo do IAG, em especial as diversas ajudas que recebi de Gislene Yoko, Daniel Bigardi, Ligia Marques, Rosely Sousa, Luciana Silveira, Marcel Kimura, Edna Diniz, Richard Lingner e Sylvia Del Nero. Agradeço ao apoio financeiro da CAPES durante o meu mestrado. Agradeço a USP e a UFRGS por serem as minhas casas, lugares que eu quero trabalhar e retornar sempre que possível.

Os meus amigos são a minha sustentação. Agradeço imensamente a parceria de vocês. Sou extremamente grato em especial à Catarina Aydar, Guilherme Limberg, Thainá

Sabino, Jhon Yana, Natália Crepaldi, Thayse Pacheco e Júlia Santos. Vocês me salvam demais pessoal. Agradeço ao Geraldo Gonçalves e a Roberta Duarte por terem me apresentado as músicas da Taylor Swift. Agradeço as conversas sobre a vida e a Natureza, André Figueiredo. E por sanar as minhas inúmeras dúvidas de filosofia, Jullian Santos. A pandemia pode ter dificultado nosso convívio, mas amei a oportunidade de conhecer todos vocês. Agradeço imensamente também as minhas amizades, sempre tão presentes, que começaram nos meus tempos de UFRGS. Afinal, eu não estaria aqui sem eles. Em especial gostaria de agradecer à Tuila Ziliotto, Leonardo Pessoa, Vinícius Bernardes, Larissa Antunes, Danielle Reppold, Geovane Naysinger, Mônica Tergolina, João Pedro Benedetti, Rodrigo Freitas e Roberta Razera. Muito obrigado por fazerem parte da minha história, e espero que continuem fazendo parte do meu futuro.

Por fim, agradeço a banca avaliadora pelos valorosos comentários que, tenho certeza, contribuirão muito para a continuidade desse trabalho.

Esta tese/dissertação foi escrita em LaTeX com a classe IAGTESE, para teses e dissertações do IAG.

"*We all change, when you think about it. We're all different people all through our lives. And that's OK, that's good, you gotta keep moving, so long as you remember all the people that you used to be.*"

The Doctor

"*You wait a moment, Doctor. Let's get it right. I've got a few things to say to you.*
Basic stuff first.
Never be cruel, never be cowardly. And never ever eat pears!
Remember – hate is always foolish... and love, is always wise.
Always try, to be nice and never fail to be kind. Oh, and....and you mustn't tell anyone your name. No-one would understand it anyway. Except....
Except....children. Children can hear it. Sometimes – if their hearts are in the right place, and the stars are too. Children can hear your name.
But nobody else. Nobody else. Ever.
Laugh hard. Run fast. Be kind.
Doctor – I let you go."

The Doctor

Resumo

Realizamos uma análise detalhada dos 350 parsecs centrais da galáxia NGC 5643. Nosso objetivo foi investigar as condições e mecanismos por trás da emissão do gás. Para isso, foram analisados dados de espectroscopia de campo integral de alta resolução espacial no óptico e infravermelho próximo. A maior parte da emissão de gás ionizado é observada ao longo de uma estrutura de bicone de ionização. O [Fe II]λ16440, menos obscurecido pela poeira, revelou os cones até suas bordas. O gás ionizado apresenta alta extinção principalmente para o lado oeste onde atinge até Av $\approx$ 4.4 magnitudes. A estrutura de poeira provavelmente está associada a um anel molecular de gás alimentado pela espiral circumnuclear. Para nordeste, onde a extinção cai, o cenário favorece os cones de ionização estarem inclinados em relação ao disco galáctico. Obtivemos estimativas de temperatura eletrônica com valores em torno de $T_e \approx 10^4$ K. As densidades eletrônicas apresentaram seus maiores valores para o lado oeste, onde se mantiveram tão altas quanto a densidade nuclear de $n_e \approx 1200\ cm^{-3}$ até $\approx 0.5''$. A cinemática da componente Gaussiana estreita de Hα apresentou estruturas semelhantes ao H_2, sugerindo que ambos podem ser quase co-espaciais e emitidos mais próximos do disco galáctico. Encontramos parte da cinemática da componente estreita associada a *outflows* de baixa velocidade, também observados na fase molecular quente. O *outflow* é proeminente na direção nordeste-sudoeste, atingindo FWHM $\leq$ 476 km/s. *Outflows* de alta velocidade foram frequentemente encontrados em *blueshift*, associados às bordas do cone leste e na região interna do cone oeste, alcançando FWHM $\leq$ 926 km/s. Encontramos o AGN como a fonte primária de ionização. No entanto, [Fe VII]λ6086/Hβ apresentou altas razões fora do núcleo, sugerindo a presença de *fast shocks*. Essas regiões foram encontradas alinhadas ao jato em rádio e na direção de emissão ionizada associada a *outflows*. Esses resultados sugerem que o jato em rádio está

potencialmente alterando a ionização e a cinemática da região central da galáxia. Estudos detalhados no Universo local, como o atual, nos fornecem mais evidências de como os fenômenos associados a AGNs impactam o gás das galáxias.

Abstract

We carried out a detailed analysis of the central 350 pc of the galaxy NGC 5643. We aimed to probe the conditions and mechanisms behind the gas emission. For that, high spatial resolution optical and near-infrared integral field spectroscopy data were analyzed. Most of the ionized gas emission is seen across an ionization bicone structure. The [Fe II]λ16440, less obscured by dust, revealed the cones until their walls. The ionized gas presents high extinction mainly towards the west side, reaching up to Av $\approx$ 4.4 magnitudes. The dust structure is probably associated with a molecular gas ring fed by the circumnuclear spiral. Towards the northeast, where extinction drops, the favored scenario is the ionization cones tilted relative to the galaxy disc. We obtain electron temperature estimates that show values around $T_e \approx 10^4$ K. Electron densities present their highest values towards the west side, where their values maintain as high as the nuclear density of $n_e \approx 1200\ cm^{-3}$ until $\approx 0.5''$. From the kinematics, the narrow Gaussian component of Hα presents similar structures as H_2, suggesting that both can be almost co-spatial and closer to the galaxy disc. We found part of the narrow component kinematics associated with low-velocity outflows, also seen in the hot molecular phase. The outflow is prominent across the northeast-southwest direction, reaching up to FWHM $\leq$ 476 km/s. High-velocity outflows were often found in blueshift, associated with the eastern cone edges and in the inner region of the west cone, reaching up to FWHM $\leq$ 926 km/s. We found the AGN as the primary ionization source. However, [Fe VII]λ6086/Hβ presented high ratios outside the nucleus, suggesting the presence of fast shocks. These regions were found aligned with the radio jet and in the direction of ionized gas emission tracing outflows. These results suggest that the radio jet is potentially changing the ionization and kinematics of the central region of the galaxy. Detailed studies in the nearby Universe, as the current,

provide further evidence of how AGN-driven phenomena impact the gas of galaxies.

List of Figures

List of Tables

Contents

Chapter 1

Introduction

1.1 Active Galactic Nucleus (AGN)

Nuclear regions of galaxies are unique places in the Universe because they contain information on the origin and evolution of galaxies. When the spectra of the nuclear regions present gas emission with excitation of non-stellar origin, we say that the galaxy has an Active Galactic Nucleus (AGN). The active nuclei are very compact sources. Studies about their variability indicate that their radiation is produced in scales of milliparsecs, being unresolved by current optical telescopes (Padovani et al., 2017). Such radiation extends across all electromagnetic spectrum, from radio to γ-rays (Almeida and Ricci, 2017). AGNs can achieve high luminosities, up to $L_{bol} \approx 10^{48} erg/s$, being the most powerful persistent phenomena in the Universe (Padovani et al., 2017). These unusual energy ranges and power in such compact regions cannot be explained in terms of theirs stellar populations. Despite their differences, AGNs are explained physically by the accretion of matter to supermassive black holes (SMBHs, $M_{BH} \geq 10^6 M_{\odot}$, Padovani et al. 2017).

AGNs display a great diversity of observational signatures beyond the already mentioned, which led to different classes. Broadly speaking, we can classify them in terms of their bolometric luminosity and the ionization degree of their emission lines. Seyferts (10^{42} erg/s $\leq L_{bol} < 10^{45}$ erg/s) and Quasars ($L_{bol} \geq 10^{45}$ erg/s, Hickox and Alexander 2018) are examples of AGNs with intermediate to high luminosities and ionization degrees. On the other hand, the Low Ionization Nuclear Emission-Line Regions (LINERs) are examples of low-luminosity AGNs with a mean bolometric luminosity of $L_{bol} \approx 10^{41}$ erg/s (Ho, 2009) and low ionization levels. Also, AGNs can be classified according to the presence of broad permitted emission lines (Type 1, FWHM $>$ 1000 km/s) or just narrow

emission lines (Type 2, FWHM $<$ 1000 km/s, Khachikian and Weedman 1974; Netzer 2015). Another sign of an active nucleus is the presence of jets, usually very collimated, straight radio emitters. In the presence of powerful jets, we classify them as radio-loud; otherwise, they are called radio-quiet.

Most of the energy in an AGN is produced by the accretion flow, where the gravitational potential energy released by the spiraling gas is converted into radiation (Netzer, 2013, Section 7.8). The mass accretion rate $\dot{M} = \frac{L}{\eta c^2}$, where η is the mass-to-luminosity conversion efficiency, is a fundamental quantity correlated to the power observed, more specifically to the Eddington ratio $\lambda = \frac{L_{Bol}}{L_{Edd}}$ (Netzer, 2013, Section 3.3.1). In other words, more luminous AGNs are accreting faster at a given SMBH mass. Seyferts and Quasars ($L_{Bol}/L_{Edd} \geq 0.01$, Netzer 2015) are examples of SMBHs accreting at high $\dot{M}$ and LINERs at low $\dot{M}$ ($L_{Bol}/L_{Edd} < 0.01$).

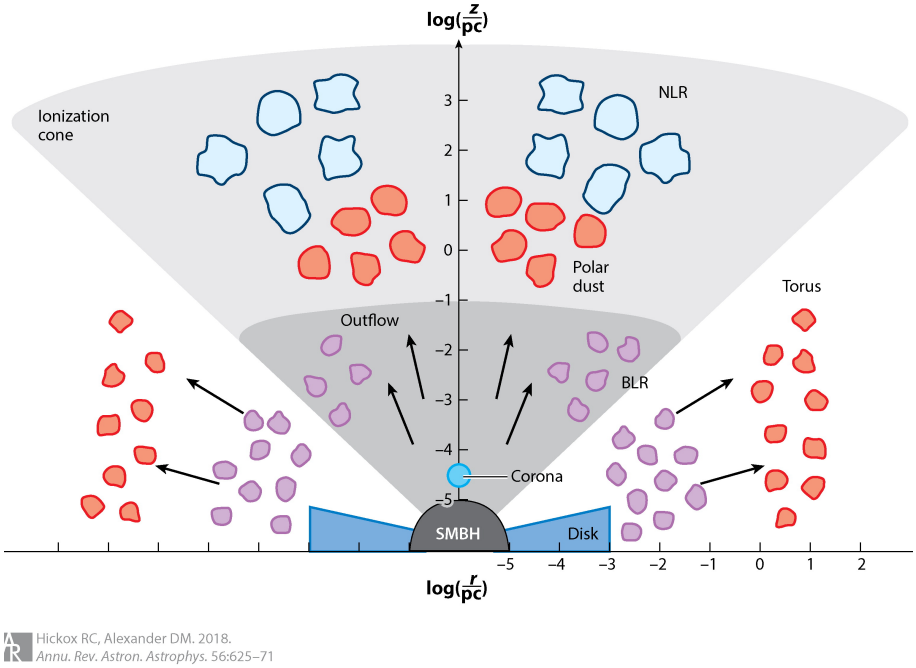

Figure 1.1: Schematic representation of the main AGN structures and physical scales taken from Hickox and Alexander (2018) that adapted the original plot from Almeida and Ricci (2017).

Active nuclei are complex systems, covering different phases (e.g., molecular gas, dust, ionized gas) , kinematics and can impact from sub-parsec scales up to hundreds of kilo-parsecs (Heckman and Best, 2014). A sketch is shown in figure 1.1 labeling some of the main structures. Closer to the SMBH, the accretion disk is responsible for most energy production. Yet at typical sub-parsec scales, gas clouds have keplerian rotation around the

SMBH, broadening the permitted emission lines at FWHM $>$ 1000 km/s in the region called broad-line region (BLR). Still under the sphere of influence of the SMBH [1] a dusty torus, made of cool molecular gas and dust, absorbs a significant part of the continuum and reemits in the Mid-infrared (MIR). The torus does not cover all solid angles. The radiation that scapes can photoionize clouds in the narrow-line region (NLR), reaching hundreds up to thousands of parsecs away from the SMBH. Such regions are the main focus of this work.

1.1.1 Obscuration and the Narrow-Line Region (NLR)

The obscuring dusty torus can have different orientations that can influence how we classify AGNs. On Type 1 sources that present broad permitted (BLR) and narrow forbidden and permitted (NLR) emission lines, the torus is possibly almost faced on. Type 2 AGNs, which only present narrow emission lines, have their BLR hidden from our view by a torus at larger inclinations respective to our LOS, making just the NLR detectable. Its dependence on the orientation of the dusty torus is proposed by the Unified Model of AGNs (Antonucci, 1993; Netzer, 2015).

Absorption and scattering of the light from the AGN continuum due to material in the galaxies contribute to their obscuration. There are many sources to obscure active galaxies. The largest contribution comes from the small-scale dusty torus, which can achieve column densities of about $N_H \approx 10^{25} cm^{-2}$. Obscured sources ($N_H \geq 10^{22} cm^{-2}$) are the largest population of AGNs and probably even greater at high redshifts, where the environments are gas-rich. Compton-thick sources ($N_H \geq 10^{24} cm^{-2}$) are when the medium becomes optically thick to Compton scattering, in that case, even hard X-ray spectrum is affected (Hickox and Alexander, 2018). For such sources, where the continuum is not directly seen, studying their NLR and reprocessed light can lead to a better understanding of the system.

Spectroscopy can reveal more than 100 emission lines in the NIR-UV range (Netzer, 2013, Section 7.2.1). The emission lines give us important information about the regions where they were produced. The broadening of permitted emission lines seen in

[1] The sphere of influence is the radius where the gravity of the SMBH equals the potential of the host galaxy. Clouds under this region are governed by the SMBH and beyond by the galaxy potential. Typically this radius is in order of some parsecs.

Type 1 sources is mainly due to the Doppler effect caused by orbital motions around the SMBH in the BLR. The density conditions do not allow the detection of forbidden emission lines. The BLR density is much higher than the critical density, making the collisional deexcitation the main channel, suppressing the forbidden emission. Using values for [OIII]λ5007 we can achieve a lower limit to the BLR density of $n_e \geq 10^8 cm^{-3}$ (Osterbrock and Ferland, 2006, Section 13.6). On the other hand, the narrow permitted and forbidden emission lines are emitted hundreds up to thousands of parsecs away, in the NLR and Extended Narrow Line Region (ENLR, Ma et al. 2021). Typical conditions of the NLR are $T_e \approx 1 - 2 \cdot 10^4 K$, measured from [NII]$\lambda\lambda$5755,6548,6583, and $n_e \approx 10^3 cm^{-3}$ traced by the [SII]$\lambda\lambda$6716,6731 (Osterbrock and Ferland, 2006, Section 13.4).

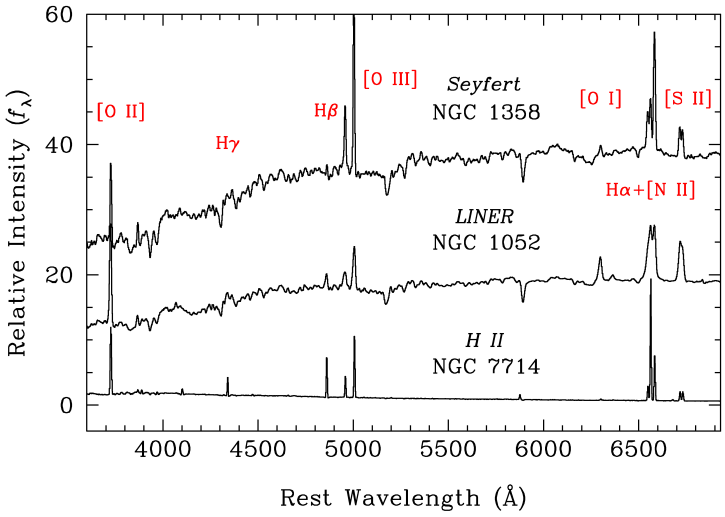

Figure 1.2: Typical spectra of Seyferts, LINERs, and Starburst galaxies (HII region-like spectra) taken from Ho (2008) and adapted from Ho et al. (1993). Different emission lines strengths (highlighted by the red legends) are shown for each spectrum and are related to their physical environment and source of ionization (e.g., AGN for Seyferts and LINERs, young massive stars in an HII region).

Temperatures of about $T_e \approx 10^4 K$ and no relation between T_e and ionization degree suggest that photoionization is the main source of ionization of typical NLRs. In addition, the emission lines present a great diversity of ionization degrees and different line ratios than observed in HII regions, like seen in figure 1.2, requiring a much harder continuum. In fact, from photoionization calculations it is possible to infer the general slope of the continuum being a power-law relative to the frequency $L_\nu = C\nu^{-\alpha}$ (optical-UV), with $\alpha \approx 1 - 2$ (Osterbrock and Ferland, 2006, Section 13.5). All those conditions point towards the photoionization by the AGN continuum acting in the NLRs.

The ionized structure is far from constant across the NLR. Because of the different ionization potentials (IP) and likely different temperatures (T_e), emission lines as [FeVII]λ6086 (IP = 100 eV), [OIII]λ5007 (IP = 35.1 eV), and [SII]$\lambda\lambda$6716,6731 (IP = 10.4 eV, Van Hoof 2018) will be produced at different zones. Also, the density structure will discriminate emission lines of different critical densities (Kewley et al., 2019). Critical density is the density where collisional and radiative deexcitation are equally probable. For higher densities, the collisional deexcitation suppresses the emission line since the collisions happen faster than the radiative lifetime (Osterbrock and Ferland, 2006, Section 3.5). The high ionized gas will tend to be produced closer to the ionizing source. At the same time, the contribution of a partially ionized zone, with the bulk of low-ionization lines, will contribute more to the emission far from the source. This structure is a natural result of photoionization of an optically thick gas in the presence of a radiation field (Osterbrock and Ferland, 2006, Section 2.3;13.5). Stratification of the NLR is also shown in optical and MIR studies, reporting that high IP lines tend to have larger widths and, assuming rotation, are likely emitted closer to the center (Netzer, 2013, Section 7.2.1).

Obscuration also shapes the NLR, making the illumination non-isotropic, but collimated normally in double-sided ionization cones. The bicone shape, often seen in [OIII]λ5007, traces the ionized gas photoionized by the central source. The ionization cones also reveal that the accretion disk and torus often do not have the same inclination as the galaxy disc (Netzer, 2015).

Ionization cones can reveal part of the NLR structure and bring us information of the central obscurer. The bicone aperture and orientation are probably related to the inner boundaries of the torus, making it possible to study them indirectly. Some studies also indicate that the bicone does not end suddenly. Still, far from the ionization axis, where the low-ionization lines are stronger, the radiation is probably being filtered by the small scale obscuration (Netzer, 2015). Dust is also likely to be present in polar directions since dusty NLR clouds better model emission lines (Netzer, 2013, Section 7.2.1).

1.1.2 AGN-driven Outflows and Shock Ionization

Narrow-line region kinematics often are more complex than pure stellar rotation. The main reason is that AGNs can also produce kinetic power, AGN-driven outflows, in the form of winds and jets. These outflows can make outward motions and heat the

environment since they carry out energy and momentum.

Usually seen in radio and accelerated in the central regions, jets are double-sided highly collimated emissions. The radio loudness parameter R defined as the $\frac{L_\nu(5GHz)}{L_\nu(4400\mathring{A})}$ is used to differentiate powerful radio-loud (R $\geq$ 10) from low power radio-quiet, but not necessarily radio silent, sources. Although most AGNs present radio emission, about 10% are radio-loud (Netzer, 2013, Section 1.1.4). The collimated plasma, often with relativistic velocities, expands through the interstellar medium (ISM), compressing the gas on its way and creating a cocoon of expanding gas in the perpendicular direction, a lateral outflow (Morganti et al., 2015). Even for radio-quiet sources, recent works show that jet-ISM interaction can trigger powerful outflows (Morganti et al., 2015) and promote turbulence on galaxy discs up to a few kilo-parsecs (Venturi et al., 2021).

Winds typically have higher opening angles and achieve lower velocities. AGN winds in Seyferts usually attain some hundreds, common in Type 2 AGNs, up to thousands of kilometers per second seen in Type 1 sources. In quasars, winds can reach tens of thousands of kilometers per second (Heckman and Best, 2014). Jets are much faster, achieving fractions of the speed of light, while starburst winds, like those produced by supernovae, usually reach a few 100 km/s (Fabian, 2012). They can be triggered, for example, by the radiation pressure on high accretion systems. Winds closer to the galaxy disc tend to be more luminous due to higher densities and frequently well collimated until they interact with denser clouds and ascend to the halo (Veilleux et al., 2005).

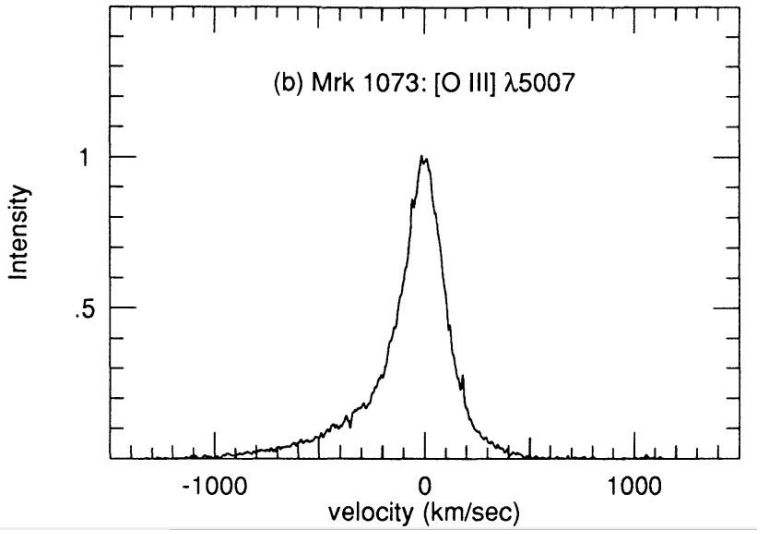

Figure 1.3: The asymmetric line shape of [OIII]λ5007 in velocity space in Mrk 1073 taken from Veilleux (1991).

We focus on the outflows constrained using IR-optical emission lines for the present work. Motions of different gas phases, such as molecular and ionized gas, can show deviations from stellar rotation. Emission lines, often of high ionization, commonly present an asymmetrical line shape, an extended wing, considered a doppler shift. Figure 1.3 shows the typical line profile. These asymmetric wings are interpreted as gas clouds with shifted bulk velocities and outflowing to the external regions. These outflows are usually detected in blueshift, suggesting that this component comes from the near side. In contrast, the redshifted wing is possibly suppressed by the dusty medium of the NLR (Peterson, 1997).

The impact of AGN-driven outflows does not resume to change the environment kinematics but also contributes to heating. Jets, in particular, can deposit their energy in small regions making shock waves capable of ionizing the gas. Shock ionization, also called collisional ionization, happens when free electrons are capable of ionizing the atoms by colliding with them (Netzer, 2013, Section 5.2). Shocks are more important in gas at higher temperatures, whre there are enough electrons with energies above the ionization potential of the species (Osterbrock and Ferland, 2006, Section 12.7). Because of that, regions dominated by shocks present a relation between temperature and the degree of ionization. The O^{+} production, for example, peaks at $T_e \approx 30000$ K, while O^{++} at $T_e \approx 90000$ K (Osterbrock and Ferland, 2006, Section 12.7). Shocked regions can also produce an increase of the gas velocity dispersion and electron densities (Kewley et al., 2019). As a result, gas of high-velocity dispersion often is associated with regions presenting enhanced low-ionization line ratios, like [SII]/Hα and [OI]/Hα, caused by shocks. Higher ionization can be achieved when fast shocks are present ($v \geq 500$ km/s) and result from the cooling of the shocked gas. Such gas produces a radiation field, from UV to soft X-rays, called the photoionizing precursor, that causes ionization in front of the shock (Kewley et al., 2019; Allen et al., 2008).

1.1.3 Coronal Line Region (CLR)

Coronal lines (CLs) are forbidden transitions of highly ionized species of IP $\geq$ 100 eV, requiring UV to X-ray photons, above the typical stellar continuum ($\approx$ 55 eV, Moneti and Ramo 2001). The high energies involved make these lines good tracers of AGN activity. Although supernovae remnants, Wolf–Rayet stars, and planetary nebulae can also produce them, their typical luminosities of about $10^{31} - 10^{33}$ erg/s (Dopita et al.,

2018), are orders of magnitude fainter than in AGNs.

The coronal line region (CLR), where CLs are emitted, is likely to be closer to the AGN, though outside the BLR, since the density at the BLR does not allow forbidden transitions to occur. Many studies show signs of stratification of the CLR (Rodríguez-Ardila et al., 2011), with high IP coronal lines having broader profiles, so likely emitted closer to the AGN, but this correlation is not always detected (Mazzalay et al., 2010; Cerqueira-Campos et al., 2021). According to Cerqueira-Campos et al. (2021), coronal-line forest AGNs, which present a great diversity of CLs in their spectra, are mostly Type 1 AGNs. This result agrees with the bulk of CLs being produced in a region between the BLR and NLR, although these studies need larger samples to ensure this finding. The CLR location and mechanisms are still under debate, but what is clear is that the lower-ionization lines, like [Fe VII]λ6086 and [Ca V]λ5309, both with IP $\approx$ 100 eV, can be emitted across the NLR in scales up to hundreds of parsecs (Mazzalay et al., 2010). Higher IP lines are usually concentrated in the nucleus (Mazzalay et al., 2010; Rodríguez-Ardila et al., 2011).

Many mechanisms associated with AGN can produce coronal lines such as hot accretion disk around intermediate-mass black holes (Cann et al., 2018), reflection from the inner torus wall (Rose et al., 2015), fast shocks triggered by outflows (Fonseca-Faria et al., 2021) or even a NLR dominated by matter-bounded clouds (Cerqueira-Campos et al., 2021). The last two will be discussed in this work.

Often CL luminosities correlates well with [OIII]λ5007 and X-ray luminosities (Rodríguez-Ardila et al., 2011; Negus et al., 2021). Studies of AGNs presenting CLs also found typical NLR temperatures of about $T_e \approx 10^4$ K (Mazzalay et al., 2010; Rodríguez-Ardila et al., 2011; Cerqueira-Campos et al., 2021). Both pieces of evidence favor the scenario of CLs being produced by photoionization. Binette et al. (1996) propose a NLR scenario with two populations of clouds: matter-bounded clouds of high ionization degree and ionization-bounded clouds of low to intermediate ionization degree. Ionization bounded clouds, far from the nucleus, receive radiation filtered by the matter-bounded, which modifies the power-law incident on these clouds. In the presence of most matter-bounded clouds, the NLR production of intense CLs is expected (Cerqueira-Campos et al., 2021). Cerqueira-Campos et al. (2021) found a difference of $\Delta T_e \approx 5000$ K between [OIII]$\lambda\lambda$4363,4959,5007 and [NII]$\lambda\lambda$5755,6548,6583 temperatures, what the authors emphasized being compatible

with this scenario. These electron temperature differences, however, are not constant, but a function of the temperatures, how as shown recently in Dors et al. (2020).

Outflows can induce fast shocks capable of creating X-ray photons via bremsstrahlung. Such X-rays can photoionize the gas leading to highly ionized species (May and Steiner, 2017). Jets were found to trigger CLs in recent studies (May et al., 2018; Fonseca-Faria et al., 2021). Fonseca-Faria et al. (2021), in particular, found [Fe VII]λ6086 extended emission, up to 2 kpc, in a sample of 5 local Seyferts. The authors associated this emission with dust-free regions and also found that this emission is well-matched to X-ray and radio jet emissions. The authors also stated that the excitation of [Fe VII]λ6086 and their off-center peaks are better described if they are shock-driven by the passage of the jet. This is a possible scenario when the CLs are extended hundreds of parsecs from the nucleus and associated with low-power radio emission.

1.2 The Seyfert Galaxy NGC 5643

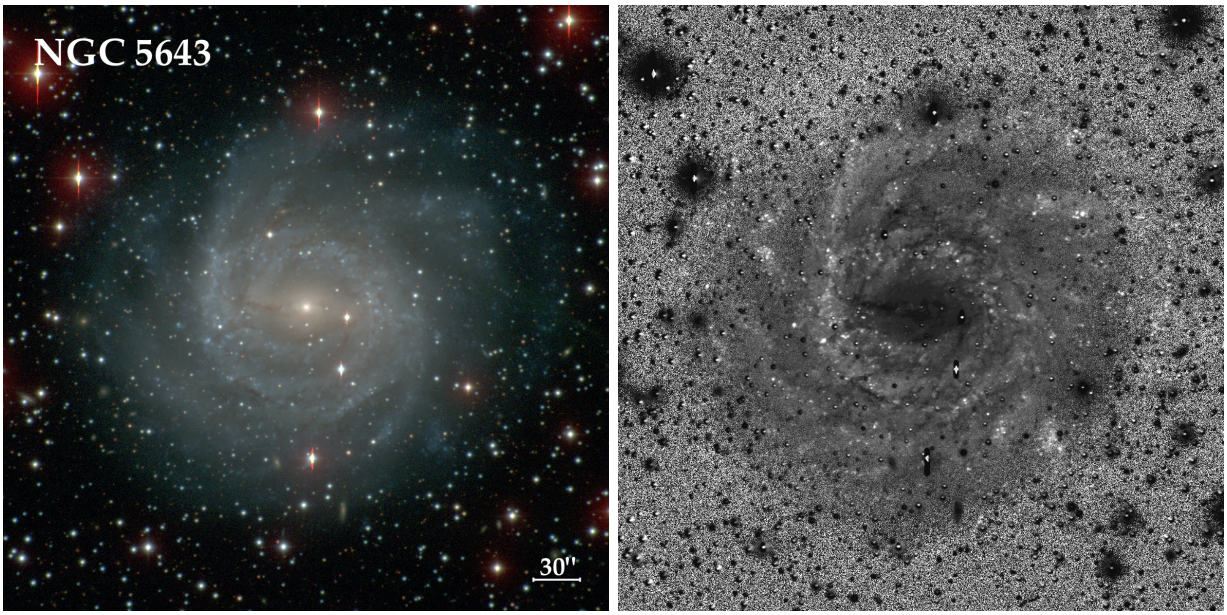

Figure 1.4: (Left) Composite image of NGC 5643 (RGB: I, V, and B bands) taken with CCD camera of du Pont 2.5-meter telescope from the Carnegie-Irvine Galaxy Survey (Ho et al., 2011). North is up and east to the left. (Right) Color index map B-R, in the same scale as the composite image, presents in dark colors regions of high extinction. More dust is associated with the inner spiral arms and the bar, with a dust lane in the south to the west-central area, agreeing to be the near side of the galaxy.

NGC 5643, shown in figure 1.4, is a late-type SAB(rs)c galaxy, almost face-on (i $\approx 30°$, Fischer et al. 2013) and only 16.9 Mpc away (Tully and Fisher, 1988). The nuclear

activity is classified as a Seyfert 2 (Véron-Cetty and Véron, 2010) with a Compton-thick nuclear obscuration ($N_H \geq 5 \cdot 10^{24} cm^{-2}$, Annuar et al. 2015). Its SMBH was estimated from $M-\sigma$ relation as $M_{BH} \approx 2.75 \cdot 10^6 M_\odot$ (Goulding et al., 2010). Most recent bolometric luminosity estimate found $L_{bol} = 8.14 \times 10^{43} erg/s$ (García-Bernete et al., 2021; Ricci et al., 2017).

Morris et al. (1985) presented Hα and [OIII]λ5007 emission line cubes from the Fabry-Perot spectrometer TAURUS at a seeing $\geq 2''$ and velocity resolution of about FWHM $\approx$ 25 km/s. The kinematics show rotation distortions in the E-W direction, qualitatively in agreement with a flow through the bar at position angle (PA) = $90° \pm 10°$. The emitting region is elongated in the bar direction. The authors also presented Very Large Array (VLA) radio continuum maps at 6 and 20cm. A core and two lobes were detected with the same orientation as the emission line region. The core size measured was $0.6''$ with jet direction at PA = $87° \pm 3°$. The jet E-W extension has at least $35''$ ($\approx$ 2.9 kpc). They propose that the gas flows across the bar to the nucleus, where the gas feeds a disc orthogonal to the bar that helps to collimate the ionizing continuum and the radio jet. Leipski et al. (2006) presented 3.5 cm VLA observations with a angular resolution of $1.7''$x$1.7''$ beam. The authors estimated a nearly $30''$ extent, diameter of about 2.5 kpc, with a luminosity of $\nu L_\nu[8.4GHz] = 4.62 \cdot 10^{37}$ erg/s.

Schmitt et al. (1994) presented long-slit spectroscopy towards PA = $90°$ and $0.9''$ scale per pixel from the Cerro Tololo Inter-American Observatory (CTIO) 4m-telescope. The authors confirmed that the continuum is collimated in an ionization bicone, probably by the presence of an obscuring torus. They also found an increased extinction and density of $3''$ to the west, which they suggested to be where the active nucleus is hidden. The nucleus presents $n_e \approx 200\ cm^{-4}$ and $E(B-V) = 0.6$, compared to $n_e \approx 450\ cm^{-4}$ and $E(B-V) = 0.7-0.8$ at $1.8''$ and $3.6''$ to west. Towards the east side, there is an abrupt drop of extinction around 5". The extinction corrected excitation ratios were similar towards both sides (E-W), suggesting that the dust in the bar is probably obscuring the west side. They propose that the cone is in front o the bar towards the east and behind on the west side. This result changes the scenario of Morris et al. (1985), now with the nuclear disc tilted alongside the bar.

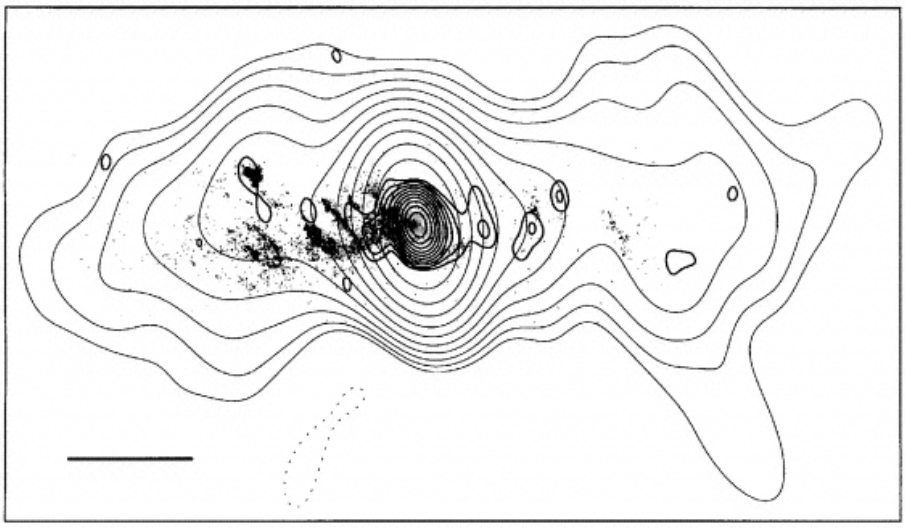

Figure 1.5: HST excitation map of [O III]/Hα and superposed radio contours taken from Simpson et al. (1997). The thick lines indicate the 6 cm radio map. The thin lines are the 6 cm map smoothed to the 20 cm map resolution from Morris et al. (1985). North is up and east to the left. The horizontal bar indicates the scale of 5″.

With *Hubble Space Telescope* (HST) high spatial resolution ($\approx 0.1''$) images of [OIII] λ5007 and $H\alpha$, Simpson et al. (1997) confirmed the v shape eastern ionization cone. The western cone was absent on their data. They suggested it is obscured and behind the disc. They found a dust lane perpendicular to the radio axis on the west side with a color index map. This red arc structure at 1″ from the nucleus extends to the west, north, and south. The authors also mention that the galaxy is rotating counterclockwise. The northeastern half is the far side of the galaxy, which is compatible with the dust lane detection in the southwest. Additionally was presented evidence of jet-ISM interaction as seen in figure 1.5. The [O III]/Hα map superposed to 6-cm VLA radio data (Morris et al., 1985) is enhanced in the direction of the small-scale radio emission, which does not follow the large-scale trend but is aligned with the southern east cone emission at PA = 113°. Because of the coincident center between radio and optical data, the hypothesis of a hidden nucleus from Schmitt et al. (1994) was ruled out.

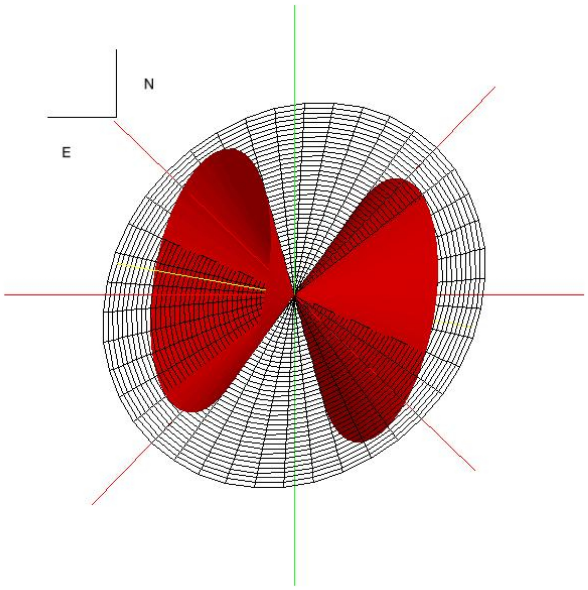

Figure 1.6: Ionization cone model obtained in Fischer et al. (2013). The grid represents the galaxy disc and the red bicone the ionization cones of NGC 5643.

Fischer et al. (2013) fitted kinematical models to the long slit HST/STIS data for many outflowing NLRs. For NGC 5643 they fitted a wide opening angle bicone inclined 65° from our LOS ($i = 25°$) seen in figure 1.6. The bicone model has orientation PA = 80° and inner and outer opening angles $\theta_{min} = 50°$ and $\theta_{max} = 55°$. The model opening angles are wider than the observed data, probably by the intersection of the ionization cones with the galaxy disc. The maximum velocity achieved in the model was $v_{max} = 500$ km/s with a turnover radius (where the outflowing gas begin to decelerate) of $r_t = 70$ pc. Their model predicts extended blueshifted emission towards the west.

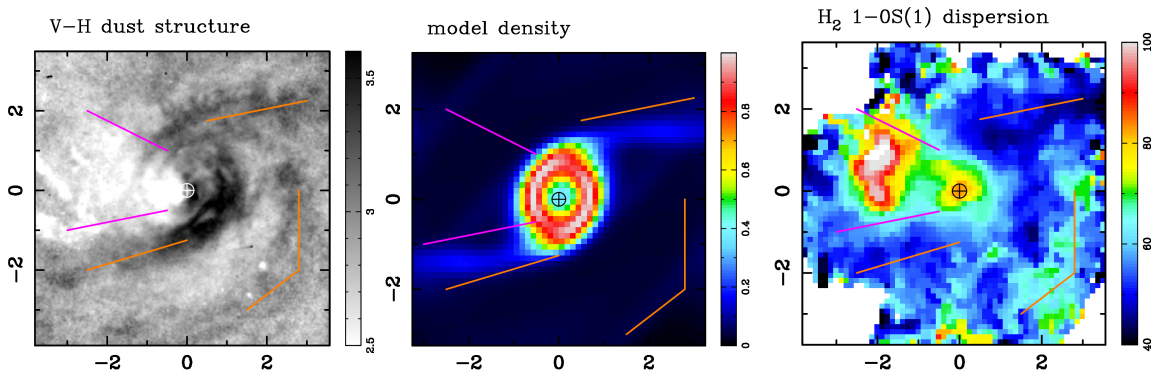

Figure 1.7: (Left) V-H HST map adapted from Martini et al. (2003) presented in Davies et al. (2014). North is up and east is left. The scale is given in arc seconds. The map clearly shows the nuclear spiral structure and the high extinction structure towards the west in darker regions. The marked lines represents the arms and the eastern ionization cone region. (Center) The density model of the simulation is used to match the molecular kinematics. The model shows the inflowing molecular gas, triggered by the large-scale bar, feeding the internal ring. (Right) Dispersion map of H2 1-0 S(1) showing the molecular outflow towards the northeast and the enhanced dispersion in the western third arm.

Davies et al. (2014) presented near-infrared (NIR) integral field spectroscopy K-band observations from Spectrograph for Integral Field Observations in the Near Infrared from the Very Large Telescope (SINFONI/VLT). The H2 1-0 S(1) molecular emission and dust structure seen in the V-H HST map from Martini et al. (2003) show in figure 1.7 presented the nuclear two-arm spiral. They reproduced the molecular kinematics with a hydrodynamical simulation of a disk with a circumnuclear ring generated by a large-scale bar. Molecular outflows were found to the northeast, as evinced in the dispersion map of figure 1.7). The authors said that the emission comes from the far side of the eastern cone, probably from the disk plane, and is being pushed away by the outflow. A third arm shown in the dust map also presents high dispersion, what they propose to be a sign of a recent perturbation or the far west side of the molecular outflow seen in the east.

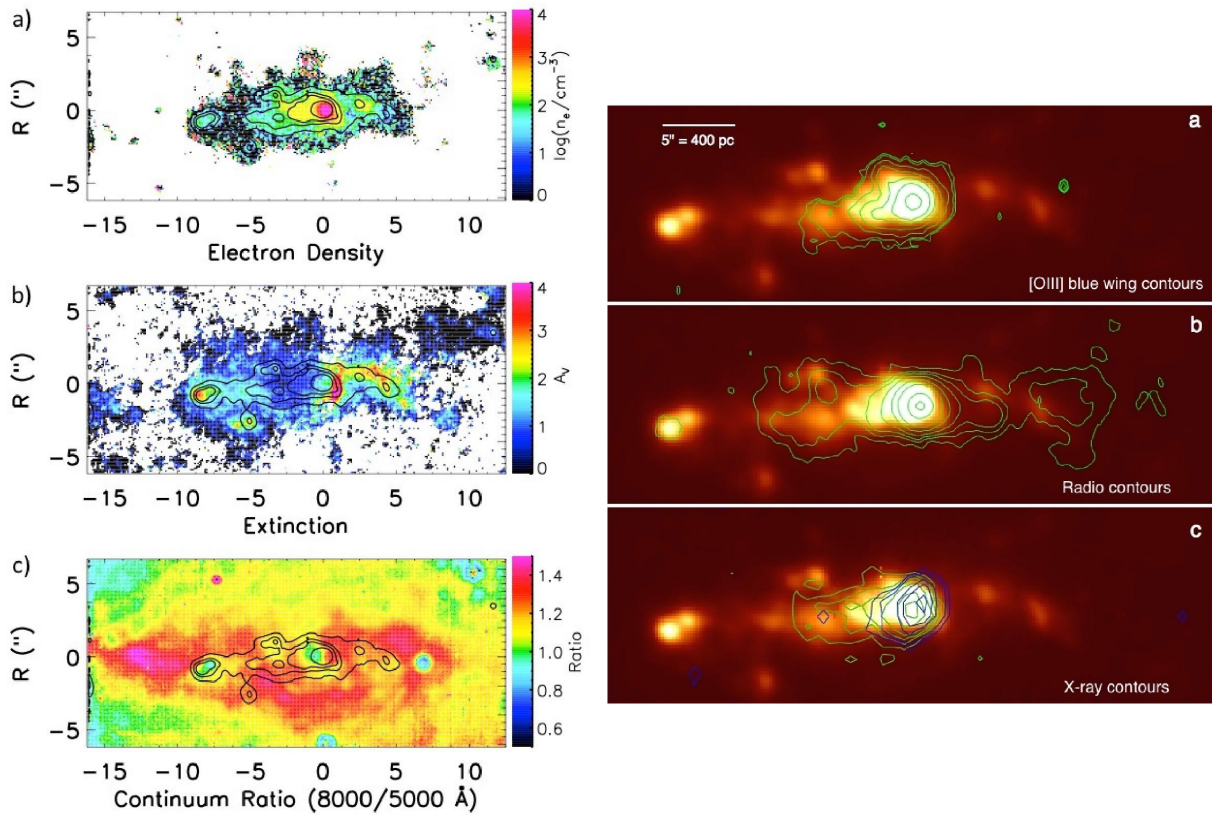

Figure 1.8: (Left) Electron density (a), extinction (b) and red to blue continuum ratio maps (c). The contours represent the Hα emission. The extinction map shows the western dust lane structure associated to the bar. (Right) Hα maps with superposed contours of [OIII] wing component (top), radio emission at 3.5 cm (Leipski et al., 2006) (Middle) and Chandra emission at 0.3–0.5 keV (green contours) and 0.5–8 keV (blue contours) X-rays (Bottom). North is up and east is left. Plots from Cresci et al. (2015).

Optical integral field unit (IFU) obtained with the Multi Unit Spectroscopic Explorer (MUSE) from the VLT with FWHM $\approx 0.88\,''$ was presented by Cresci et al. (2015). The dusty structure, shown in the middle left panel of figure 1.8, was suggested to produce the collimation of the ionization bicone, has a size of $\approx 7'' \times 1.5'' \approx 580$ pc x 125 pc and is connected to the dust lane in the bar as evinces the continuum ratio map of figure 1.8. Extinction is higher in the west circumnuclear region $A_V > 3$ mag, achieving a maximum of $A_V = 4.8$ mag. Electron densities, at fixed $T_e = 10^4 K$, in the nucleus is $n_e \approx 3 \cdot 10^3 cm^{-3}$ and drops outwards. Diagnostic diagrams showed Seyfert-like nucleus and cones, LINER-like emission, interpreted as shocks, in the surrounding region and the dusty structure towards the west. The authors found an outflow in [OIII]λ5007 at $1.6''$ $\times$ $1.6''$ nuclear spectrum with v = -200 $\pm$ 15 km/s and FWHM = 590 $\pm$ 20 km/s. The spatially resolved blue wing map, on the right side of figure 1.8, had good agreement with the Chandra Space Telescope data in the soft x-rays, which can indicate photoionization

or shocks. The wing map was also in accordance with the VLA radio continuum map, caused by jet or winds. The authors claimed that the outflow, the soft x-ray, and the radio emission have a common origin. Clumps of star formation were found in the same direction as the outflow 15 ″ away, suggesting a positive feedback scenario.

There are other NIR studies on NGC 5643. Menezes et al. (2015) presented the same K-band results as an example of the application of treatment procedures on SINFONI data cubes. The $Br\gamma$ presents signs of acceleration closer to the nucleus and a good match with [OIII]λ5007 HST cloud positions. From the H_2 morphology, they argue for a molecular disc or torus in the N-S direction responsible for feeding the AGN and collimating the ionization cones. Riffel et al. (2018) reported observations of the Gemini Multi-Object Spectrographs (GMOS) IFU from Gemini South telescope in the NIR, between 7750–9950 $\AA$ and with FWHM = 0.8″. They found the ionization cones dominated by outflows, with [SIII]λ9069 kinematics in redshift to the east and blueshift to the west. From the [SIII]λ9069 channel maps, an elongated structure was discovered in lower blueshift velocities to the east and redshift to the west, which they considered gas on the plane of the galaxy, heated by the outflowing gas.

Alonso-Herrero et al. (2018) shown Atacama Large Millimeter/Submillimeter Array (ALMA) cold molecular CO(2–1) at 0.26″ x 0.17″ resolution emission tracing the two-arm nuclear spiral up to 10″ in each side. The velocity residuals show strong non-circular motions, shown in figure 1.9. The regions have [OIII]λ5007 counterparts, including towards the southeast where the [OIII]λ5007 and radio jet was suggested to be interacting with the galaxy disc (Cresci et al., 2015). The authors suggest that the molecular gas is being pushed away by the outflow traced the [OIII]λ5007 emission. A nuclear disc was detected, probably tilted about the disc, and aligned to the N-S direction with dimensions 0.32″ x 0.24″ $\approx$ 26 pc x 20 pc. They propose that this nuclear disc could be the obscuring torus of NGC 5643.

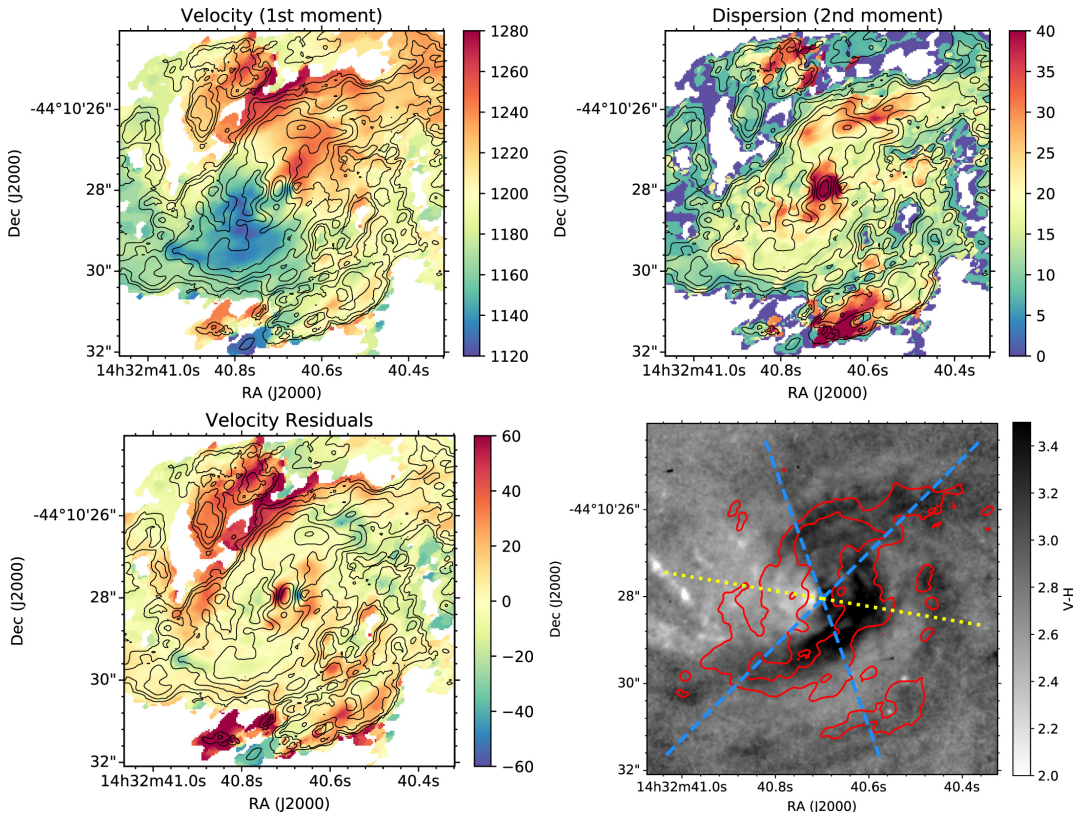

Figure 1.9: Molecular velocity (top left), dispersion (top right) and velocity residuals (bottom left) across the FoV = 8″ x 8″. The black contours are the CO intensity. At the bottom right, the V-H map (Martini et al., 2003; Davies et al., 2014) is superposed to the CO contours. The ionization cones aperture are indicated as blue dashed lines Fischer et al. (2013) and their orientation as a yellow dashed line towards PA = 80°). North is probably up, and east is left. Images taken from Alonso-Herrero et al. (2018).

A multiphase outflow work was made by García-Bernete et al. (2021) combining observations of ALMA CO(2-1) with a new MUSE/VLT data cube with FWHM = 0.5″. The authors found multiple Gaussian components in both phases, for [OIII]λ5007 and CO(2-1). From the [OIII]λ5007 outflow kinematics, they found velocities increasing to 750 km/s up to 10″ $\approx$ 830 pc and decreasing farther away. The CO in the outflow region extends 2.3 kpc in the E-W direction, and the spiral arms present outflowing and inflowing motions. Molecular gas presents lower outflow velocities than ionized gas but a similar radial profile. Because of that, the authors suggested that the wind is dragging the molecular gas. The molecular phase was found to dominate the outflowing mass. A radiation-driven wind plus gravitational drag model reproduced the two-kiloparsec scale outflows. They also found that the eastern spiral arm contains only $50 - 70\%$ of the molecular gas in the western arm. The authors interpreted it as being due to the destruction and clearing of molecular gas by the wind. This is an indication of possible negative feedback on kiloparsec scales in

NGC 5643.

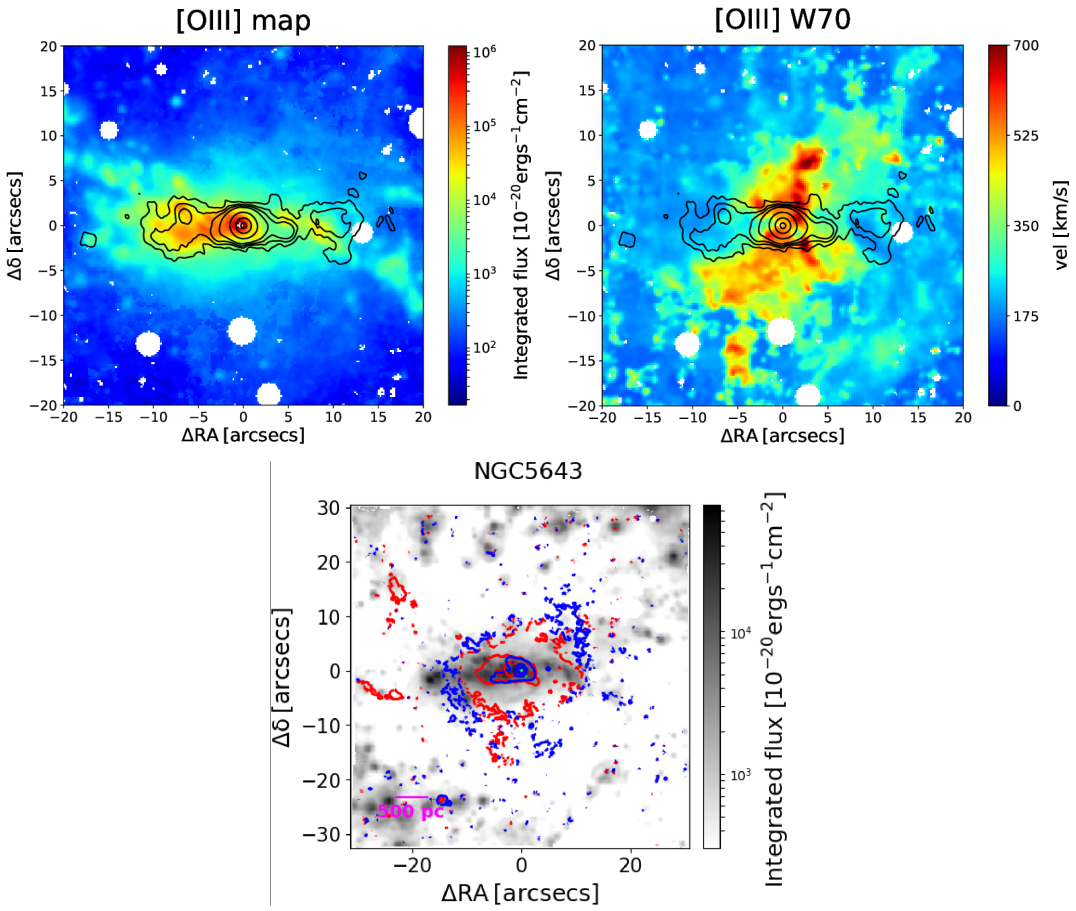

Figure 1.10: Top: Flux and W70 maps for [OIII]λ5007 with the radio contours from Leipski et al. (2006) superposed. Plots were taken from Venturi et al. (2021). Bottom: Outflowing gas in redshift and blueshift with ordinary rotating in the background from Mingozzi et al. (2019). North is up and east towards left.

Mingozzi et al. (2019), using the Cresci et al. (2015) MUSE/VLT data cube, separate the disc and outflowing gas emission based on the stellar line profiles. The blueshifted and redshifted gas distribution found for NGC 5643 is shown in figure 1.10. They use the disc and outflowing emission to study their properties. The authors found that outflowing gas is more associated with higher densities and excitation than the disc. Regions on which the outflow dominates tend to show the highest and the lowest values of low ionization line ratios. Their lowest ratios come from the innermost regions, close to the ionization cone axis. On the other hand, the highest ratios come from the edges of the cones and in the cross-cone areas, often associated with $\sigma([OIII]\lambda5007) \geq 200$ km/s. They suggest that a NLR with matter and ionization bounded clouds (Binette et al., 1996) can explain the observations. To account for the highest low-ionization ratios and increased [OIII]λ5007 dispersion, shock was suggested to play a role.

Venturi et al. (2021) studied with MUSE/VLT data cubes a sample of galaxies with low power jets with L $< 10^{44}$ erg/s at lower inclinations against their galaxies disc. The data cube used for NGC 5643 was the same as in García-Bernete et al. (2021). The authors found the W70 [2] enhanced perpendicular to the direction of the cones, achieving W70 $\approx$ 700 km/s up to 3 kpc from the nucleus, which can be seen in figure 1.10. They propose that this W70 value is due to the interaction of the jets with the disc of the galaxy, causing turbulent motions. The turbulence does not have peak velocities too far from the rotation component, distinct from standard outflows.

By using *XMM-Newton* data, Guainazzi et al. (2004) obtained column densities in the range N_H 6–10 $\cdot 10^{23} cm^2$, suggesting the possibility of a nuclear Compton-thick absorber. Matt et al. (2013), using data with longer exposures from *XMM-Newton*, confirmed the Compton-thick nature of the nuclear obscuration. They detect highly ionized lines ranging from 0.5-7.4 keV and suggest the main mechanism is likely photoionization, although a shock-ionized region can be present. Annuar et al. (2015) presented *NuSTAR* space telescope observations together with archival *Chandra*, *XMM-Newton* and *Swift-BAT* space telescopes, making a broadband analysis from 0.5-100 KeV, fiting the nuclear emission of NGC 5643 using consistent torus models. They found a $N_H \geq 5 \cdot 10^{24} cm^{-2}$, an absorption corrected luminosity of $L_{2-10KeV} = (0.8 - 1.7) \cdot 10^{42}$ erg/s. Assuming a ratio $L_{Bol}/L_{2-10KeV} \approx 20$ and the SMBH of $M_{BH} = 10^{6.4} M\odot$ (Goulding et al., 2010) the authors found an Eddington ratio of about 5-10%. They suggest that torus can be on the inner west warped disk or dust lane.

[2] The W70 velocity width is defined as W70 $= v_{85} - v_{15}$.

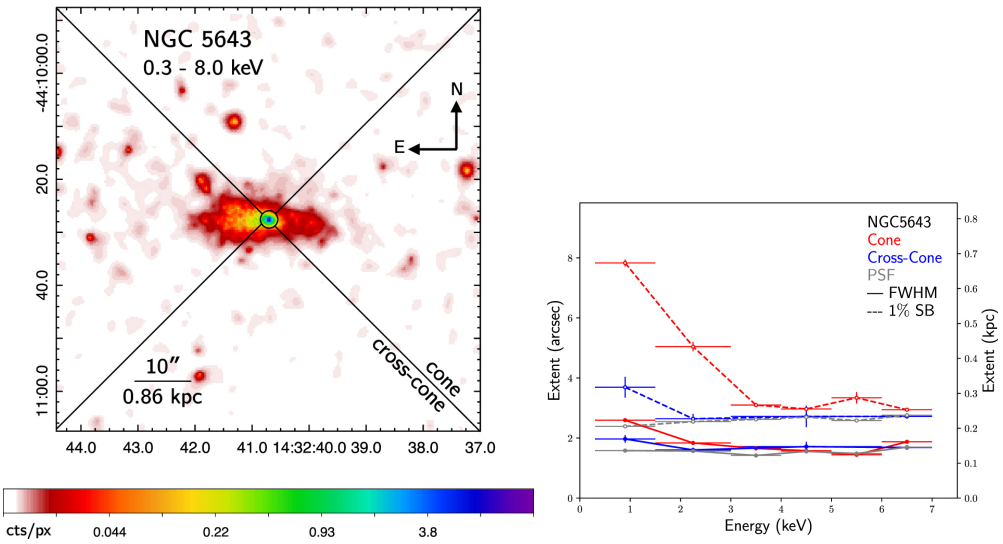

Figure 1.11: Plots taken from Jones et al. (2021). (Left) Image of 0.3-8 KeV range showing the emission across the cones and cross-cone regions. (Right) FWHM (full line) and at 1% surface brightness (dashed) profiles at the ionization cones and cross cone region.

Spatially resolved *Chandra Space Telescope* observations presented interesting results. Extended neutral Fe $K\alpha$ [3] emission was found by Fabbiano et al. (2018), compatible with the inner disc orientation found by Alonso-Herrero et al. (2018) along N-S direction, but with an angular size of $0.8'' \approx 65$ pc. The authors suggest that the CO and Fe $K\alpha$ are in a clumpy obscuring circumnuclear disk, the torus of NGC 5643. Jones et al. (2021) reported using *Chandra* data that NGC 5643 presented emission up to 670 pc in the bi-cone and 360 pc in the cross-cone regions, how seen in image 1.11. The emission across the cross-cone suggests that X-rays can leak out the torus.

Many works studied the coronal line emission from NGC 5643. The optical spectroscopy atlas of Morris and Ward (1988), with observations from the Anglo-Australian Telescope (AAT), reported the detection of [Ne V] λ3526 and [Fe VII]λ6086. Later on, Schmitt et al. (1994) presented CTIO 4m-telescope long-slit observations, showing extended [Ne V]λ3526 profile up to $10''$ to the east. On the other hand, Mazzalay et al. (2010) that presented HST long-slit spectroscopy observations just reported a nuclear [Fe X]λ6374 emission, probably disfavoured by the slit orientation. Rodríguez-Ardila and Fonseca-Faria (2021) analyzed the MUSE/VLT data cube from Cresci et al. (2015) and found extended

[3] Fe $K\alpha$ emission is a fluorescent line close to 6.4 KeV, that occurs when an electron goes from n=2 to n=1 to fill a vacancy due to a previous electron removal from the ground state (Netzer 2013, Section 5.4.2,Osterbrock and Ferland 2006, Section 11.2.1). Their contribution can come from highly-ionized gas, likely from the accretion disc, or even neutral Fe, associated to the torus (Netzer, 2015).

[Fe VII]λ6086 emission up to 0.8 kpc to the east and 0.9 kpc towards the west side. This work, with another four local Seyferts, found [Fe VII]λ6086 emission is likely produced by shocks and associated with the radio jet.

1.2.1 Motivation and Aims

Studying nearby AGNs allow us to explore the impact of the SMBH on its surroundings with great spatial resolution. These observations can lead to clues into how these systems interact with the interstellar medium (Heckman and Best, 2014). To reveal what mechanisms are driving the gas emission and kinematics. If the NLR links the SMBH domain and the host galaxy, understanding the conditions and mechanisms there, acting on the gas at different phases, can help us build a more comprehensive view of the impact of the AGN phenomena.

In this work, we conduct a detailed analysis of the nuclear and circumnuclear region of NGC 5643, addressing the multiphase gas conditions and mechanisms behind their emission. We aim to explore the neutral up to highly ionized gas properties up to several hundreds of parsecs with a high degree of detail using high-resolution IFU spectroscopy. The central region of NGC 5642 was observed with the instrument GMOS from the Gemini South telescope and is part of the Deep IFS View of Nuclei of Galaxies (DIVING^{3D}, Steiner et al. 2022) sample. Additional NIR data in the H and K bands data cubes comes from the instrument SINFONI from the VLT telescope. With the reduced data, we aim to:

- Analyze the emission line properties - to understand the physical conditions, geometry, excitation, and kinematics of the ionized gas;
- Study the properties of the coronal emission lines - the highly ionized phase;
- Reveal the structure of the ionization cones.

In the process, an additional subproduct will be the stellar populations kinematics and archaeology. The GMOS data cube presents a better spatial resolution than most previous works in the optical (Cresci et al., 2015). Even when the literature delivered better spatial resolution (García-Bernete et al., 2021; Simpson et al., 1997), the optical data cube brings higher spectral resolution, giving us a better view of the emission line profiles.

The expected results will describe the properties and structure of the nuclear and circumnuclear regions of this galaxy with unique precision. The detection of coronal lines will allow us a high degree of confidence in the details of the high ionization region. The results will be compared to recent works in radio, infrared, optical, and X-rays.

Chapter 2

Methodology

2.1 Data

Integral Field Spectroscopy (IFS)

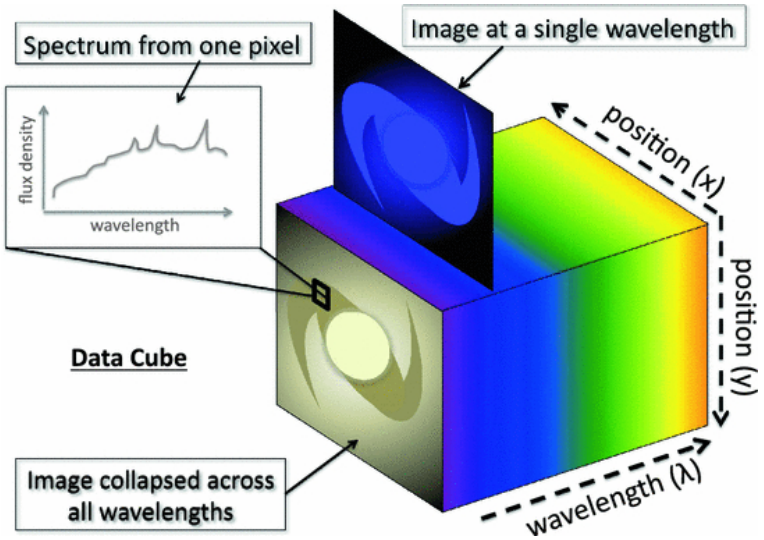

Figure 2.1: IFU data cube representation taken from Harrison (2016). The data cube has two spatial dimensions (x-y positions) and one spectral dimension (wavelength - λ). We can extract spectra of regions in the source (1D spectrum shown in the upper left panel) or pick maps at specific wavelengths (blue wavelength image from the data cube).

Integral field spectroscopy (IFS) is a spatially resolved spectroscopic method. The data consist of spectra of each spatial pixel on the source, called spaxels, obtained at the same time and can be arranged in a data cube as represented in figure 2.1. The IFU data cube has two spatial dimensions, the source projection in the plane of the sky, and the spectrum in the third dimension, in terms of wavelength. The final data can be seen as a collection of spectra for each part of the source or stacked images at slightly different wavelengths (Smith, 2014, Section 4.2.4).

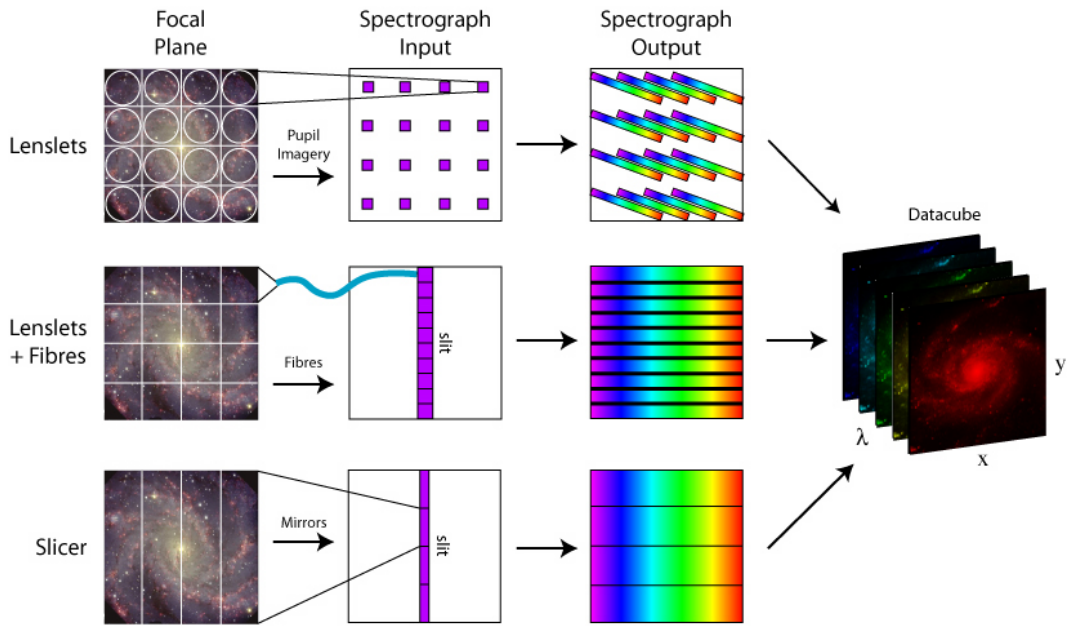

Figure 2.2: IFU spectroscopy main techniques scheme taken from Westmoquette et al. (2009) that adapted from Allington-smith et al. (1998). The GMOS / Gemini telescopes and SINFONI / VLT instruments use the middle and bottom panel techniques, respectively.

There are different ways to get an IFU data cube. The fibers with lenslets and the images-slicer techniques are essential for this assembly, shown in figure 2.2. In the lenslet plus fibers case, the light captured by the telescope goes to a lenslet array. The light is directed to the pseudo-slits, where it enters the spectrograph and is subsequently imaged by the CCD. One example is the instrument GMOS at Gemini telescopes. The image slicer splits the light into many slices by a segmented mirror. The light follows to a second mirror that rearranges the slices making radiation pass through the slits. These are the cases of the instruments SINFONI and MUSE at VLT (Westmoquette et al., 2009).

The DIVING^{3D} Survey

The DIVING^{3D} project is a survey designed to unveil the central regions of galaxies with IFU spectroscopy (Steiner et al., 2022). Inspired on the Palomar survey, the DIVING^{3D} has a statistically complete sample of galaxies, all objects with B < 12.0 mag, $\delta < 0°$ and $|b| > 15°$. The 170 galaxies of the sample were observed mainly with the GMOS IFU at the Gemini telescopes in one slit mode with a field-of-view (FoV) $= 3.5''$ x $5''$ and typical spatial resolution of 0.5-0.8″. The spectra cover the 4300–6800 $\AA$ optical range at about 1.3 $\AA$ spectral resolution. The survey aims to study the emission line properties of

the nuclei of galaxies, up to the faintest AGN population, and the ionizing sources of the circumnuclear gas. Additionally, aims to study the kinematics and properties of the stellar populations. Besides the complete sample, another strength of the survey is the high angular resolution, under seeing limited conditions, and high signal-to-noise ratio (SNR) observations (Steiner et al., 2021; Steiner et al., 2022).

Optical and NIR Data Cubes

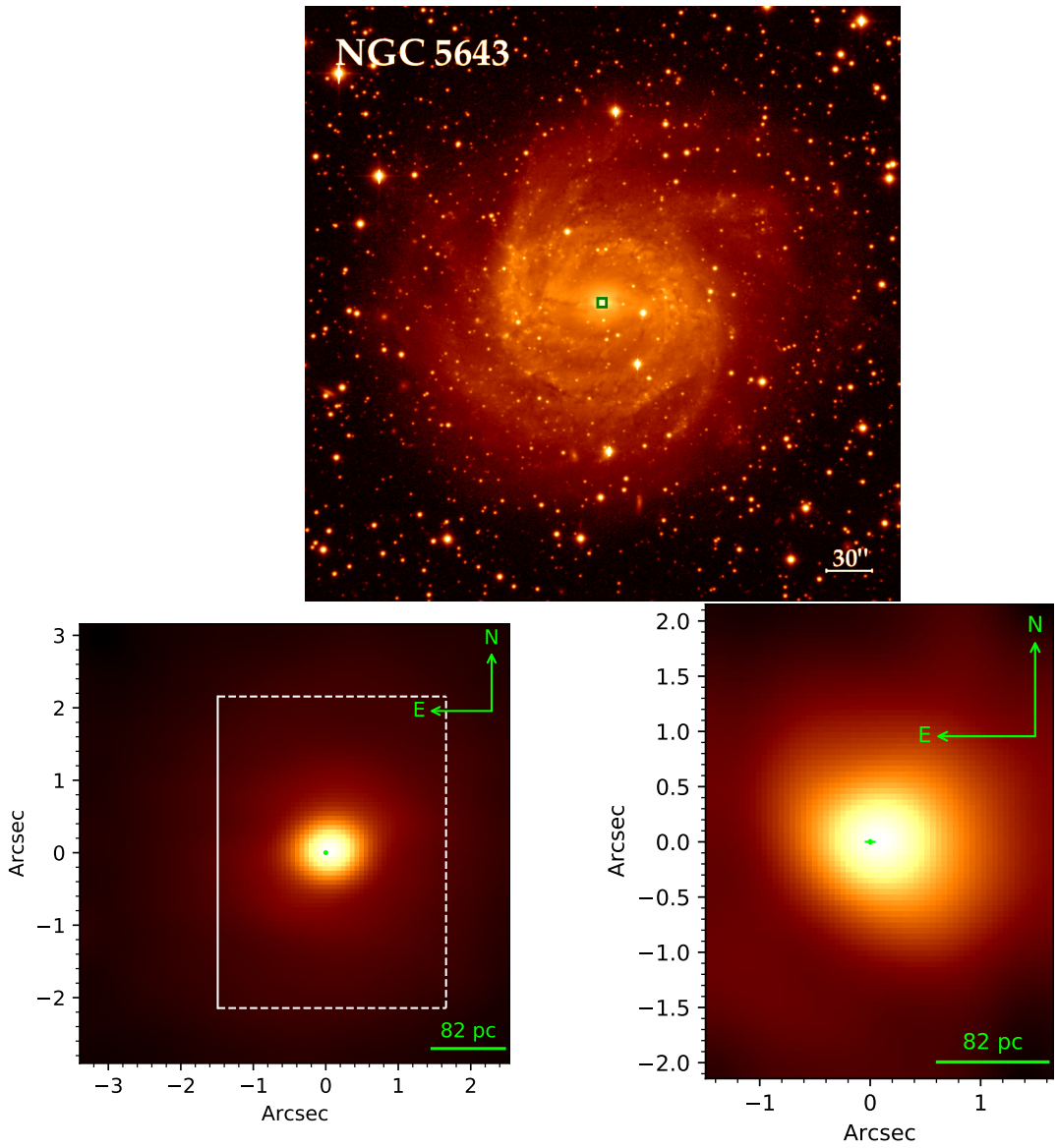

Figure 2.3: (Top) V-band image of NGC 5643 from the Carnegie-Irvine Galaxy Survey (Ho et al., 2011). North is up, and East is left. Evinced as a green box the final K-band SINFONI data cube FoV = 6.00″(N-S) x 5.88″(L-W). (Bottom left) Collapsed image along the spectral dimension for the K-band SINFONI data cube. The white box shows the optical GMOS data cube FoV = 3.10″(N-S) x 4.25″(L-W). (Bottom right) Collapsed image along the spectral dimension for optical GMOS data cube. The green cross marks the nuclear position as defined in appendix A.3.

The data used in the project consist of a optical and two NIR IFU data cubes. Data reduction and treatment follow the procedures described in Menezes et al. (2014, 2015, 2019). The optical data cube was obtained in the Gemini South telescope with the instrument GMOS in the context of the DIVING^{3D} survey. The observations obtained 3 data cubes with exposure times of 815 s each that were combined to get the final data cube. A collapsed image is presented in figure 2.3. The data cube cover the λ_{range} = 4782-6817

$\mathring{A}$ with a spectral resolution of R $\approx$ 4500 ($\Delta\lambda \approx 1.3$ $\mathring{A}$). Besides that, the final cube is on the 0.05″/pixel scale with of FoV = 3.10″(N-S) x 4.25″(L-W), and spatial resolution of $\langle FWHM([FeVII]6086\mathring{A})\rangle \approx 0.62'' \approx 51$ pc.

In the NIR, the datacubes in the H and K bands were obtained from the public archive of SINFONI. Both were originally observed in the 250 mas spatial scale with an FoV = 8″ x 8″, not applying adaptive optics. The K-band cube makes part of the observing proposal 083.B-0332(A) with the principal investigator (PI) Erin Hicks. The data was previously published in Hicks et al. (2013) and Davies et al. (2014). The data consist of 5 data cubes exposures of 600 s each that were combined to obtain the final data cube. This data was treated and partially analyzed in our group at Menezes et al. (2015). The final cube have FoV = 6.00″(N-S) x 5.88″(L-W) in the spatial scale 0.0625″ and $\langle FWHM(Br\gamma, [CaVIII]23210\mathring{A})\rangle \approx 0.46'' \approx 38$ pc resolution. A collapsed image and comparison with the GMOS FoV is shown in figure 2.3. The spectra cover the range λ_{range} = 20254-24183 $\mathring{A}$ with spectra resolution of R $\approx$ 4000 or $\Delta\lambda \approx 5\mathring{A}$ (Nurnberger D., 2011). The H-band makes part of the 075.B-0348(A) observing proposal with PI Eric Emsellem. The reduced data cube consists of a combination of 12 individual data cube exposures of 600 s each. After the reduction and treatment, the data cube reached a FoV = 6.37″(N-S) x 6.87″(L-W), with spatial scale 0.0625″/spaxel and resolution of $\langle FWHM(Br10)\rangle \approx 0.56'' \approx 46$ pc. Their spectra are in the wavelength interval λ_{range} = 14469-17846 $\mathring{A}$ with R $\approx$ 3000 or $\Delta\lambda \approx 6\mathring{A}$ (Nurnberger D., 2011). The procedures adopted for estimating the centroids and spatial resolution are in appendix A.4.

Reduction and treatment

The data cubes reduction and treatment were conducted by members of the DIVING^{3D} group. The data acquisition comprises more stages in the observation beyond the science exposures, such as bias, flat fields, arc lamps, sky images, and standard stars. The procedures mentioned here is a summary of the thesis of Menezes (2012). The GMOS data reduction was conducted with the Gemini package in the `IRAF` environment. For the SINFONI data cubes were used the ESO software GASGANO [1]. The main procedures for both are described as follows. At first, the field was trimmed to cover just regions with re-

[1] http://www.eso.org/sci/software/gasgano.html

levant detection. Then the master bias was subtracted, accounting for the electronic noise, combining 0 seconds exposures. Cosmic rays were removed from the scientific data with the routine L.A. COSMIC (van Dokkum, 2001). Next, 2D spectra were extracted in 1D spectra. The flat field correction divides the science data by a homogenous source, a lamp or twilight exposure, to account for inhomogeneities and differences in sensitivity. The flat field correction was different for the GMOS datacube because the correction was made by generating a response map that used both white lamp and twilight exposures to account for different gains across the CCD and fibres (Menezes, 2012, Section 3.2). Later, arc lamps were used for wavelength calibration. Next, the sky emission lines are subtracted, and the sky absorption removed, dividing the science spectra by the telluric absorption spectra. The flux calibration was done from the observations of a standard star, obtaining the relation between measurements and the flux. At last, the data cubes were constructed.

In order to make the most of the information that these data can provide, the DIVING^{3D} team developed some techniques to treat them (Steiner et al., 2009; Menezes et al., 2014, 2015, 2019). The procedures are briefly mentioned here and based on the thesis of Menezes (2012), and Ricci (2013). Firstly the data is corrected by the atmospheric differential refraction, caused by the atmosphere refraction index dependence on the wavelength, making the source have different centroids across the data cube. The individual data cubes exposures were combined using their median. Infrared data cubes were resampled to the $0.0625''$/spaxel scale since, in that way, the structures can be better resolved. Optical data was maintained at $0.05''$/spaxel.

The following steps are related to the high frequency spatial and spectral noises. The nature of the high-frequency spatial noise can be instrumental due to low statistics of photons or even introduced by the resampling. This noise can be identified through the Fourier transform, which transform the image from spatial to frequencies domain, and is removed applying a spatial Butterworth filtering (Gonzalez, 2009). A Butterworth filter is a low-pass filter that can suppress the high-frequency components depending on the chosen cut-off frequency and index filter. After, an inverse Fourier transform is made to return to the spatial domain. The instrumental fingerprint is caused by the telescope geometry and can drastically affect the data cubes. It causes wide stripes in the images and large ripples in the spectra. In order to remove that, we use the principal component analysis (PCA) Tomography (Steiner et al., 2009). The PCA Tomography is a linear transformation that

decomposes our data into the autovectors or principal components on a new orthogonal basis. With this technique, we can isolate the fingerprint effects hidden in the data cube and construct fingerprint data cubes to be subtracted from the science data cubes. Later, the Richardson-Lucy deconvolution (Richardson, 1972; Lucy, 1974) was applied to improve the spatial resolution. The Richardson-Lucy deconvolution is an attempt to recover the real image if the point spread function (PSF) that degrade the astronomical images is known and assumes a Poissonian noise. Finally, the science data cubes are ready for analysis.

2.2 Methods

To analyse the scientific data many python modules were developed. I intend to fully document the codes to make them publicly available to the community. Also, it was made use of public codes and modules, most of them briefly mentioned in the following sections (e.g., `STARLIGHT`, `pPXF`, `IFSCUBE`, `astropy`, `PyNeb`). Additional information about error propagation, centroid, and spatial resolutions considered are presented in appendix A.

2.2.1 Stellar Population Synthesis and the Pure Emission Lines Data Cubes

The spectra of galaxies usually are a superposition of stellar continuum and absorption lines, emission lines from ionized gas, and featureless continuum from the AGN. In our case, the AGN continuum is not detected in the spectra due to the high nuclear obscuration. To separate the stellar contribution is the first critical approach because it weakens the emission lines. We can also extract relevant information about the stellar populations and their kinematics from their spectra.

A technique to model the stellar content in galaxies is the synthesis of stellar populations. The method consider the stellar continuum as a combination of simple stellar populations (SSPs). Each SSP is the integrated spectra of an entire stellar population and is like an ideal stellar cluster. Composed of stars of the same age and metallicity, but different stellar masses following the initial mass function (IMF) [2]. Since the stellar spectra of galaxies are a combination of the stars in them, born in star clusters, weighing different SSPs contributions can model the whole spectra and unveil detailed information about the

[2] The initial mass function (IMF) defines the fraction of stars at each mass in a population.

stellar content of the galaxy. The synthesis makes it possible to obtain, for example, the star formation history (SFH), which summarizes the past events of star formation. Also, from the fit of the absorption lines, we can obtain the stellar kinematics and disentangle the emission lines.

To model the optical stellar continuum was used up to 350 MILES SSPs models (Vazdekis et al., 2010), which are a combination of empirical stellar observations, theoretical isochrones, and the IMF. The adopted stellar base makes use of Padova isochrones and Chabrier IMF with ages ranging from 63 Myr $\leq$ t $\leq$ 17.78 Gyr and seven metallicities Z ($Z_{\odot}$) $\approx$ 0.005, 0.019, 0.049, 0.195, 0.398, 1.000, 1.660. The spectral resolution is FWHM $\approx$ 2.5 $\mathring{A}$. In the NIR were not used SSPs as a base. For the K-band a stellar library was used, consisting of 20 stars in the spectral range of λ : 2.04 - 2.43 μm observed with the instrument NIFS at Gemini telescope (Winge et al., 2009). This stellar library has a spectral resolution of FWHM $\approx$ 3.2 $\mathring{A}$. To remove the stellar contribution in the H-band, a low-order Spline fit was performed.

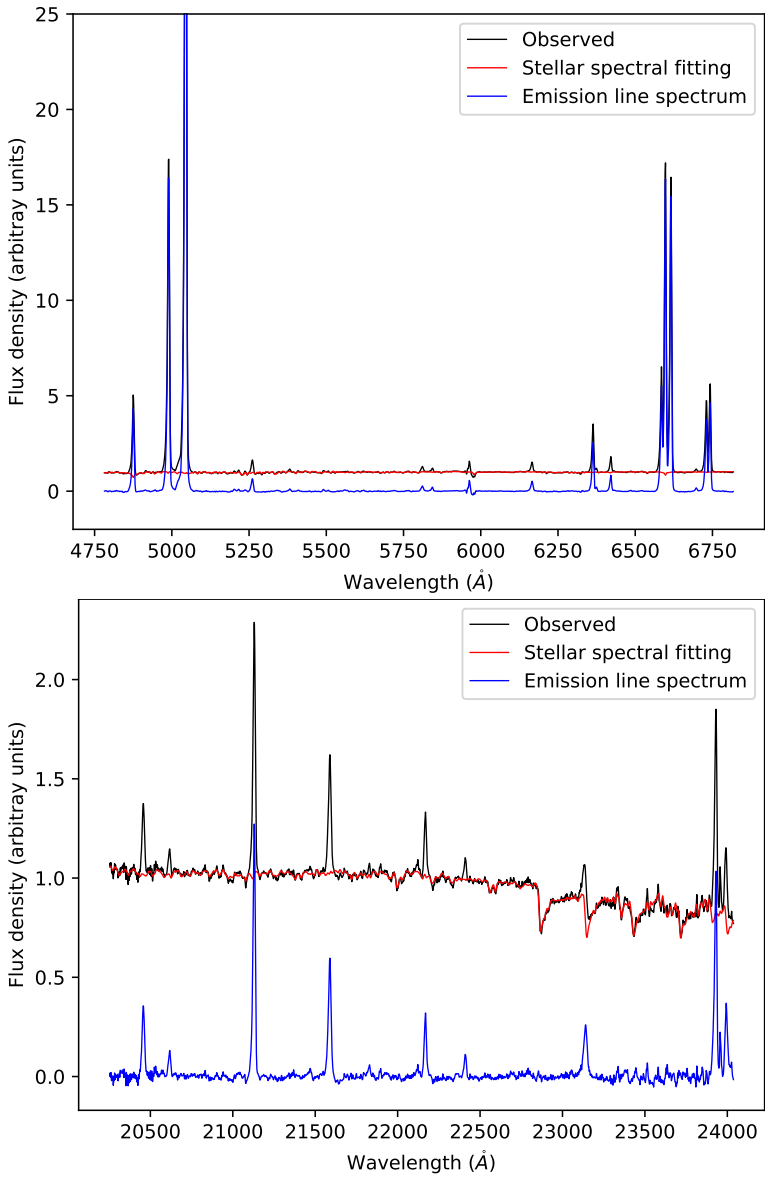

Figure 2.4: Central spaxel spectra of NGC 5643 for the optical GMOS data cube (upper panel) and the NIR K-band from SINFONI (bottom panel). The plots show the observed spectra (black lines), the stellar fits (red lines) made with the `pPXF` code, and the stellar libraries of NIFS and MILES, respectively, and the residual spectra (blue) with the emission lines.

To unveil the stellar populations in the galaxy was used the `STARLIGHT` code (Cid Fernandes et al., 2005) to fit the optical data cube with 200 MILES SSPs. `STARLIGHT` fits our data with a Markov Chain Monte Carlo technique trying to minimize the χ^2 using a model spectrum. The model spectrum takes into account the base SSPs weighted by their light fraction contribution (x_j) and the dust attenuation (A_λ). The whole model spectra are convoluted by the velocity field represented by a Gaussian filter $G(v_*, \sigma_*)$. The selected base spectra consist of 50 ages between 63 Myr $\leq$ t $\leq$ 17.78 Gyr and the four metalicities Z ($Z_\odot$) = 0.19,0.40,1.00,1.66. Here just the nuclear, estimated from FWHM([OI]λ 6300)

$\approx 0.7\,''$, circumnuclear stellar populations were fitted, and an SFH was built.

The stellar kinematics was extracted from the K-band SINFONI and optical GMOS data cubes using the Penalized Pixel-Fitting (`pPXF`) (Cappellari and Emsellem, 2004; Cappellari, 2017) synthesis code. The observed spectrum is modeled fitting it with stellar templates, similar to `STARLIGHT`, but convoluted with a velocity distribution described in terms of Gauss-Hermit functions. In order to fit the kinematics, it was required to match the spectral resolutions, with the NIFS stars library convoluted to $FWHM \approx 5\mathring{A}$ and the GMOS spectra for FWHM $\approx 2.5\ \mathring{A}$. The outputs are the velocity, dispersion, h3 and h4 coefficients. The h3 and h4 coefficients measure the asymmetric and symmetric deviations from a Gaussian profile.

Beyond the velocity distribution, `pPXF` can apply additive and/or multiplicative Legendre polynomials. The additive polynomials can tune the line strengths, when an incompatibility between the base and observed spectrum, and regarding bad sky subtractions. On the other hand, multiplicative polynomials can help to correct inaccurate wavelength calibration and make the fit independent of reddening. All these features make the kinematics obtained with `pPXF` less noisy. Examples of fits are presented in figure 2.4. Results of the stellar kinematics and their errors are in appendix B.

The code `PPXF` was used again to obtain the pure emission lines spectra, free from stellar contribution. This time no additive polynomials were applied since they can interfere in the strength of the lines. The procedure for the optical data cube is the following. A first run was made with the 23 most relevant SSPs for the nuclear spectrum at a fixed error. These fits estimate the input errors for a new run, now with all 350 MILES SSPs. Later on, the resulting emission lines data cube is the treated cube minus the stellar fits ones.

2.2.2 Emission Lines Fitting

We measured the emission lines from the pure emission lines data cubes fitting one or more Gaussian components. For that was used the code `IFSCUBE` (Ruschel-Dutra and de Oliveira, 2020a). The code can fit with Gaussians or Gauss-Hermite polynomials entire data cubes (`cubefit`) or individual spectra (`specfit`), with different possible minimizations in combination with Monte Carlo simulations to estimate the uncertainties. The procedure adopted used a least-squares fit with 30 Monte Carlo iterations. The data

cube, a variance cube, and a configuration file or python script that sets the features and parameters are given as input. The output is a fits file with the spectra and continuum fits, solution parameters for amplitude, v, σ, their errors, and the line fluxes. The procedure adopted to calculate the flux errors is in appendix A.1.

Until the final version, many different settings and constraints were tested for each set of emission lines. The definite procedure to fit data cubes follows. First, the [OIII]$\lambda\lambda$4959,5007 components were fitted together preserving the ratio $[OIII]\lambda4959 = [OIII]\lambda5007/3$. The H$\alpha$, H$\beta$, [NI]$\lambda$5199, [NII]$\lambda\lambda$5755,6568,6583, [OI]$\lambda\lambda$6300,6364 and [SII]$\lambda\lambda$6717,6731 were fitted with the same kinematics. The ratio $[NII]\lambda6583 = [NII]\lambda6548/3$ was given by the ratio of their transition probabilities (Osterbrock and Ferland, 2006, Section 5.2). The coronal line of [Fe VII]λ 6086 was modeled alone, and the K-band molecular lines of H_2 were all fitted together. Optical lines were fitted with -400 km/s $\leq v \leq$ 400 km/s and $\sigma \leq$ 400 km/s. On another hand, the molecular ones present best fits -250 km/s $\leq v \leq$ 250 km/s and $\sigma \leq$ 250 km/s. The most successful fits was found using a narrow Gaussian component plus a slightly broader component, the last probably representing gas in outflow. For the weak emission lines, as Hβ, [NI]λ5199, and for molecular H_2 lines, the best fits were obtained from fitting a single Gaussian component.

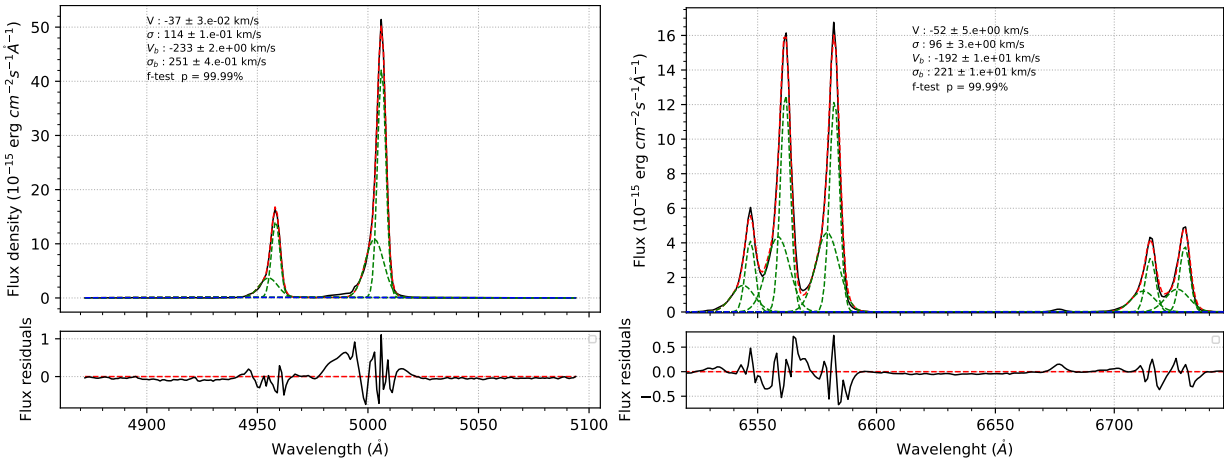

Figure 2.5: Nuclear spectrum of NGC 5643 (D = 0.62″) with two Gaussian components fits showing the [OIII]$\lambda\lambda$4959,5007 (left) and [NII]$\lambda\lambda$6568,6583, Hα and [SII]$\lambda\lambda$6717,6731 (right) emission lines. The observed spectrum is shown as a black line, and the Gaussian components and total models as green and red lines, respectively. The broader Gaussian component, modeled in terms of v_b and σ_b, is probably part of a blueshifted outflow.

Extractions were made to overcome the lower signal in the borders of the field and detect fainter emission lines, as [Fe VII]λ6086. We define the regions based on the

ionization cone limits, and the procedure is described in section 3.3. The fit of the nuclear extraction spectrum of NGC 5643 is shown in figure 2.5. They were fitted with one up to three Gaussian components. The velocity and sigma ranges are the same used in the fits for spaxels. In the case of three components, a narrow Gaussian was always at lower velocities in relation to the broader components, that were constraint to be one in blueshift and other in redshift relative to the narrow. To evaluate how many components provide the best fits statistically a F-test was implemented and applied to each extraction as explained in appendix A.3.

2.2.3 Extinction

The dust in the galaxy, in the way of light, scatters and absorbs the observed radiation, the commonly called interstellar absorption (Osterbrock and Ferland, 2006, Section 7.2). Considering just the light getting absorbed and scattered from the beam of light we can obtain the relation :

$$I_\lambda = I_{\lambda 0} e^{-\tau_\lambda} \tag{2.1}$$

Where the intensity $I_{\lambda 0}$ decay exponentially with the optical depth τ_λ [3] , that is a function of the wavelength. Normally it is assumed that $\tau_\lambda = C \cdot f(\lambda)$, where C is a constant calibrated to each spectra and $f(\lambda)$ an extinction law. A technique to infer the constant is using the Balmer decrement, that consist to calculate the ratios between balmer series lines, that is theoretically know, to infer C. Like for $H\alpha$ and $H\beta$:

$$\frac{I_{H\alpha}}{I_{H\beta}} = \frac{I_{H\alpha 0}}{I_{H\beta 0}} 10^{-c[f(H\alpha)-f(H\beta)]} \rightarrow c = \frac{1}{f(H\alpha)-f(H\beta)} log_{10}\left(\frac{I_{H\beta 0}\cdot I_{H\alpha}}{I_{H\alpha 0}\cdot I_{H\beta}}\right) \tag{2.2}$$

Where c = 0.434C and the property $e = 10^{log_{10}(e)}$ was used. Now assuming a $f(\lambda)$ and measuring $H\alpha$ and $H\beta$ intensities or fluxes it is possible to infer the extinction and correct the emission lines :

$$\begin{aligned} F_{\lambda 0} &= F_\lambda \cdot 10^{c\cdot f(\lambda)} \\ A_\lambda(\text{mag}) = 2.5\log\left(\frac{\mathrm{I}_\lambda}{\mathrm{I}_{\lambda 0}}\right) &= -2.5\cdot \mathrm{c}\cdot \mathrm{f}(\lambda) \end{aligned} \tag{2.3}$$

[3] The optical depth is defined as : $\tau_\nu(s) = \int_{s0}^{s} \alpha_\nu(s')ds'$, where α_ν (absorption coefficient) in integrated along the way of light to the LOS (Rybicki and Lightman, 1979, Section 1.4).

To account for this extinction the Balmer decrement method was applied using the $\frac{H\alpha}{H\beta} = 3.1$ and the extinction law of Cardelli et al. (1989). For AGNs the ratio is $\frac{H\alpha}{H\beta} = 3.1$, different from star-forming galaxies ($\frac{H\alpha}{H\beta} = 2.87$), because the H$\alpha$ can be produced collisionally in the partly ionized region (Osterbrock and Ferland, 2006, Section 14.6). Finally we obtain the extinction maps, corrected emission lines fluxes and propagated errors presented in appendix A.1.

Extinction correction was also applied to the optical data cube to make unreddened channel maps. Channel maps are intensity maps produced for different spectral frames across the emission line, evincing different gas velocities. The velocities considered were calculated concerning the nuclear stellar velocity, and spaxels presenting SNR ≤ 10 were masked, according to the procedure of appendix A.2.

2.2.4 Electron Density and Temperature Diagnostics

Pairs of forbidden lines of the same ion, to avoid abundances dependence, and excitation potential, but different critical densities can be used to determine electron densities. We can use the [SII]$\lambda\lambda$6716,6731 doublet of critical densities $n_c(6716) = 1.5 \cdot 10^3 cm^{-3}$ and $n_c(6731) = 3.9 \cdot 10^3 cm^{-3}$ as example. When $n_e \ll 10^3 cm^{-3}$, low-density regime for both lines, their ratio tend to F(6716)/F(6731) = 1.44. At high density case $n_e \gg 10^3 cm^{-3}$ the ratio becomes F(6716)/F(6731) = 0.44 (Peterson, 1997, Section 6.2.1). But, for densities in between $n_e \approx 10^3 cm^{-3}$, the ratio becomes a function of the density. The [SII] doublet, in particular, is suitable to infer low-density values between $10^2 cm^{-3} \ll n_e \ll 10^4 cm^{-3}$. This is possible since one emission line is in the low-density regime while the other is being suppressed by collisions, in the high-density regime.

Electron temperature is another physical property that can be measured using forbidden lines of the same species. The transitions need to have different excitation potentials, like for [OIII]$\lambda\lambda$4363,4959,5007 and [NII]$\lambda\lambda$5755,6548,6583 lines. For [NII]$\lambda\lambda$5755,6548,6583 the relations becomes (Osterbrock and Ferland, 2006, Section 5.2):

$$\frac{[NII]\lambda6548 + [NII]\lambda6583}{[NII]\lambda5755} = \frac{8.23e^{2.50 \cdot 10^4/T}}{1 + 4.4 \cdot 10^{-3} n_e / T^{1/2}} \tag{2.4}$$

That is also dependent on the electron density. If we can measure the density, like using [SII]$\lambda\lambda$6716,6731, we can obtain T_e, under the assumption that both

[NII]$\lambda\lambda$5755,6548,6583 and [SII]$\lambda\lambda$6716,6731 are being produced in the same zone. This assumption cannot be such a good approximation when T_e is estimated from [OIII]$\lambda\lambda$4363,4959,5007.

Steiner et al. (2009) proposed to apply a linear transform to obtain maps of low and high density. There is a transformation from a base of the two lines map [SII]$\lambda\lambda$6716,6731 to a base of two density modes, of low and high density. It can also be viewed as a decomposition of the intensity map of the high critical density line [SII]λ6731 into low and high-density intensities maps. This diagnostic is a valuable qualitative tool for spatially resolved data. For the [SII]$\lambda\lambda$6716,6731 doublet, the low-density map corresponds to $n_e \leq 81\ cm^{-3}$ and for the high-density $n_e \geq 5.9 \cdot 10^3\ cm^{-3}$. Spaxels in both maps are probably of intermediate projected densities.

To quantitatively determine both electron density and temperature was used the python library `PyNeb` (Luridiana et al., 2015). The code solves the levels population equations for the ions, usually 5-6 levels for each one, to different T_e and n_e, to compute their emissivities. Many nebular diagnostics are available. Here was used the routine `getCrossTemDen` for iteractively get both T_e and n_e using the emission lines of [NII]$\lambda\lambda$5755,6548,6583 and [SII]$\lambda\lambda$6716,6731, respectively. Also was applied the routine `getTemDen`, with fixed $T_e = 10000$ K and computing the density with [SII]$\lambda\lambda$6716,6731. The errors were estimated from the emission lines errors to save computing time. Comparing these error estimates to Monte Carlo simulations using 417 spaxels, it was found that Monte Carlo errors tend to be higher. For 90% of the spaxels, Monte Carlo estimated errors do not exceed our errors in more than 30%.

2.2.5 Optical Excitation Diagnostics

The strength of emission lines relative to hydrogen lines or transitions of the same atom is good diagnostics of the source of ionization. The $[OIII]/H\beta$, for example, is a proxy to the mean level of ionization. At the same time, $[SII]/H\alpha$ and $[OI]/H\alpha$ can be enhanced in regions with higher partially ionized zone contribution (Osterbrock and Ferland, 2006, Section 14.3) or even associated to shocks.

Diagnostic diagrams are a tool to separate the main ionization mechanisms behind the nebular emission. They often combine different line ratios capable of separating different classes. The [OIII]$/H\beta$ against [NII]$/H\alpha$ (BPT, or hereafter N-BPT) was first proposed by Baldwin et al. (1981). Later, the diagrams of [OIII]$/H\beta$ against [SII]$/H\alpha$

(hereafter S-BPT) and [OI]/$H\alpha$ (hereafter O-BPT) were proposed by Veilleux and Osterbrock (1987). The diagrams are combined with empirical and theoretical models to distinguish star-forming from Seyferts and LINERs. Kewley et al. (2001) produced photoionization models to constraint the ratios of an extreme Starburst to divide the region of pure star-formation from the others. The studies advance with the Sloan Digital Sky Survey (SDSS, York et al. 2000), which made available hundreds of thousands of spectra of galaxies. Kauffmann et al. (2003) derived an empirical branch of star-forming galaxies using more than 20000 galaxies from SDSS. The Seyfert-LINER separations used here were proposed in Kewley et al. (2006). We also made use of a Seyfert-LINER separation in the N-BPT that was proposed in Cid Fernandes et al. (2010).

To investigate the nuclear and circumnuclear activity mechanisms acting in NGC 5643 was built diagrams for the optical datacube. Many recent infrared and optical studies explore spatially resolved diagnostic diagrams and excitation diagnostics (da Silva et al., 2020; Riffel et al., 2021; Ma et al., 2021; Venturi et al., 2021). Unlike a single integrated spectrum, like from SDSS 3″ fibre, we had thousands of spectra, allowing much more detailed information from the source. There is also expected that the transition objects, frequently found in the BPT diagram, are just mixed in the integrated spectra and can be solved in high spatial resolution (Ricci et al., 2021; Menezes et al., 2021).

Chapter 3

Results

Since the main aims of the project are on the gas properties, this will be our focus in the following sections. The extra results obtained for the stellar populations and kinematics are in appendix B.

3.1 Emission Line Spectra

From the subtraction of the stellar spectra modeled with `pPXF` we obtain the pure emission-line data cube. Figures 3.1 and 3.2 present the optical, H-band, and K-band nuclear spectra. The nuclear position for each data cube and spatial resolution estimates are presented in appendix A.4.

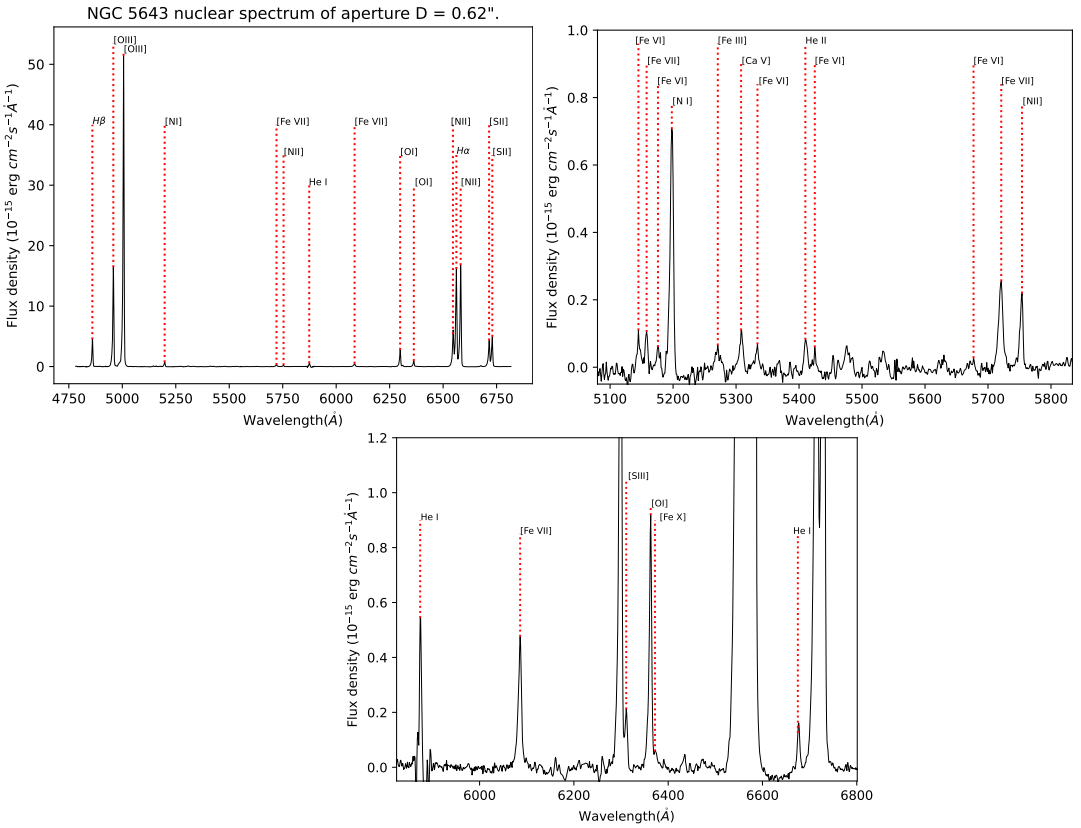

Figure 3.1: The optical nuclear spectrum of NGC 5643 with an aperture diameter of 0.62″. The main emission lines of the spectrum were labeled. The enlarged spectra on the right and bottom panels reveal fainter nuclear emission lines.

The optical nuclear spectrum of figure 3.1 shows a diversity of emission lines. The most traditional and intense ones, like [OIII]λ5007, [NII]$\lambda\lambda$6568,6583, and [SII]$\lambda\lambda$6717,6731 doublets and Hα, will be essential for the complete analysis. Other less common features are also present. Fe^{+6}, for example, is detected in three wavelengths, being the stronger [Fe VII] λ6086 coronal line analyzed in detail in the following sections. The weak and extended [NII]λ5755 allows the estimate of electron temperature. Other faint lines are typically seen in AGNs, most of them too weak or absent in the circumnuclear spectra. Examples are [Ca V]λ5309, He IIλ5412 and [Fe X]λ6374.

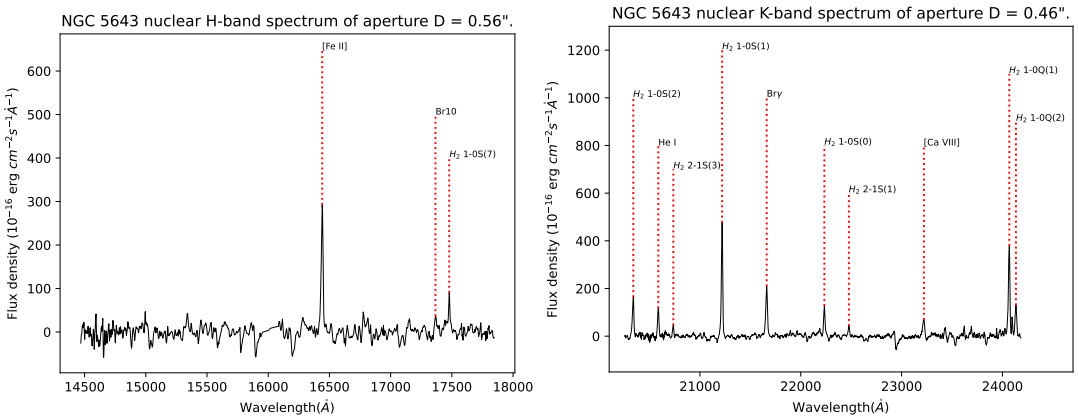

Figure 3.2: Nuclear H-band and K-band spectra with diameter apertures of 0.56″ and 0.46″. The main NIR emission lines were labeled..

Other important emission lines come from the NIR spectra, as shown in the figure 3.2. In the H-band, the bright low-ionization [Fe II]λ16440 helps us to see the NLR with less dust attenuation. In the K-band, besides the Brγ and the weak coronal line of [Ca VIII]λ23210, there are many H_2 molecular emission lines, allowing us to map and better extract their kinematics.

3.2 Channel Maps

Channel maps of emission lines are used to study the distribution and kinematics of the gas, showing in each wavelength slice regions of the field that emits in that velocity range. The channels were made from the pure emission lines data cubes, with the optical one also corrected for extinction. Only spaxels with SNR ≥ 10 were considered as explained in appendix A.2. Individual maps of an emission line were normalized in flux relative to the lower velocity map. Then, brighter structures in a specific velocity range map can be compared to the other maps. All velocities were considered relative to the nuclear stellar velocity obtained with `pPXF` at the nuclear extraction. A limitation of the method is that lines that are too close in wavelength (i.e. blended), result in an ambiguous channel map. For those cases, like [SII]$\lambda\lambda$6717,6731, the maps were restricted in velocity range to avoid significant contamination. The optical maps have a mask of diameter 0.6″ in the central region to show the fainter structures better.

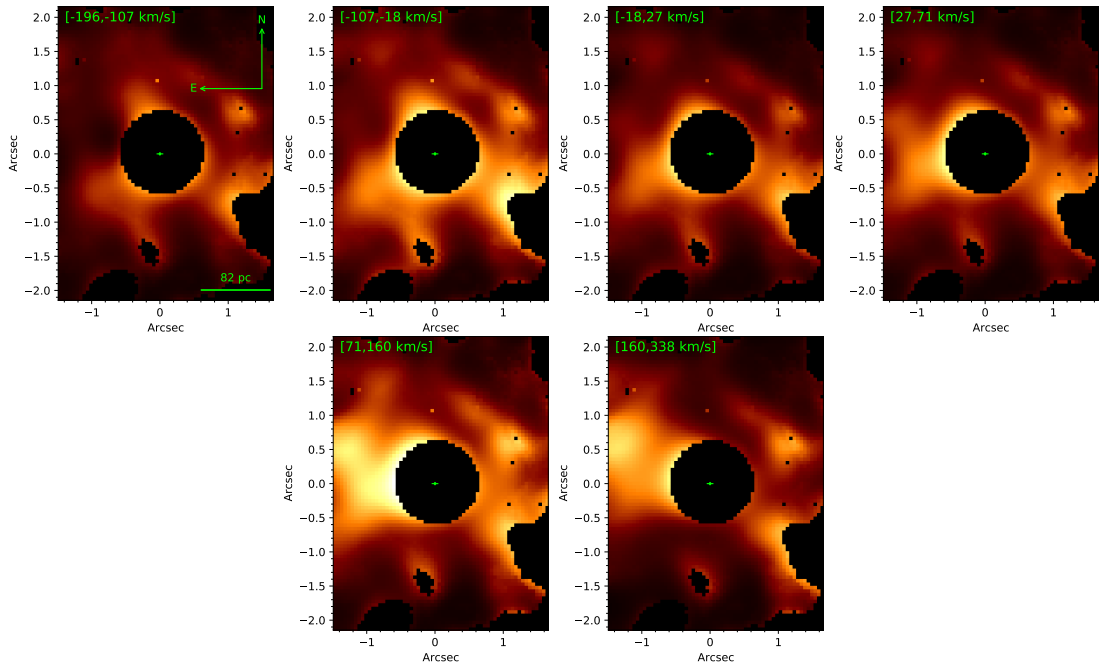

Figure 3.3: Channel maps of the [SII]λ6731 emission line. The individual map fluxes were normalized to the flux range of the lower-velocity map, allowing the comparison of flux between different maps. A mask of diameter 0.6″ was used in the nuclear region to allow us to analyze the fainter extended structures. Values between brackets on the left side of each map indicate the range of velocities of the gas. Spaxels with SNR $<$ 10 were masked.

Tracing the low ionized gas, the channels of the [SII]λ6731 are in figure 3.3. Other optical emission lines present similar behavior. The ionization cone towards the east has most of its emission redshifted with $v_{[SII]\lambda6731} \leq$ 338 km/s and $v_{[NII]\lambda6583} \leq$ 315 km/s. In addition, the possible western cone appears present in almost all velocities. Blueshifted gas achieves high velocities as for -716 km/s $\leq v_{[SII]\lambda6716} \leq$ -2 km/s and show an arc shape morphology. The southeast part of the arc is brighter than the northeast. This can be because the northeast region is on the farther side of the galaxy. Channel maps do not show the [OIII]λ5007 clearly, but suggest evidence that can have a wider velocity range than the other lines as -1006 km/s $\leq v_{[OIII]\lambda5007} \leq$ 731 km/s.

The [Fe II]λ16440 channel maps reveal, in figure 3.4, in a larger FoV and with lower dust attenuation, the NLR structure. The redshifted channels in the velocity range 100 km/s $\leq v_{[FeII]\lambda16440} \leq$ 420 km/s are filling the eastern ionization cone. On another hand, blueshifted gas is in an arc shape that makes the cone boundaries at -583 km/s $\leq v_{[FeII]\lambda16440} \leq$ -82 km/s. In constrast, the opposite occur at the western side. Redshifted gas are tracing the external regions in 55 km/s $\leq v_{[FeII]\lambda16440} \leq$ 283 km/s while the blueshifted ones in -401 km/s $\leq v_{[FeII]\lambda16440} \leq$ -82 km/s are inside the cone.

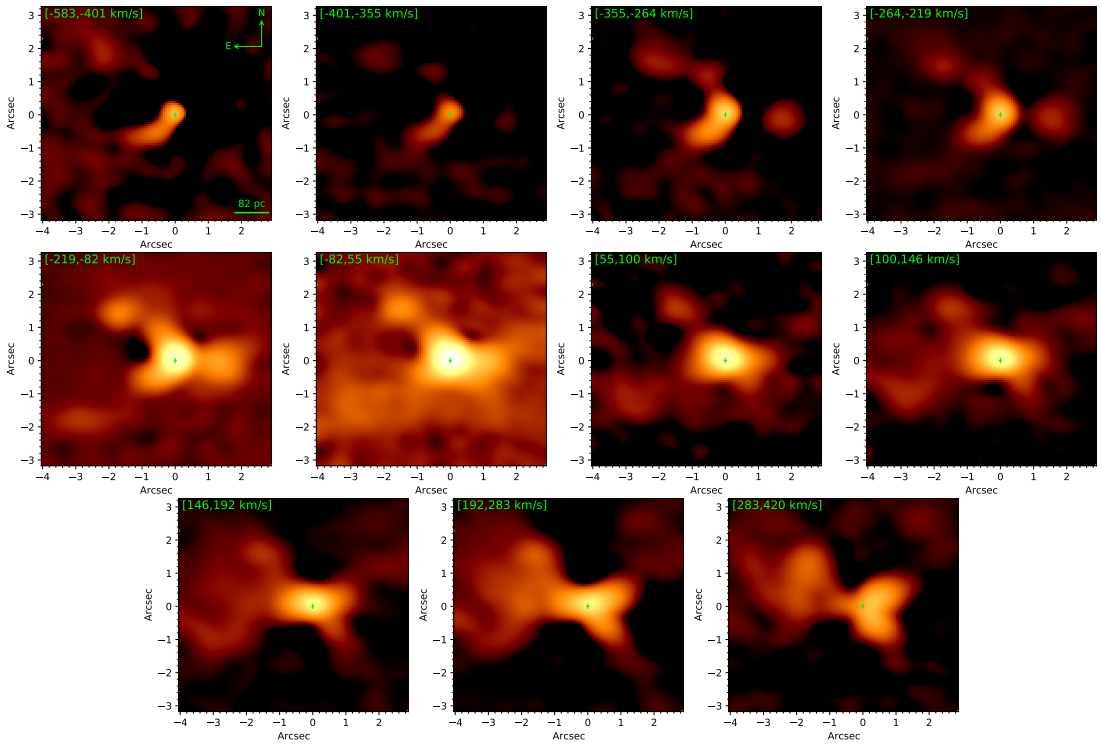

Figure 3.4: Channel maps of the [Fe II]λ16440 emission line. The individual map fluxes were normalized to the flux range of the lower-velocity map, allowing the comparison of flux between different maps. Values between brackets on the left side of each map indicate the range of velocities of the gas. Spaxels with SNR < 10 were masked.

The ionized optical and NIR channels appear to reveal an ionization bicone structure. [Fe II]λ16440 line channels incremented the optical information, getting a clearer view of the western cone. At the same time, it revealed the hourglass shape that is possibly tracing the walls of the ionization cones.

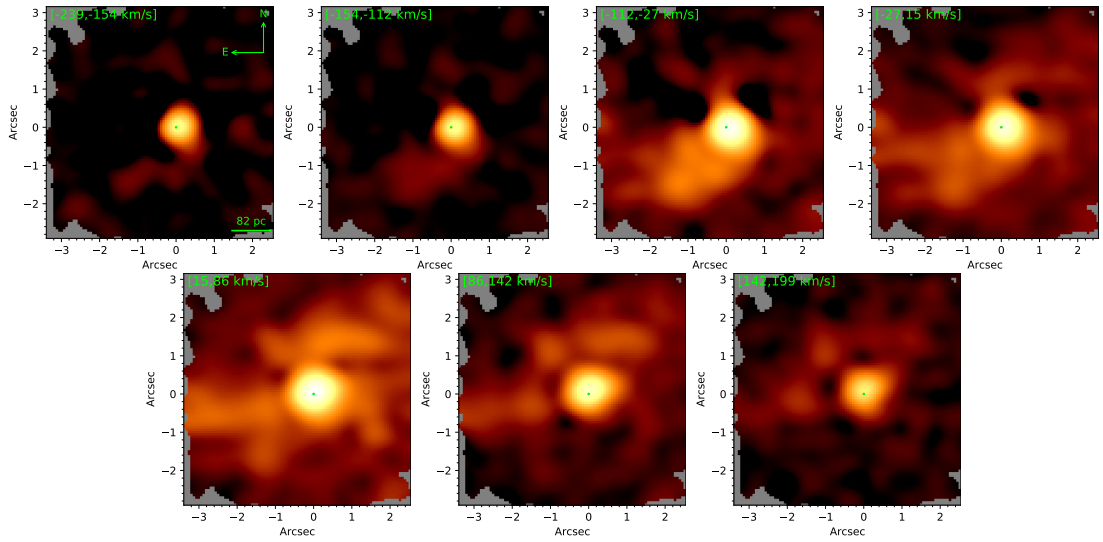

Figure 3.5: Channel maps of the $H_2\lambda$ 21218 emission line. The individual map fluxes were normalized to the flux range of the lower-velocity map, allowing the comparison of flux between different maps. Values between brackets on the left side of each map indicate the range of velocities of the gas. Spaxels with SNR < 10 were masked.

The channel maps of $H_2\lambda21218$ are presented in figure 3.5. The bulk of the molecular emission looks perpendicular to the ionization cones axis. However, some emission as well exists in the bicone direction. Like the hook shape in the western side between -112 km/s $\leq v_{H_2\lambda21218} \leq$ 86 km/s and the redshifted excess noted in the region of the east cone 86 km/s $\leq v_{H_2\lambda21218} \leq$ 199 km/s. Moreover, the emission toward the southeast occupies the same locus as the ionized gas closer to the wall of the bicone in -154 km/s $\leq v \leq$ 142 km/s.

To summarize the velocity channels, a series of RGBs are present in figure 3.6 indicating the distribution of gas divided into three bands normalized individually. In this way, each band traces the gas distribution and shows even the fainter structures. A comparison between the fluxes of each band, however, cannot be done from these maps. The previously shown channel maps were developed for this purpose. The green map shows gas with velocities closer to the range -200 km/s $\leq v \leq$ 200 km/s. This boundaries were considered like a reasonable threshold for the rotating gas due the typical stellar velocities of about $|v_\star| \simeq$ 60 km/s and $\sigma_\star \simeq$ 70 km/s presented in appendix B.

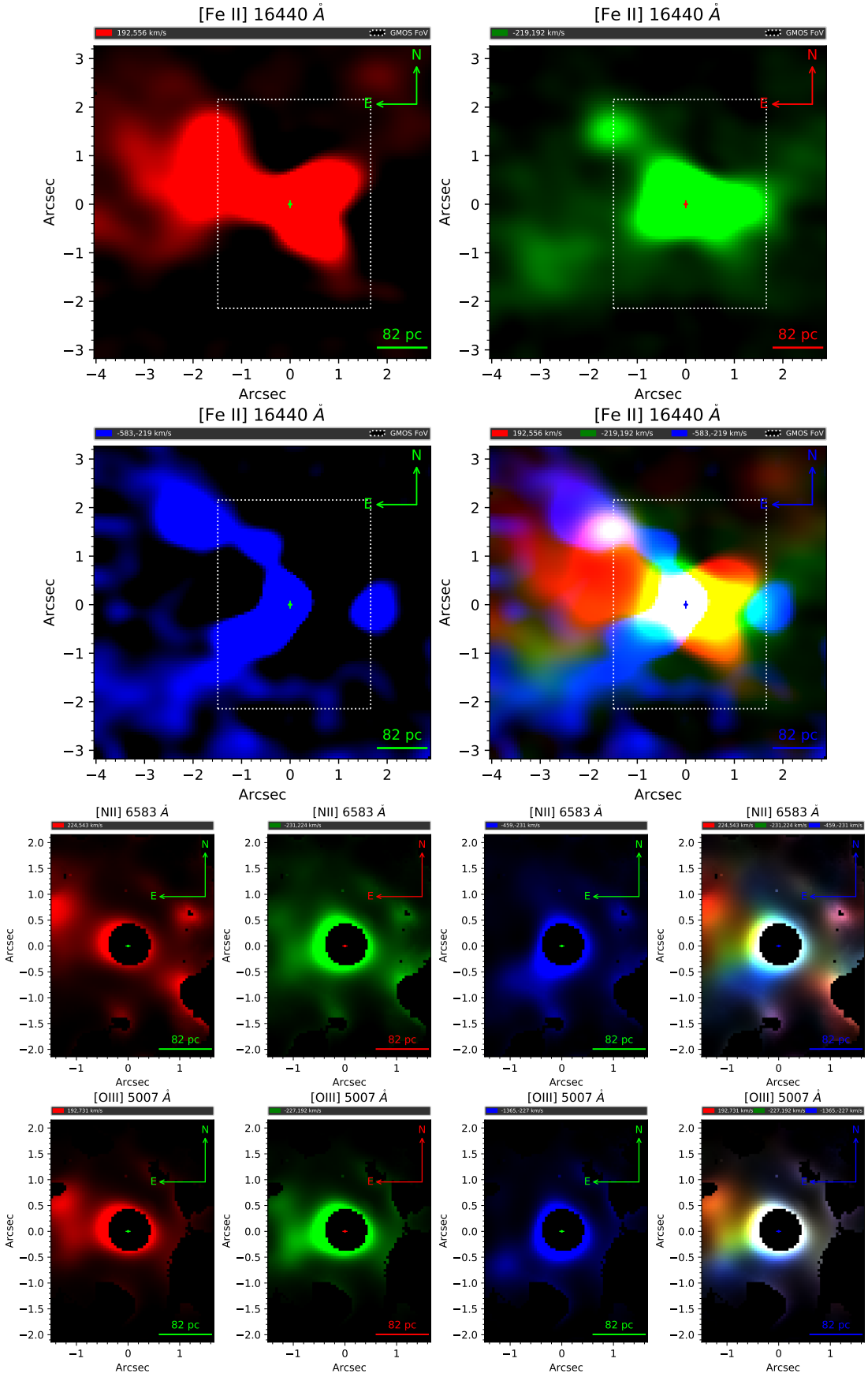

Figure 3.6: RGB images of [Fe II]λ16440, [NII]λ6583 and [OIII]λ5007. The white dashed box in the [Fe II] show the GMOS FoV. The image colors show the ionized gas likely under rotation (green, -200 km/s $\leq v \leq$ 200 km/s), and probably outflowing gas in blueshift (blue, v < -200 km/s) and redshift (red, v > 200 km/s). The individual band fluxes were normalized individually, revealing the distribution of each component of the gas.

The overall kinematics shown in figure 3.6 is consistent between optical and NIR lines. The gas in the walls had a different behavior than the inner bicone regions. A significant result is the nature of the ionized gas kinematics. The green map shows gas with low velocities that could be rotating and evince the emission across the overall bicone. Inside the cones boundaries, the green map shows that its contribution becomes fainter far away from the AGN, as seen in [Fe II]λ16440. The redshift and blueshift maps, showing the high velocities, maybe are related to outflowing gas. These outflows achieve the maximum projected velocities when directed to our LOS, which is possibly in the southeast region. The outflows are not exclusively detected on [OIII]λ5007, but also in the recombination lines as $H\alpha$, low-ionization lines as [SII]$\lambda\lambda$6717,6731 and neutral atomic lines as [OI]$\lambda\lambda$6300,6364. The issue of outflows in the coronal and molecular gas will be treated in the following sections.

Figure 3.7 displays some [Fe II]λ16440 channel maps associated with the bicone walls and their superposed fits. Overall morphology suggests two paraboloids rather than cones. The procedure consisted in adjusting ellipsoidal arcs to the emission features of the bicone walls. The full white curve represents an ellipsoidal arc of $3'' \approx 261$ pc height, and $8'' \approx 696$ pc width and an overall orientation that matches the Fischer et al. (2013) model with PA $= 80°$. It is difficult to obtain the PA of the walls since the aperture is not equal in all scales, unlike a regular bicone. Looking to maps at different velocities, the aperture of the cones also appears to be slightly different.

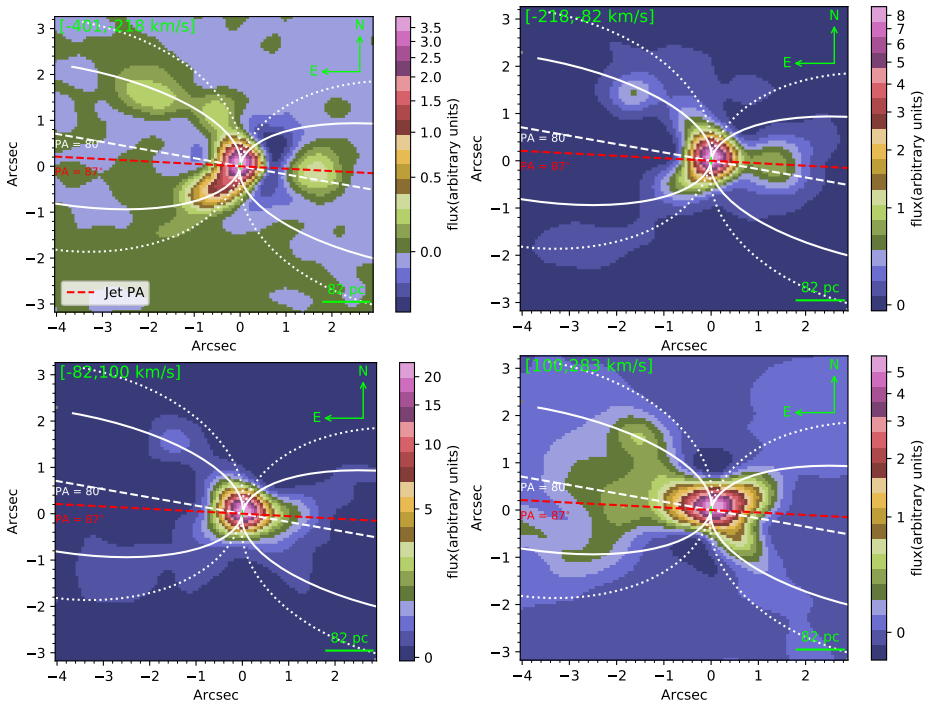

Figure 3.7: [Fe II]λ16440 channel maps showing the curve drawn to the ionization cone walls. The full curves are the arc fit to the hourglass structure, and the dashed hourglass is an upper limit that includes almost all emissions coming from the walls. The dashed lines indicate the ionization cones (white line, PA = 80°) and radio jet (red, PA = 87°) orientation.

The limits above will be necessary for the upcoming sections. They will be used in the following results to make better spatial comparisons and analyze the emission enclosed in the ionization cones and outside them.

3.3 *Emission Line Fitting and Spectra Extractions*

In order to model the emission-line fluxes and disentangle the kinematics in terms of Gaussian components, the code `IFSCUBE` (Ruschel-Dutra and de Oliveira, 2020b) was used. The fits made for spaxels consists of one or two Gaussian components. One of these components, referred to as broader or wing, is necessarily broader than the ordinary one. This component is often shifted to high velocities, interpreted as tracing an outflow. The broader component, although, was not constrained to be shifted relative to the narrow, to allow the component to freely be fitted in redshift or blueshift. We made a series of runs to obtain the best fits, and the procedure is explained in section 2.2.2.

Solving the emission spatially through the spaxels is one of the best ways to extract information from data cubes. However, this also carries limitations. The SNR is typically

worst in the borders of the field, and some fainter lines, like [Fe VII]λ6086 or [NII]λ5755 can have low SNR there. To overcome this problem, extractions were made across the optical field following the ionization cones boundaries previously shown in figure 3.7. The extractions scheme is in figure 3.8.

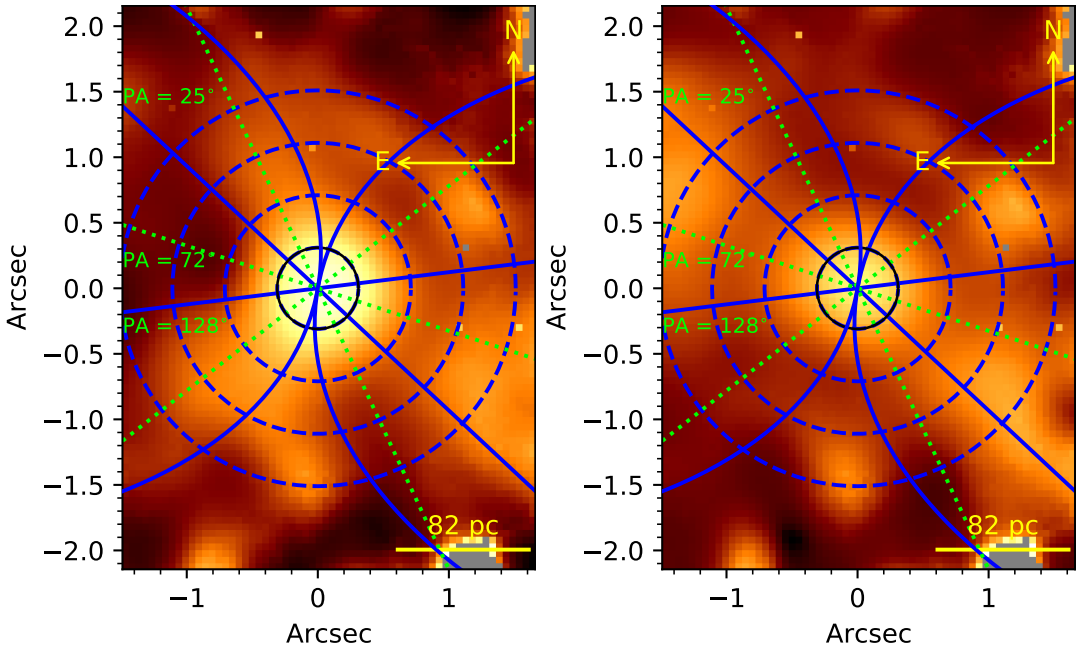

Figure 3.8: Scheme of the 32 extractions defined on the GMOS FoV. The blue lines (dashed and solid) represent the boundaries of the extractions. The solid lines constrain the region of the ionization cones. The extractions cover the ionization cones and the cross-cone region. More extractions are at the bicone, with 3 different average orientations : $\langle PA \rangle = 25°$, $\langle PA \rangle = 72°$ and $\langle PA \rangle = 128°$. In the background is the [NII]λ6583 maps between velocities of -529 km/s $\leq v \leq$ -203 km/s on the left and 142 km/s $\leq v \leq$ 343 km/s on the right. This plots evinces the necessity of more extractions along the ionization cones to catch their line variation.

The emission properties in the ionization bicone direction do not change only with the radial distance, but also depend on its PA. This difference of emission can be seen in the maps of [NII]λ6583 in the background of figure 3.8. Because of that, the cones are divided in three main regions: $\langle PA \rangle = 25°$, $\langle PA \rangle = 72°$ and $\langle PA \rangle = 128°$. The more external position angles to eastern side are regions showing more emission coming from the low-ionization lines and with blueshifted velocities. In contrast, the central cones at $\langle PA \rangle = 72°$ normally present the higher ionizing level, like from [OIII]λ5007 and [Fe VII]λ6086, with redshifted velocities.

Extractions are also good to support the resolved maps, helping to understand the general trend and with higher confidence in the individual fits. The extractions were made in order not to be too big, avoiding the dilution of information, and each extraction

having at least SNR = 10 in the window 5086-5126 $\mathring{A}$. Also, the extractions are radially distributed so that it is possible to build radial profiles. Each annulus has a radial thickness of 0.4", except for the external ones, which are bigger to increase the SNR of the borders. In this way, there are 32 extractions divided between the east-west cone, subdivided into three mean position angles, and the south-north cross-cone region. The SNR varies from 71 (west cone, $\langle PA \rangle = 128°$, $\langle r \rangle = 0.53$") to 17 (cross-cone,$\langle r \rangle = 1.33$").

With the extractions on hand, we fit the main emission lines of the sample in a quite similar fashion than made for spaxels. The difference resides in allowing the fits to have one to up three Gaussian components. To evaluate the necessity of extra components, an F-test criterion was applied as presented in appendix A.3.

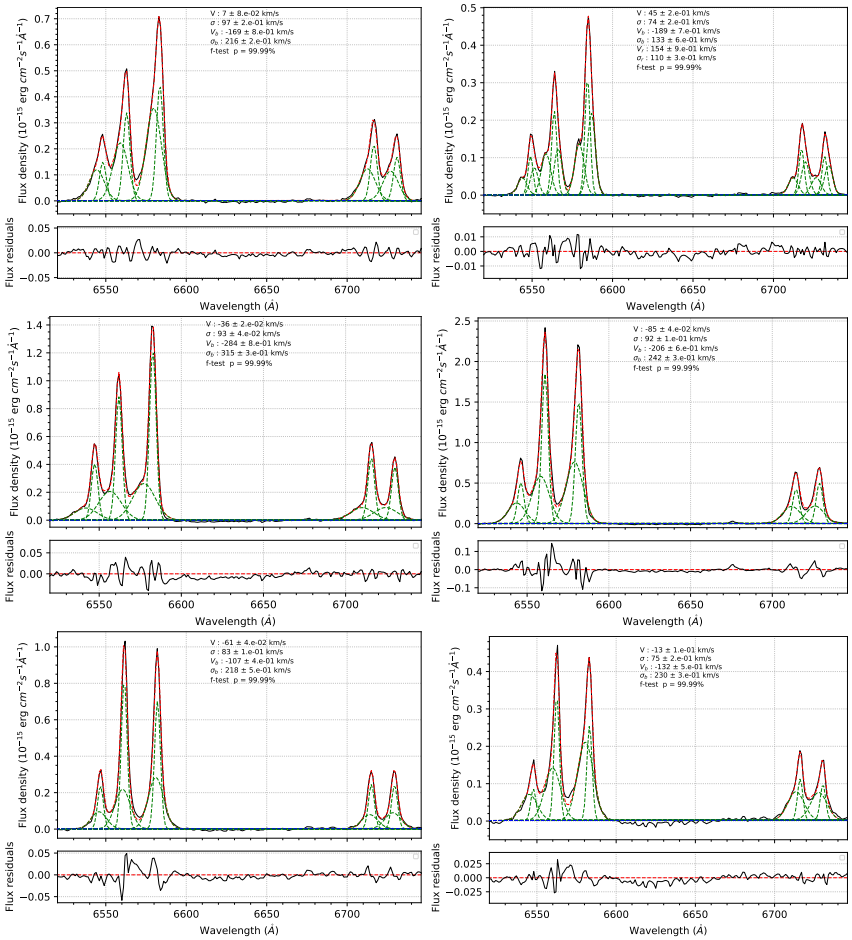

Figure 3.9: Emission line fitting for extractions towards the east (top) and west (bottom) ionization cones. From left to right, the extractions position angles are $\langle PA \rangle = 25°$, 72° and 128°. Eastern cone extractions, from left to right, have mean distances from the nucleus of $\langle d \rangle = 1.32''$, $1.67''$ and $1.32''$. In addition, towards the western cone, the mean distances from the nucleus are $\langle d \rangle = 0.53''$, $0.92''$ and $1.32''$. The fitted parameters are shown in the plots. The velocity and velocity dispersion are shown for the narrow (v, σ), broader (v_b, σ_b) and to an redshifted broader component if required (v_r, σ_r). The f-test p value of 99.99% means 1 chance in 10000 that the additional fitted component is not real.

Most optical emission lines required at least two Gaussian components, with a clear broader component shifted to higher velocities. A sample of fits towards the eastern and western cones are shown in the figure 3.9. In a statistically significant way, this result shows the necessity of a secondary Gaussian component to model the emission lines. Therefore, validating the use of more than a Gaussian component when fitting the spectra of the optical data cube.

3.4 The Narrow Line Region General View

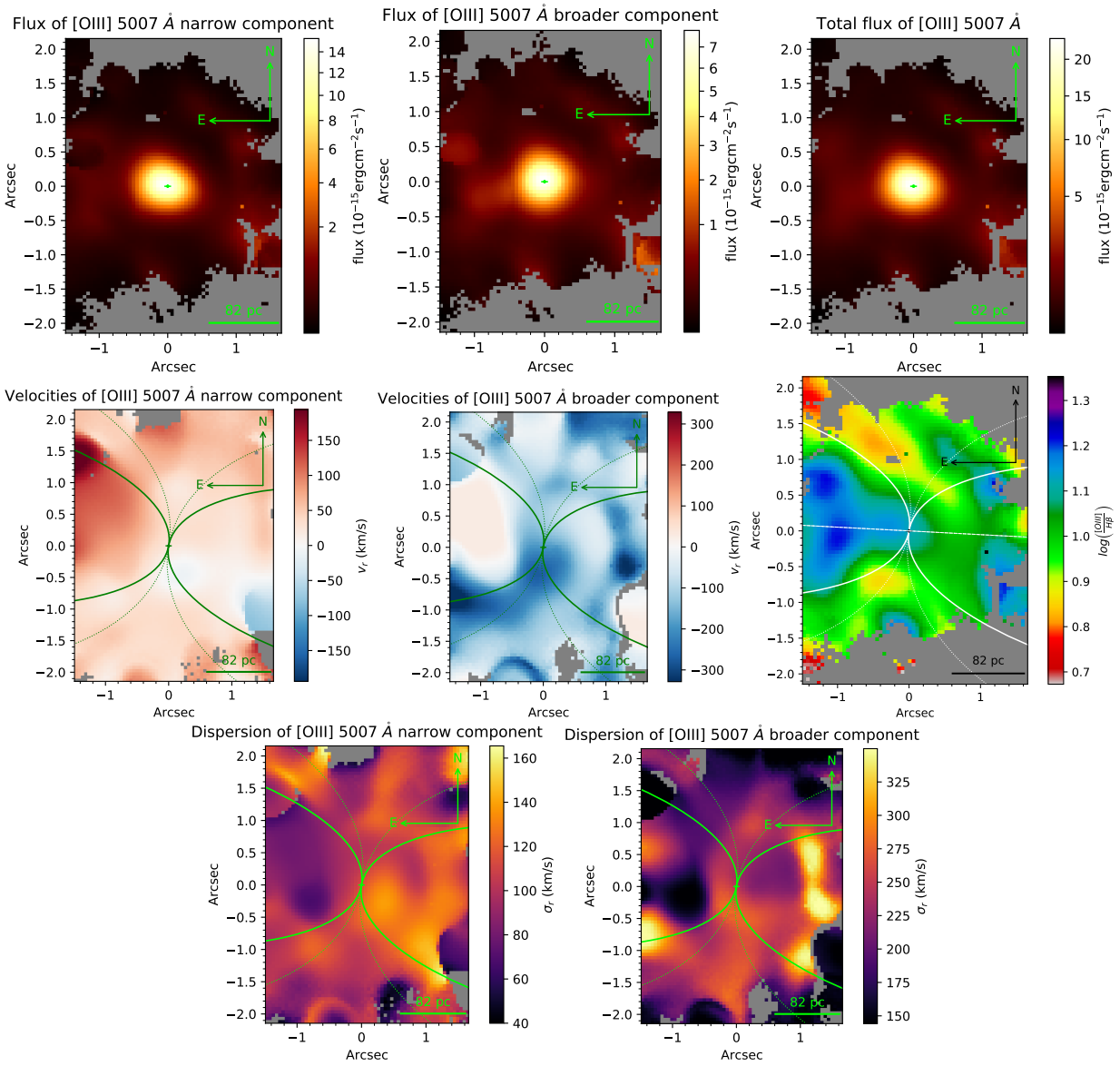

Figure 3.10: General view of the NLR of NGC 5643. (Upper panel) Narrow, broader, and total fluxes of [OIII]λ5007. (Middle panels) Narrow and broader components velocities of [OIII]λ5007. On the right is the total fluxes line ratio map of [OIII]/Hβ. (Bottom panel) Narrow and broader component dispersion maps of [OIII]/Hβ. Curves represent the ionization bicone boundaries and, the dashed ones, upper limits.

Figure 3.10 shows the general gas distribution, kinematics, and excitation properties of [OIII]λ5007. The emission is mainly distributed along an ionization bicone, confirmed by the high excitation shown in the [OIII]/Hβ map. Kinematics is a combination of rotation and outflows. The strongest outflows are seen southeast in velocity and dispersion maps of the broader component, possibly a better view of the blueshifted outflow found in Cresci et al. (2015).

In the next sections, we will further analyze these and other gas properties. We also will explore the differences found in the gas at distinct degrees of ionization and phases.

3.5 Flux Distribution of the Emission Lines

The narrow, broader component and total fluxes of [OIII]λ5007 and [NII]λ6583 are in figure 3.11. Despite their different fluxes values, the [NII]λ6583 tend to be emitted more smoothly across a wider FoV. Part of this distribution is due to a less concentrated broader component. The same behavior is seen in most emission lines, achieving wider opening angles than seen for [OIII]λ5007. They recover the arc shape morphology early seen in the blueshifted channel maps.

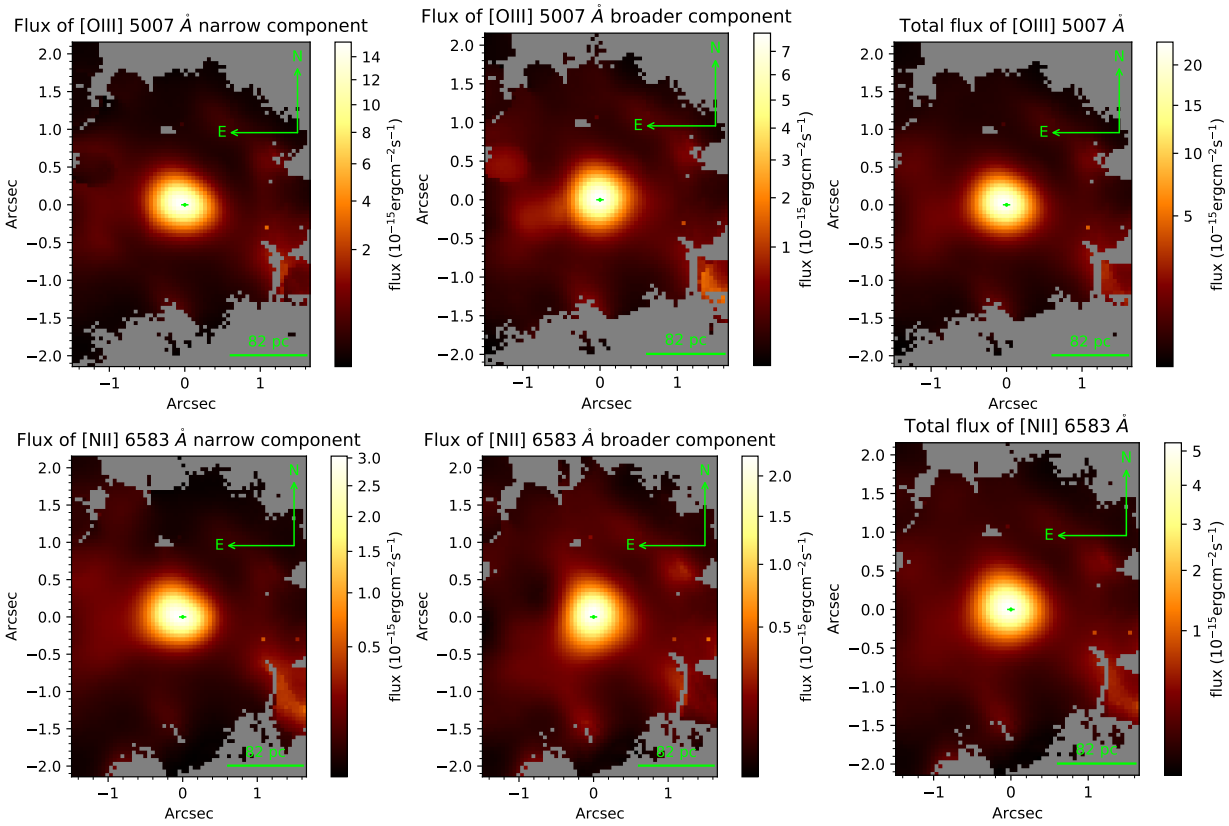

Figure 3.11: Extinction corrected integrated fluxes maps of the [OIII]λ5007 (top) and [NII]λ6583 (bottom) emission lines. The narrow component, the broader component, and the total fluxes are presented from left to right.

RB maps were built to compare the gas distribution with different ionization levels. Each layer is normalized individually. Different from channel maps that trace intensities, individual layers of the RB evince how that specific line emission is distributed across the field.

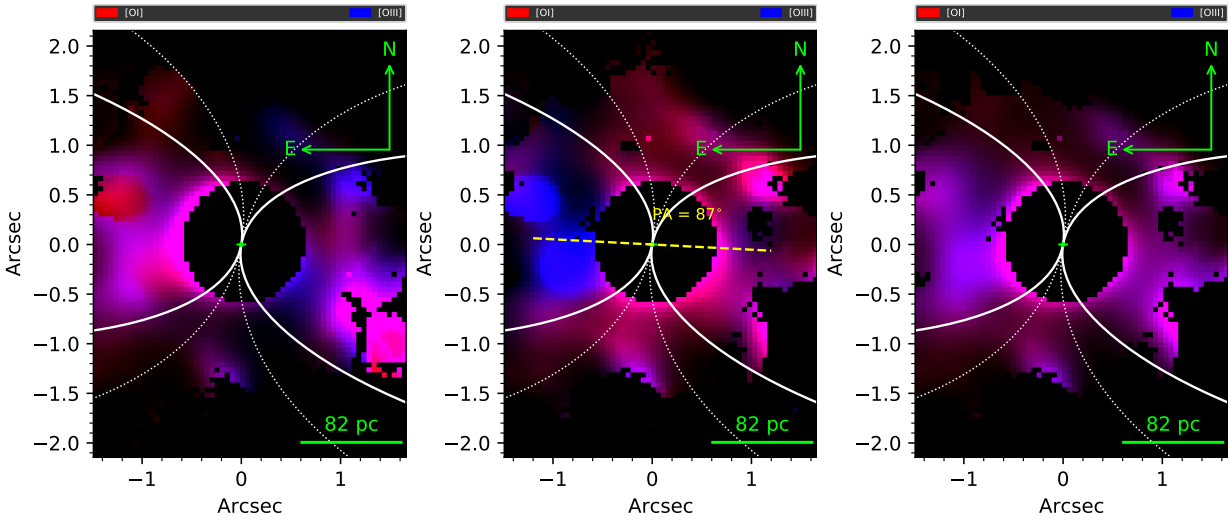

Figure 3.12: Narrow (left), broader (middle) and total fluxes (right) of the [OI]λ6300 (red) and [OIII]λ5007 (blue) emission lines. White curves represent the ionization bicone boundaries and, the dashed ones, upper limits. The yellow dashed line is the overall orientation of the radio jet PA = 87°.

The figure 3.12 illustrates the distribution of [OI]λ6300 and [OIII]λ5007 in the narrow, broad, and total emission. There is no significant distinction between the distribution of the lines when looking for the whole emission. There is an apparent deficiency of [OI]λ6300 in the west side in the narrow component, maybe suggesting a high ionization level at the west cone. However, this lack is not seen in the wing component. For this component, most of the inner east side is dominated by emission from [OIII]λ5007, while [OI]λ6300 is mainly in the outskirts. The [OI]λ6300 appear isolated far from the bicone axis on the eastern side. This drop of ionization degree in the outskirts possibly is due to an attenuation of the AGN continuum.

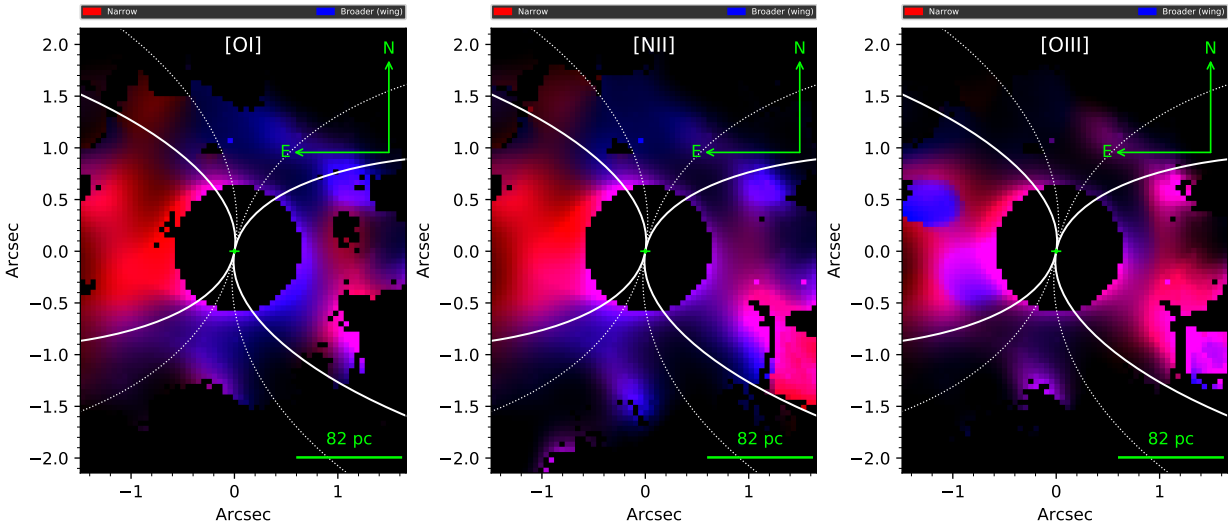

Figure 3.13: Narrow (red) and broader (blue) components images from [OI]λ6300 (left), [NII]λ6583 (middle), [OIII]λ5007 (right).

The emission coming from the narrow and broader component emission lines plays a decisive role in the ionized gas distribution. Figure 3.13 shows the distribution for both components for [OI]λ6300, [NII]λ6583, [OIII]λ5007. The wing emission, tracing gas of high velocity, in low-ionization lines is mainly emitted far away and not limited to the ionization axis. The narrow component tends to fill the cones. This behavior, also seen on channel maps on the eastern side, is shown in figure 3.13 be also true for the west cone. Different behavior was found for [OIII]λ5007 besides the more concentrated emission. The gas in high velocities is also emitted along de bicones. Knots of high emission for the broader component are evident in figures 3.12 and 3.13 on both sides. Although the emission line distribution presented little difference, the ionization degree and how the high-velocity regions are distributed account for them.

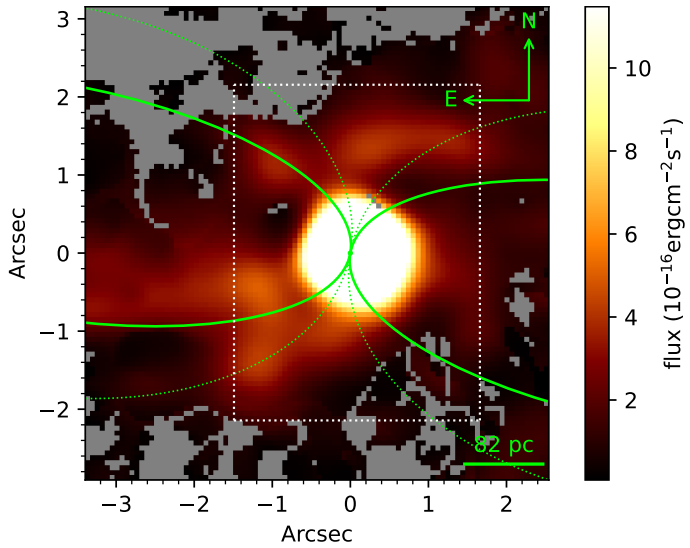

Figure 3.14: Flux map of H_2 1-0 S(1)λ21218. The ionization cone region is delimited by green curves and the GMOS FoV as the white dashed rectangle.

The H_2 1-0 S(1)λ21218 flux distribution is presented in figure 3.14. The flux shows the circumnuclear spiral shape and arms seen in figure 1.7. The flux confirms the H_2 1-0 S(1)λ21218 emission in the direction of the ionization cones. Towards the eastern side, the emission seems to be associated with the ionization bicone walls, resembling the arc shape morphology seen in the low ionization gas. This emission is bright and more extended in the direction of the brighter southeast region, where high velocity ionized gas resides. This suggests that maybe the H_2 1-0 S(1)λ21218 in the cones are associated with outflows.

3.6 Emission Line Kinematics

The Gaussian component kinematics fitted to [OIII]λ5007 and Hα is shown in the following plots. Velocity maps and profiles for both present similar behavior in figure 3.15. The ionization cone boundaries, as previously seen in figure 3.6, are shown in their velocity and dispersion kinematics. The profiles were taken at stellar disc PA = 138° and perpendicular to it at PA = 48°. The radial profile along the PA = 138° shows a rotation pattern, showing similar velocity amplitude relative to the stellar rotation disk of figure B.3.

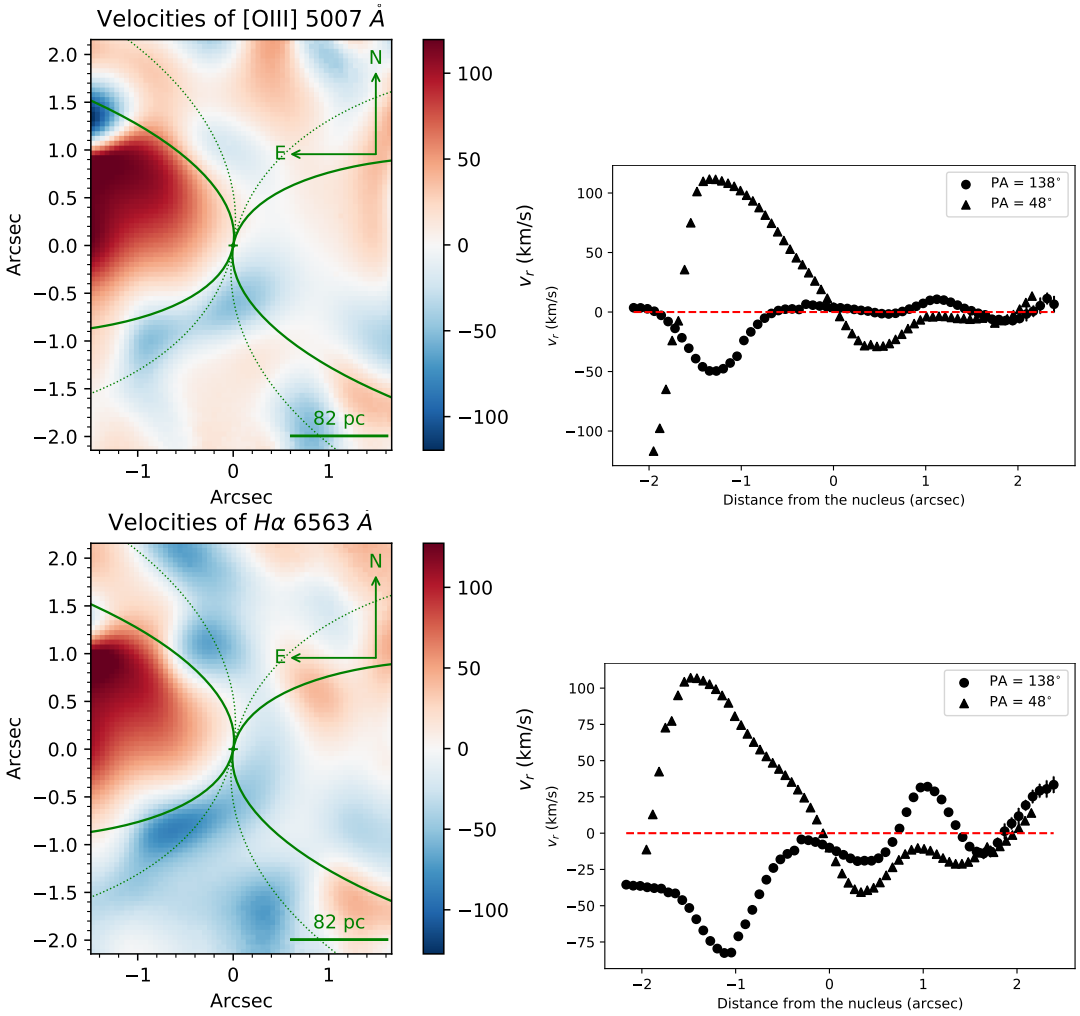

Figure 3.15: One Gaussian component velocity field for [OIII]λ5007 in the top and for $H\alpha$ in the bottom. The dashed line shows the stellar rotation axis. The curves indicate the bicone orientation and limits. To the right, the profiles are to the rotation axis (PA = 138°, circles) and perpendicular (PA = 48°, triangles).

The gas velocity dispersion maps taken from one Gaussian component are shown in figure 3.16. They present a general trend of low dispersion inside the ionization bicone. The velocity dispersion becomes higher on the outskirts, evincing the hourglass morphology. This result is probably a consequence of the lines broadening outside the internal bicone region. This is a confirmation of the findings of the ionized gas distribution. Curiously, the same dispersion enhancement far from the bicone region is seen for [OIII]λ5007. Possibly this indicates that the [OIII]λ5007 also broadens in the outskirts. However, this effect is less pronounced in the gas distribution since [OIII]λ5007 is much fainter farther away from the ionization bicone.

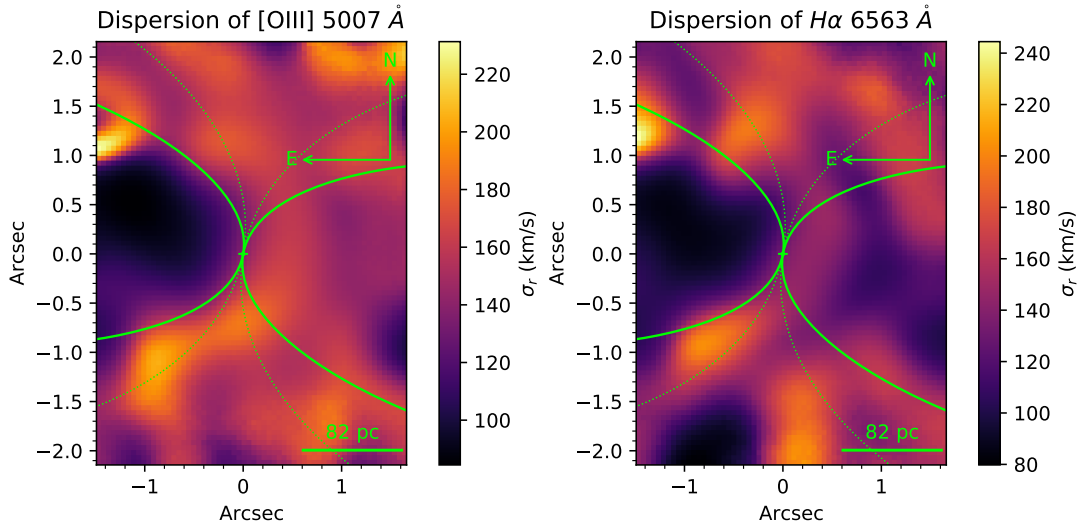

Figure 3.16: Gas velocity dispersion map taken from a decomposition using one Gaussian component of the emission lines for [OIII]λ5007 and $H\alpha$. The curves indicate the bicone orientation and limits.

A Gaussian component is not sufficient to model the profile observed for the emission lines. Because of that, in addition to the narrow component, a broader one was fitted to take into account the asymmetric wings observed in the lines. This secondary Gaussian is a few tens to hundreds of km/s broader than the first one, having no relation with the broad lines found in Type 1 sources. This asymmetric profile in the wing is usually interpreted as a doppler shift due to outflowing motions, as explained in section 1.1.2. The following results aim to separate the regular rotation from the supposed outflowing motions.

Figure 3.17 shows the narrow Gaussian component velocities map and profiles for the [OIII]λ5007 and Hα. This last one was fitted together with the low-ionization lines as described in section 2.2.2. Even when we try to fit more than one Gaussian component, the map differs from the stellar velocity disc seen in figure B.3. The main difference arises in the direction of the ionization bicones. There is an excess of redshifted velocities towards the east and blueshifted to the west. The profile at PA = 48° also suggests an acceleration of the gas far from the nucleus, most prominent on the east side. Deviations from the disk rotation in the direction of the cones can be tracing low-velocity biconical outflows. Superposed to that, we cannot rule out that a more complex disc configuration can be present. In the Hα the bulk of gas is between -317 km/s $\leq v \pm 2\sigma \leq$ 496 km/s and FWHM $\leq$ 476 km/s. Similar values were found for the [OIII]λ5007 with velocities in the range -326 km/s $\leq v \pm 2\sigma \leq$ 402 km/s and FWHM $\leq$ 390 km/s.

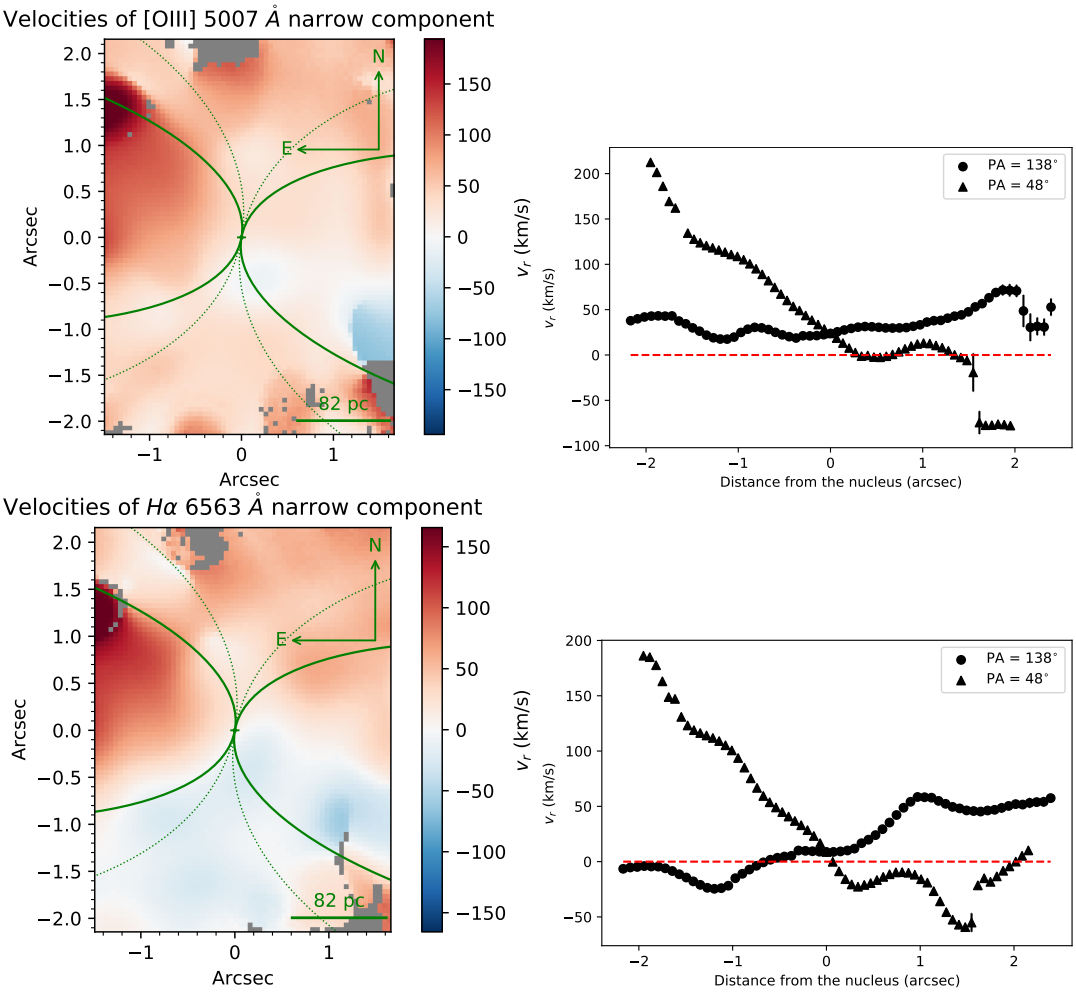

Figure 3.17: Velocity maps of the narrow component of [OIII]λ5007 and $H\alpha$. The curves indicate the ionization bicone limits. On the right, the radial profiles to the rotation disk ($PA = 138°$) and in the perpendicular direction ($PA = 48°$).

An unexpected result arises when the fit for the molecular H_2 and the narrow component of Hα kinematics are compared. Figure 3.18 shows the velocity and velocity dispersion maps of both phases. In the same FoV, despite the better spatial resolution in the K-band, both lines present matched kinematical structures. A similar deviation from the disk rotation was found in the bicone direction for the H_2 molecular lines. Hα and [OIII]λ5007 low-velocity outflows present similar widths to the FWHM $\approx$ 530 km/s of H_2. This result suggests that the low-velocity outflow is affecting both phases. Yet, [OIII]λ5007 dispersion does not present matched structures with H_2, as seen for Hα. The tentative connection between H_2 and Hα implies that they are tracing similar physical mechanisms. Without further analysis, this can suggest that both emissions are co-spatial.

Hot molecular gas is far beyond the GMOS FoV in figure 3.18. The vast majority

of the high-velocity dispersion regions are within the bicone. The high molecular dispersion regions are in agreement with the previously found in Davies et al. (2014) and shown in figure 1.7. The authors interpret the dispersion enhancement in both sides as molecular outflows, probably at the disc plane. The bulk of H_2 is in the velocity range -661 km/s $\leq v \pm 2\sigma \leq$ 597 km/s and FWHM $\leq$ 542 km/s. In addition to the apparent coupling with the Hα kinematics, the current results suggest that the molecular gas presents non-rotation motions inside the cones.

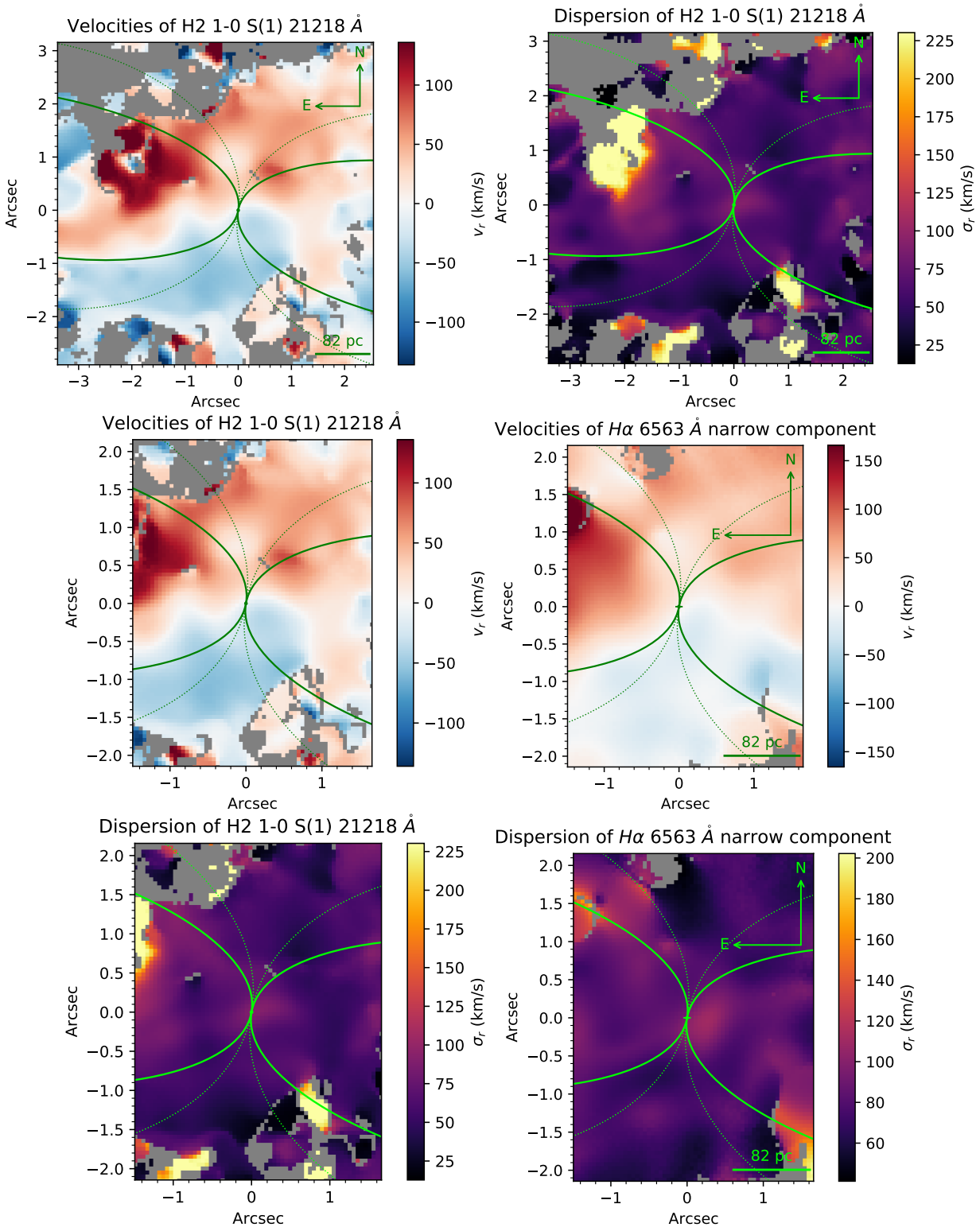

Figure 3.18: Top: Velocity and dispersion maps of the K-band $H_2\lambda21218$ molecular gas with the ionization bicone boundaries indicated by the curves. Middle: Velocity maps of $H_2\lambda21218$ molecular gas in the GMOS FoV and for the narrow component of $H\alpha$. Bottom: Velocity dispersion maps of $H_2\lambda21218$ molecular gas in the GMOS FoV and for the narrow component of $H\alpha$.

The asymmetric wing velocity maps of [OIII]λ5007 and Hα are presented in figure

3.19. The gas has blueshifted velocities in a great part of the FoV. The redshifted velocities are found on the inner east cone and towards the west cone walls, seen in Hα. Hα line emission traces the bicone walls in blueshift on the eastern side and redshift on the west side. On the other hand, [OIII]λ5007 presents a different scenario. Although the line shows a similar behavior as Hα towards the east, the west side apparently traces different patterns in their kinematics. Yet, [OIII]λ5007 and Hα also presented blueshifted emission in the west side, like proposed by the ionization cones model of Fischer et al. (2013).

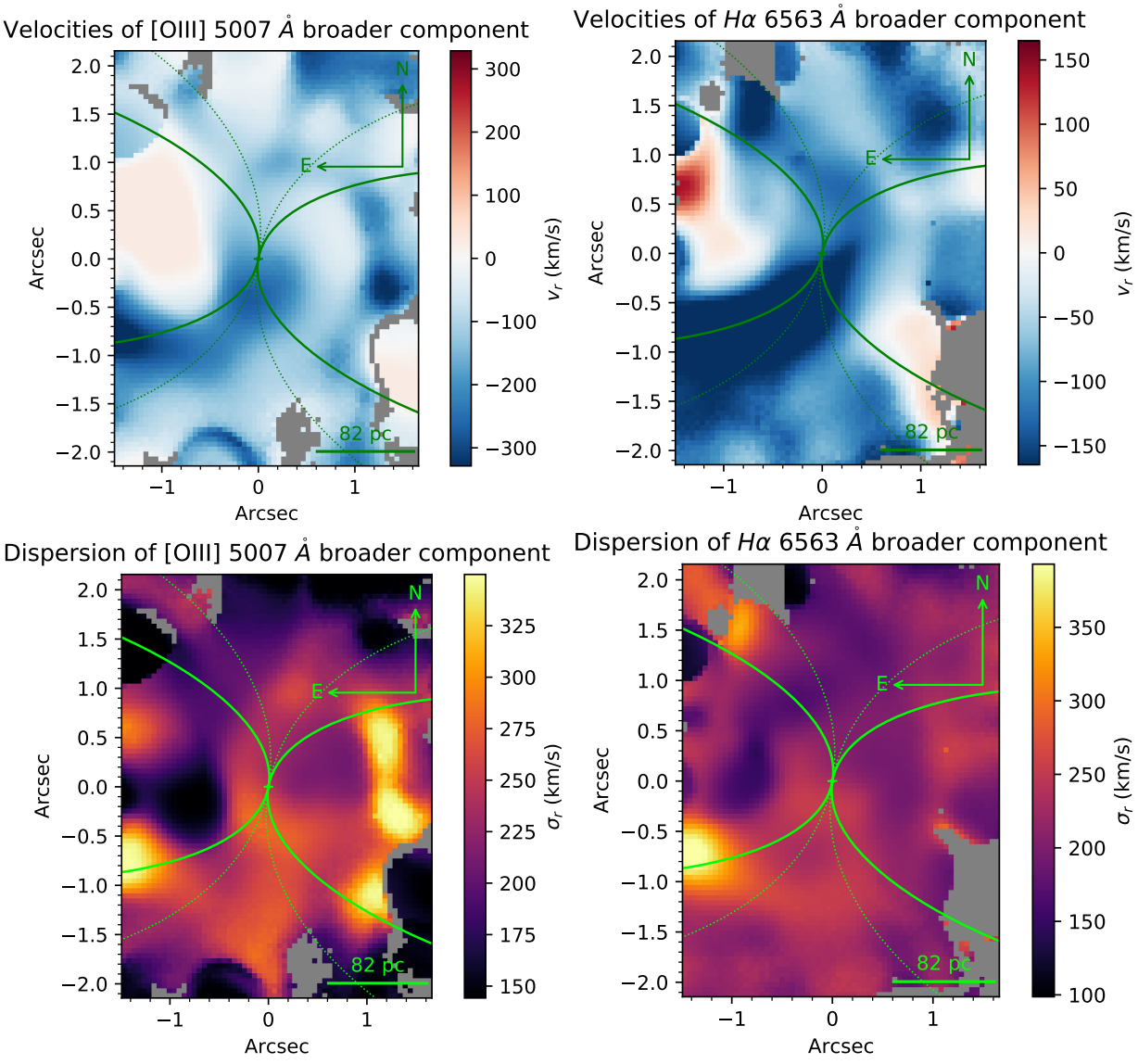

Figure 3.19: Velocity and dispersion maps of the broader component of [OIII]λ5007 (left) and *H*α (right). Curves indicate the ionization cones edges.

The velocity dispersion maps for the broader component are shown at the bottom plots of figure 3.19. Hα and [OIII]λ5007 show the highest dispersion values towards the

eastern cone boundaries, possibly tracing the blueshifted outflow indicated in the velocity maps. In contrast to Hα, [OIII]λ5007 also presented the highest dispersion values inside the west cone. Furthermore, [OIII]λ5007 shows a high dispersion region inside the east cone. This last region is co-spatial with a bright emission knot and is apparently associated with a high excitation region found in [OIII]λ5007/Hβ.

Hα and [OIII]λ5007 also showed increased dispersion in the cross-cone directions, most evinced towards the south. Part of this can be attributed to outflows not limited to the cones. Conversely, some of these regions shown in the [OIII]λ5007 map have low peak velocities. In that case, part of the gas can be tracing the turbulence in the disk caused by jet-ISM interactions rather than outflows (Venturi et al., 2021).

The broader component shows much higher velocities than those seen in the narrow one. Hα presented velocities in the interval between -950 km/s $\leq v \pm 2\sigma \leq$ 621 km/s with FWHM $\leq$ 926 km/s. For the [OIII]λ5007 the data reveal velocities of -1028 km/s $\leq v \pm 2\sigma \leq$ 665 km/s with FWHM $\leq$ 824 km/s. The highest velocities in blueshift are achieved in the arc boundaries of the eastern cone, mainly towards the southeast. Moreover, [OIII]λ5007 also shows similar outflow in the inner west cone.

3.7 Ionized Gas Extinction

To obtain the extinction values, as described in section 2.2.3, the total flux of Hα (narrow+broader) and the single Gaussian fits of Hβ were used. The extinction is not different using the total flux of Hβ, however, with the single Gaussian fits we can cover a large FoV, where Hβ is too faint to get good fits of the broader component.

The ionized gas extinction, obtained from the Balmer decrement method, shown in figure 3.20 is in the range 0.06 mag $\leq$ Av $\leq$ 4.40 mag. The dust structure and values are compatible to found in Cresci et al. (2015). The distribution of dust is non-homogeneous, affecting much more the north, south, and west side than the eastern. In practice, 4.4 magnitudes mean that the intrinsic flux for [OIII]λ5007 and Hα are 94 and 28 times the observed ones, respectively. Therefore, dust is likely responsible for some works that do not detect the western emission (Simpson et al., 1997).

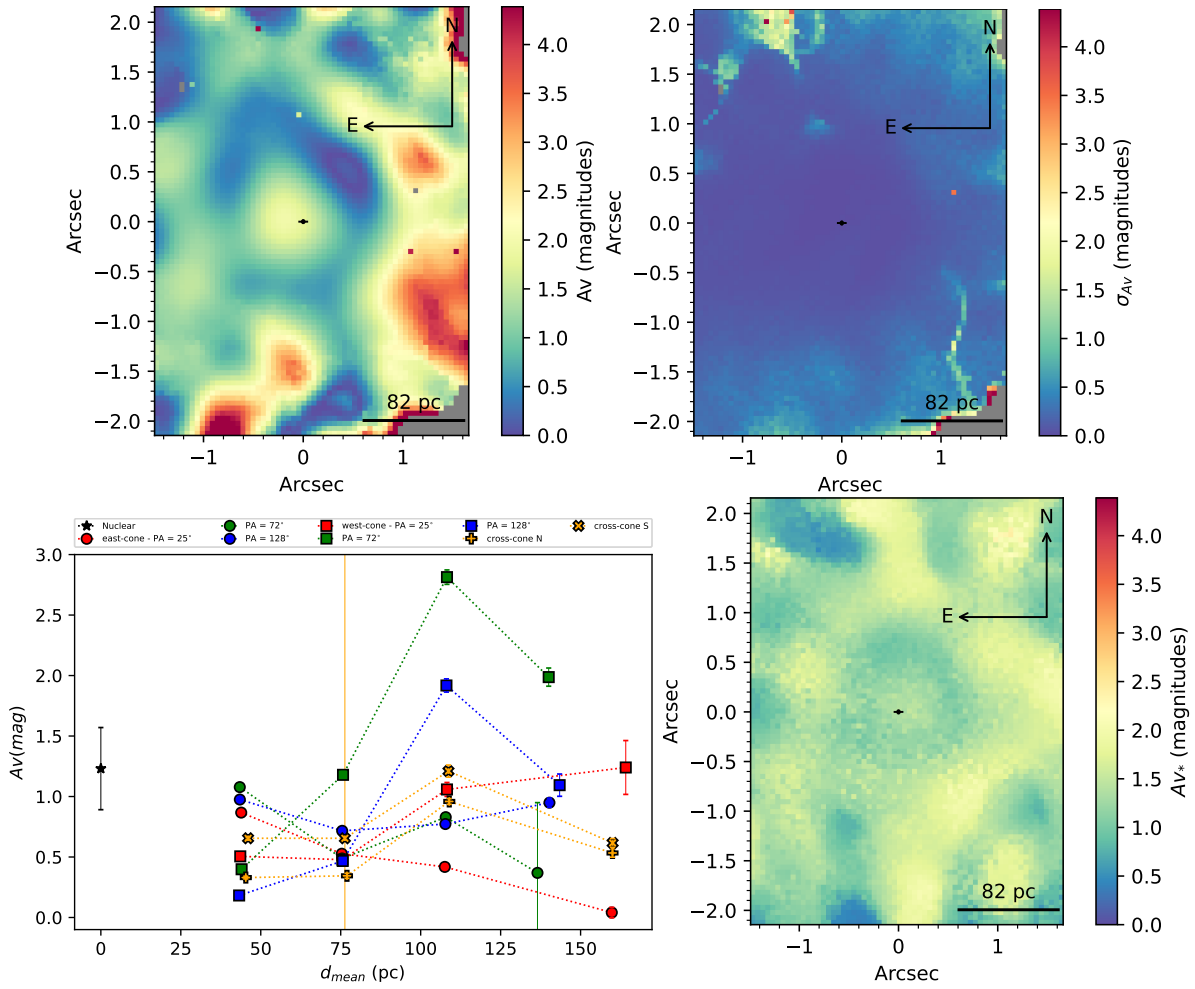

Figure 3.20: (Top) The ionized gas extinction map and its errors are derived from the Balmer decrement method. (Bottom) On the right is the Av radial profiles obtained from the extractions. The star indicates the nuclear spectrum, circles and boxes the eastern and western cones, and pluses and crosses the cross-cone north and south. The red, green and blue symbols represent extractions done at $\langle PA \rangle = 25°, 72°$ and 128°. The stellar extinction obtained with `STARLIGHT` code is at the bottom left corner.

Extinction profiles of the extracted spectra are shown in the bottom left corner of figure 3.20. Symbols and colors identify the region where each extraction was made based on the scheme of figure 3.8. As seen in the A_v maps, the extinction increases to the west side, having a peak at $A_v(\langle r \rangle = 1.32") = 2.81 \pm 0.06$ magnitudes. At this radius, approximately 104 pc far from the nucleus, most of the profiles showed their peak of extinction. By contrast, the eastern cone profile at $\langle PA \rangle = 25°$ seems to have a radial decrease of reddening. The values obtained with the extractions are lower than for spaxels because there are few spaxels with very high values, being diluted in the integrated spectra.

The dust affecting the stellar part in figure 3.20 clearly shows a disturbed ring structure. A ring of molecular gas was predicted to be fed by the circumnuclear spiral in

the model of Davies et al. (2014). The association between dust and molecular gas was previously shown in the circumnuclear spiral of figure 1.9 from the work of Alonso-Herrero et al. (2018). The dust ring found is possibly associated with this molecular gas ring.

A key result comes from comparing the gas and stellar extinction. The extinction from the stars presents similar dust structures when compared with the gas, but lower values, in the range 0.6 mag $\leq$ Av $\leq$ 2.0 mag. The lower values are expected, with usually the stellar reddening being half of the obtained from the gas, at least in starburst galaxies (Calzetti et al., 1994). The stars are not always coupled with the dust, diluting the extinction. The surprise happens at the northeast ionization cone region, where the stellar extinction becomes higher than the measured for the gas. This implies that the ionized gas is in front of the dust that obscures the stars in the background. The inclination may help since the northeast side is the far one. However, it can also suggest that the gas can be out of the plane of the galaxy, tilted relative to the disc, as indicated by the ionization bicone model (Fischer et al., 2013).

3.8 Electron Density and Temperature

Pairs of forbidden emission lines with distinct critical densities can be used for electron density diagnostics. Steiner et al. (2009) proposed to apply a linear transform in the flux maps of these lines to obtain low and high-density maps. For the [SII]$\lambda\lambda$6716,6731 doublet the low density map correspond to $n_e \leq 81\ cm^{-3}$ and the high to $n_e \geq 5.9 \times 10^3 cm^{-3}$. Spaxels in both maps probably have intermediate electron densities.

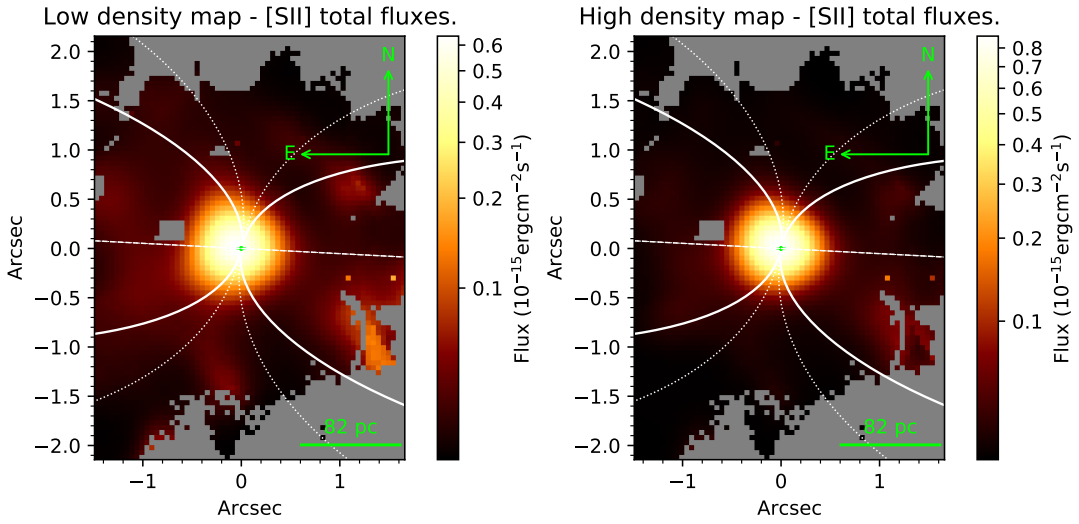

Figure 3.21: Low and high-density maps obtained from the total flux of [SII]λ6716,6731 applying the linear transform of Steiner et al. (2009). The full and dotted curves represent the ionization bicone fit and an upper limit. The white dashed indicate the jet PA = 87°.

The maps of low and high densities are shown in figure 3.21. The high densities are concentrated closer to the nuclear region. On the other hand, the low electron densities are less concentrated, filling the ionization cones up to their edges.

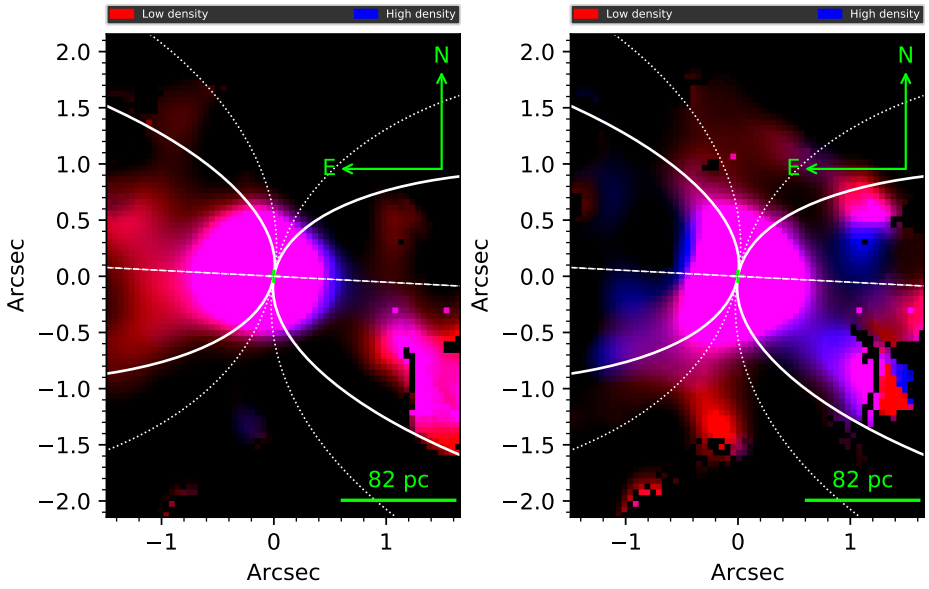

Figure 3.22: Electron density diagnostics for the narrow and wing components of [SII]λ6716,6731. The full and dotted curves represent the ionization bicone fit and a higher limit. The white dashed indicate the jet PA = 87°.

The same kind of diagnostic was tested using the narrow and broader components of the [SII]$\lambda\lambda$6716,6731 doublet, shown in figure 3.22. In the cross-cone region, the gas has lower electron densities. The high velocities gas is more associated with high-density

regions inside the bicone limits. This fact is even more apparent in the west cone region.

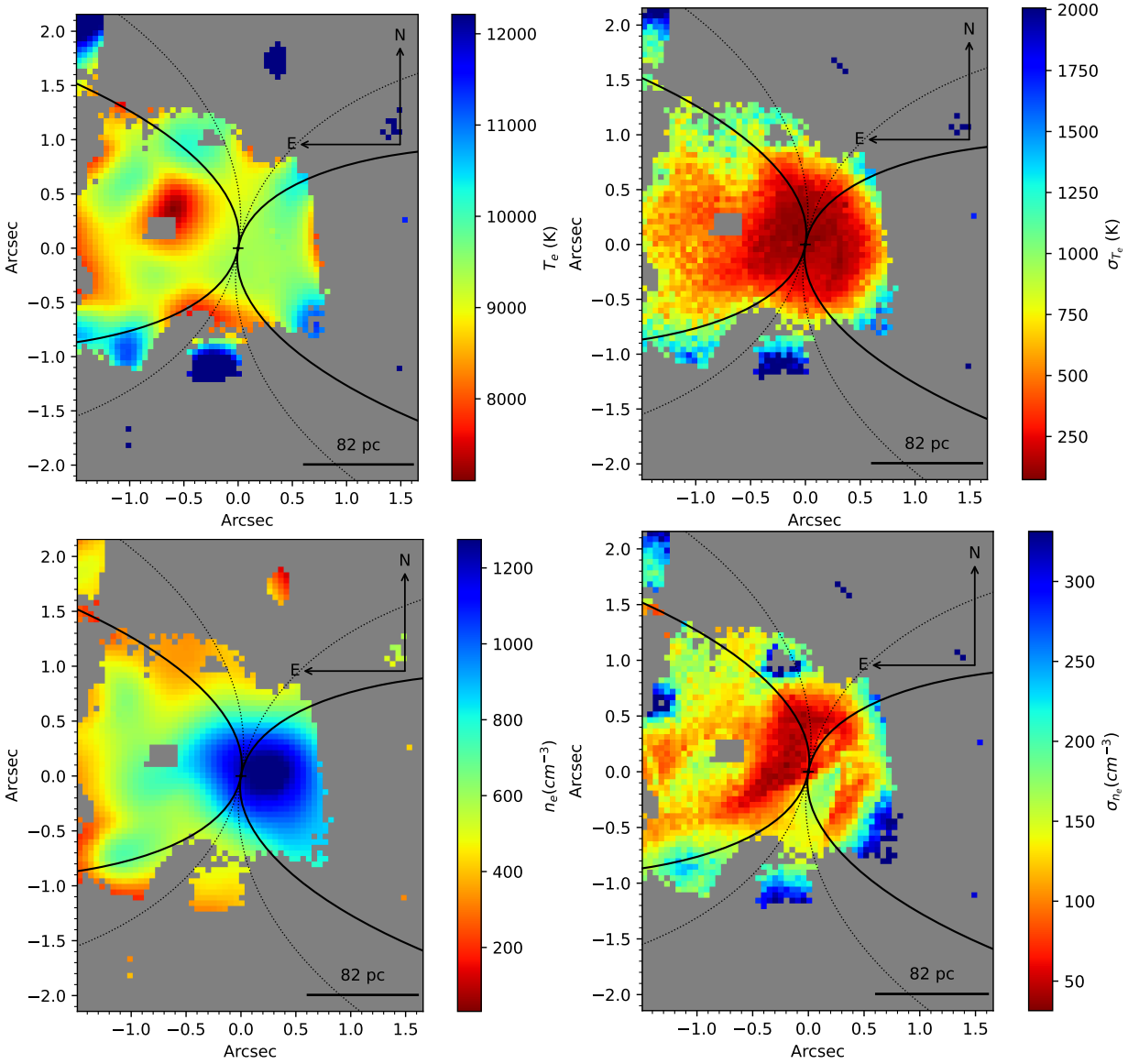

Figure 3.23: Electron temperature T_e, density n_e and their uncertainties σ_{T_e} and σ_{n_e} maps obtained iteratively with the python routine `Pyneb`. Curves represent the ionization bicone boundaries.

Quantitative measures as well can be obtained from the emission lines. Using the code `Pyneb` (Luridiana et al., 2015), that compare the line ratios with theoretical solutions, was obtained T_e and n_e iteratively from [NII]$\lambda\lambda$5755,6548,6583 and [SII]$\lambda\lambda$6716,6731, respectively. Because the limited field presenting the weak [NII]λ5755 emission, we cannot have T_e in all FoV. The results are shown in figure 3.23. The T_e map reveals typical temperatures of 10^4 K. Inside the east cone there is an apparent drop of T_e to temperatures about 8000 K. In the direction of the cone boundaries were detected the higher temperatures, although the errors make their values compatible with the nuclear region. The

temperatures are lower than 20000 K, which are suggestive of photoionization (Mazzalay et al., 2010). The densities in the east side drop from $\approx$ 1200 cm^{-3} in the nucleus to less than $<$ 300 cm^{-3} in the outskirts. Conversely, the west side had much higher densities, peak at 0.2″ from the nucleus with $>$ 1300 cm^{-3}. The density drops more slowly towards the west. This is also evinced when assuming a constant temperature of 10000 K presented in figure 3.24.

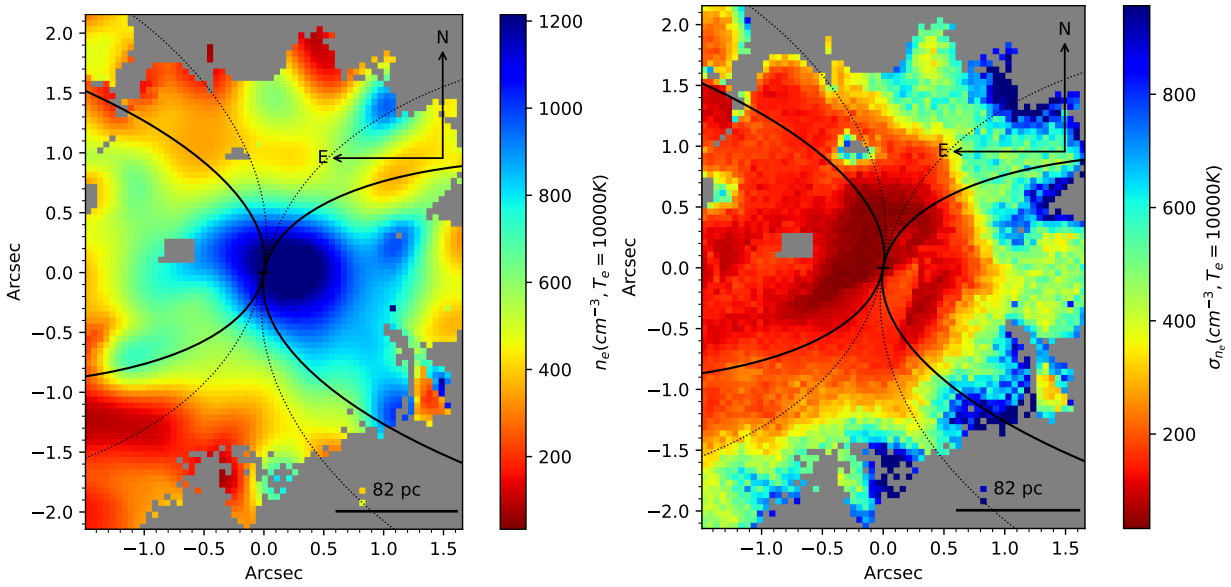

Figure 3.24: Electron density n_e and their uncertainty σ_{n_e} obtained with the python routine `Pyneb` assuming the fixed electron temperature T_e = 10000 K. Curves indicate the ionization bicone region.

3.9 Optical Excitation Diagnostics

3.9.1 Excitation Maps

The excitation maps of figure 3.25 show the line ratios of [OIII]λ5007/[OI]λ6300 and [OIII]λ5007/Hβ. These maps clearly show that the west emitting region is, in fact, the ionization cone in that direction. Higher ratios are seen mainly inside the limits of ionization bicone walls derived from [Fe II]16440λ in figure 3.7. The highest excitation ones are closer to the ionization axis. Towards the east, the high excitation is apparently co-spatial with the bright knots in the high-velocity gas, shown in the [OIII]λ5007 broader component in figure 3.11.

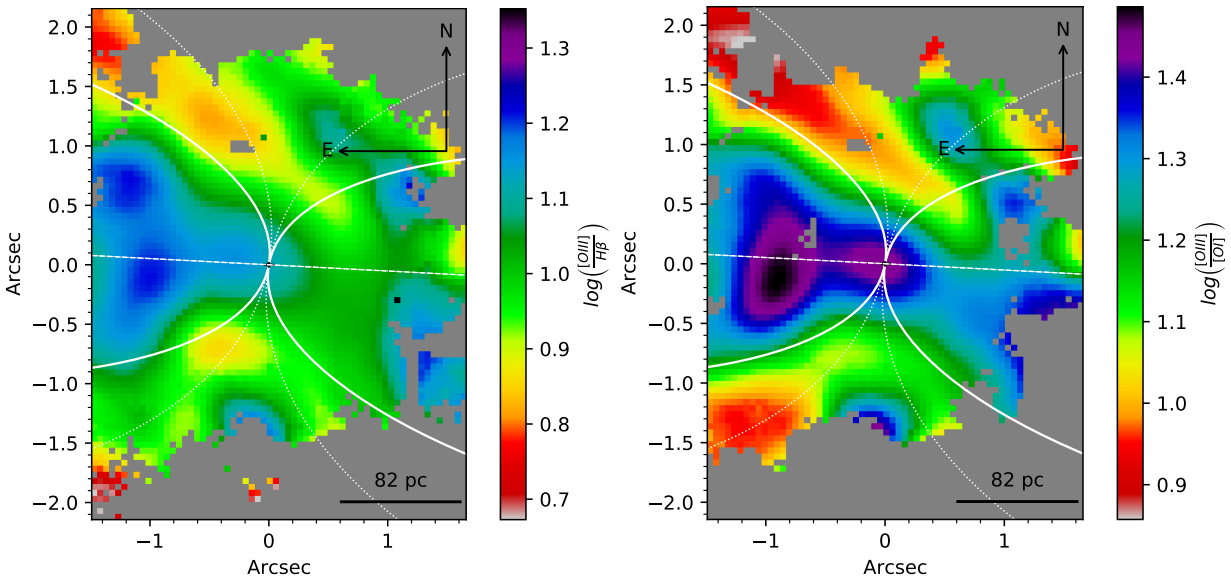

Figure 3.25: Total flux line ratios for [OIII]λ5007/[OI]λ6300 and [OIII]λ5007/Hβ. The high excitation ionization bicone is seen in both maps. Curves indicate the boundaries of the cone and the dashed line the jet PA = 87°.

Maps of low-ionization line ratios are shown in figure 3.26 for [NII]λ6583/Hα and [SII]λ6716,6731. They tend to be weaker within the cones, where there is higher excitation. In the outskirts, especially in the east, lines exhibit higher ratios, for instance, log([NII]λ6583/Hα) $\geq$ 0.25 and log([SII]λ6716,6731/Hα) $\geq$ 0.1. These regions were previously shown to be dominated by the emission of low-ionization lines, possibly receiving an attenuated AGN radiation field. The highest ratios can be also associated with shocks. Mingozzi et al. (2019) found for their sample low-ionization line ratios higher than zero associated with the edges of ionization cones and well explained by shock ionization.

Another result is an excess of $H\alpha$ and [OIII]λ5007 relative to the low-ionization lines observed across the cross-cone region. As seen in figures 3.25 and 3.26 the enhanced regions present similar ratios than in the direction of the cones. They seem to be associated with the west cone, where a peak of Hα is often seen with the jet orientation.

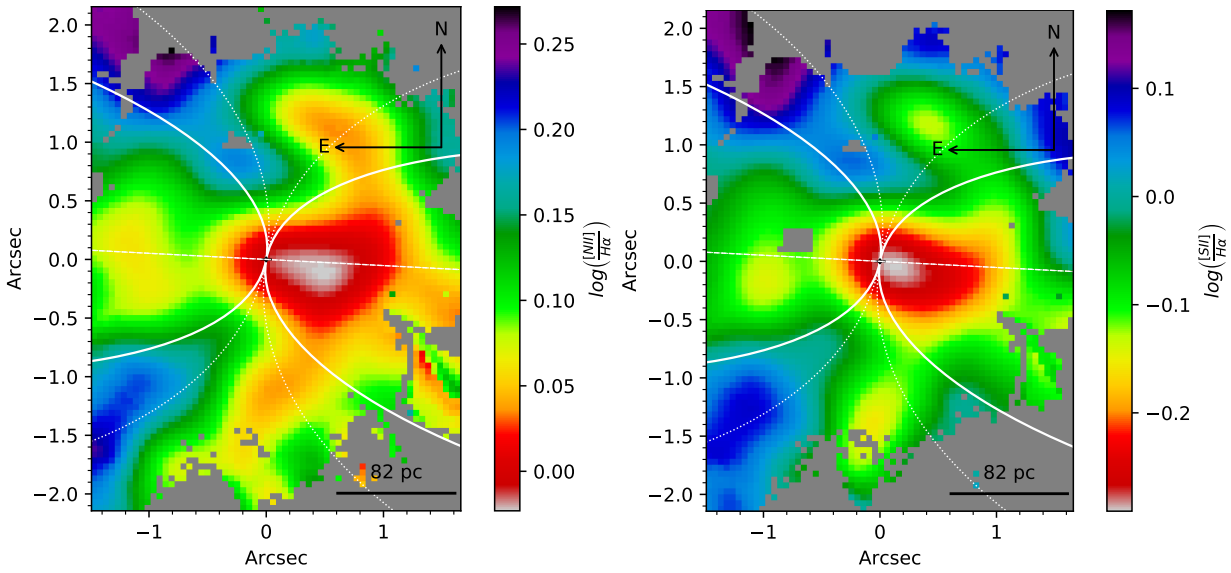

Figure 3.26: Total flux line ratios for [NII]λ6583/Hα and [SII]λ6716,6731/Hα. Curves indicate the boundaries of the cone and the dashed line the jet PA = 87°.

The enhancement of [OIII]λ5007 and Hα is also present when line ratios are analyzed for gas with different velocities. Usually, the low-velocity showed in the narrow component in figure 3.27 trace high excitation towards the west side and perpendicular to the cones. In contrast, the high-velocity gas, seen in the broader component, is often associated with high excitation in the eastern cone.

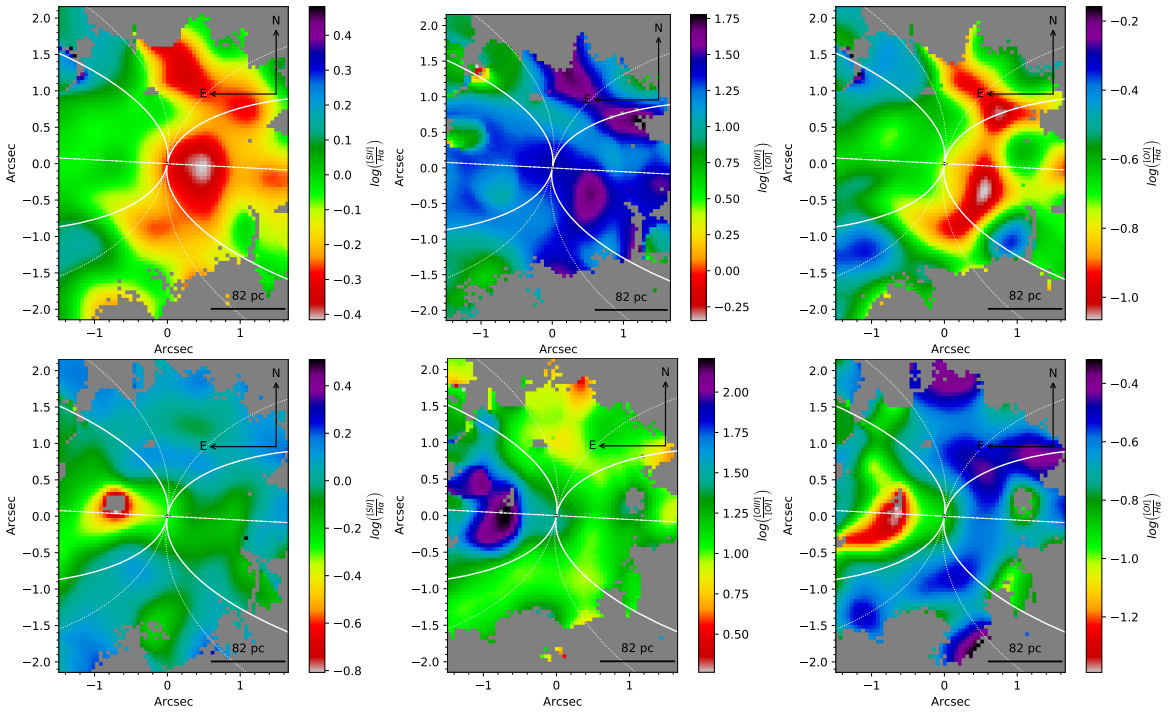

Figure 3.27: Maps of the emission-line ratios for $[SII]\lambda6716,6731/H\alpha$, [OIII]$\lambda$5007/[OI]$\lambda$6300 and $[OI]\lambda6300/H\alpha$ of gas with lower velocities (top) and higher velocities (bottom). Curves indicate the boundaries of the cone and the dashed line the jet PA = 87°.

3.9.2 Diagnostic Diagrams

Diagnostic diagrams are good tools to separate the main ionization mechanisms behind the production of the observed emission. The total flux S-BPT diagnostic diagrams are presented in figure 3.28 with the color bars indicating the Hα velocity dispersion, [OIII]λ5007/Hβ and electron density.

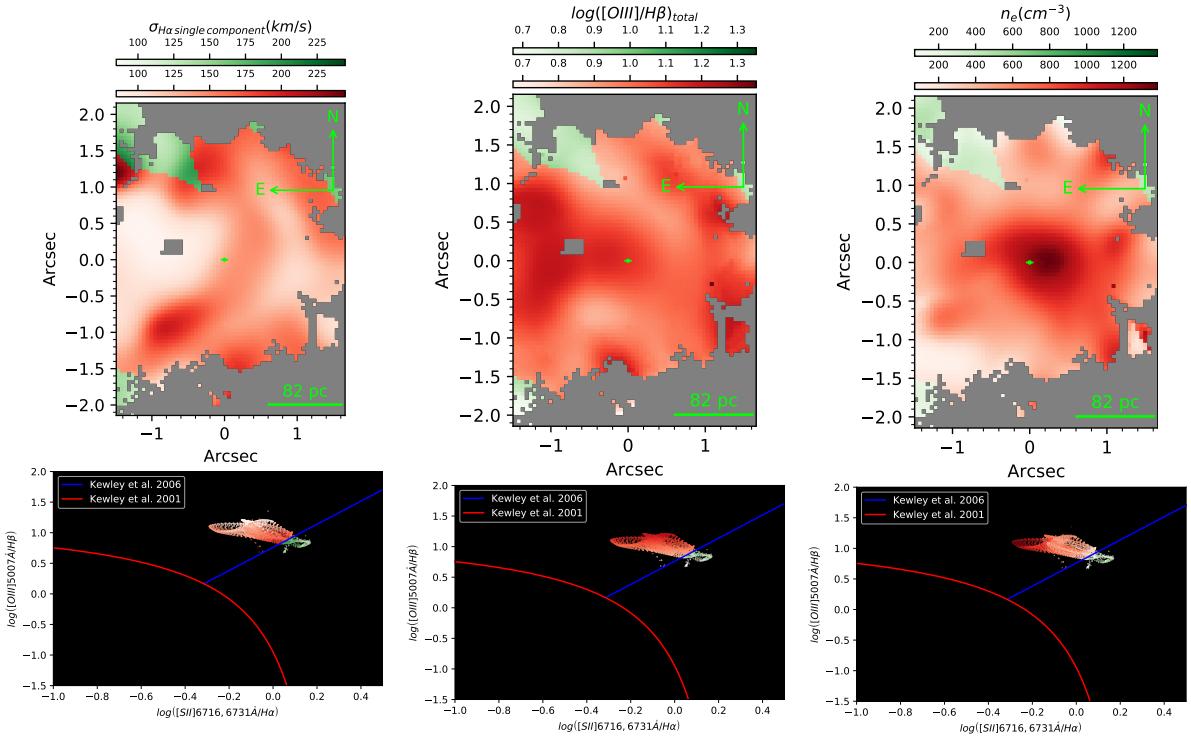

Figure 3.28: Spatially resolved S-BPT for the total flux ratios. The Seyfert-like spaxels are indicated in red and LINER-like in green. The color gradient to both activities indicates, from left to right, the Hα velocity dispersion, [OIII]λ5007/Hβ and electron density, respectively. The dispersion ranges are shown in the upper color bars.

The total flux diagnostic diagrams show the AGN as the primary ionization source across the FoV. The only diagram presenting extra information is the S-BPT. The northeast, southeast, and northwest regions present emission-line ratios compatible with LINERs. As seen in figure 3.28, the total flux S-BPT presents the lowest values of $[SII]\lambda\lambda 6716, 6731/H\alpha$ and dispersion in the bicone axis. Also, they have been associated with the highest [OIII]λ5007/Hβ and electron densities. The opposite occurs in the outskirts, where the ionization degree and electron densities drop while the dispersion increases.

The low and high velocities gas components in the S-BPT relative to the Hα dispersion are presented in figure 3.29. Both show the highest $[SII]\lambda\lambda 6716, 6731/H\alpha$ values associated with the largest dispersion values. There is another result suggestive of shock ionization contribution towards the eastern cone edges as seen in Mingozzi et al. (2019).

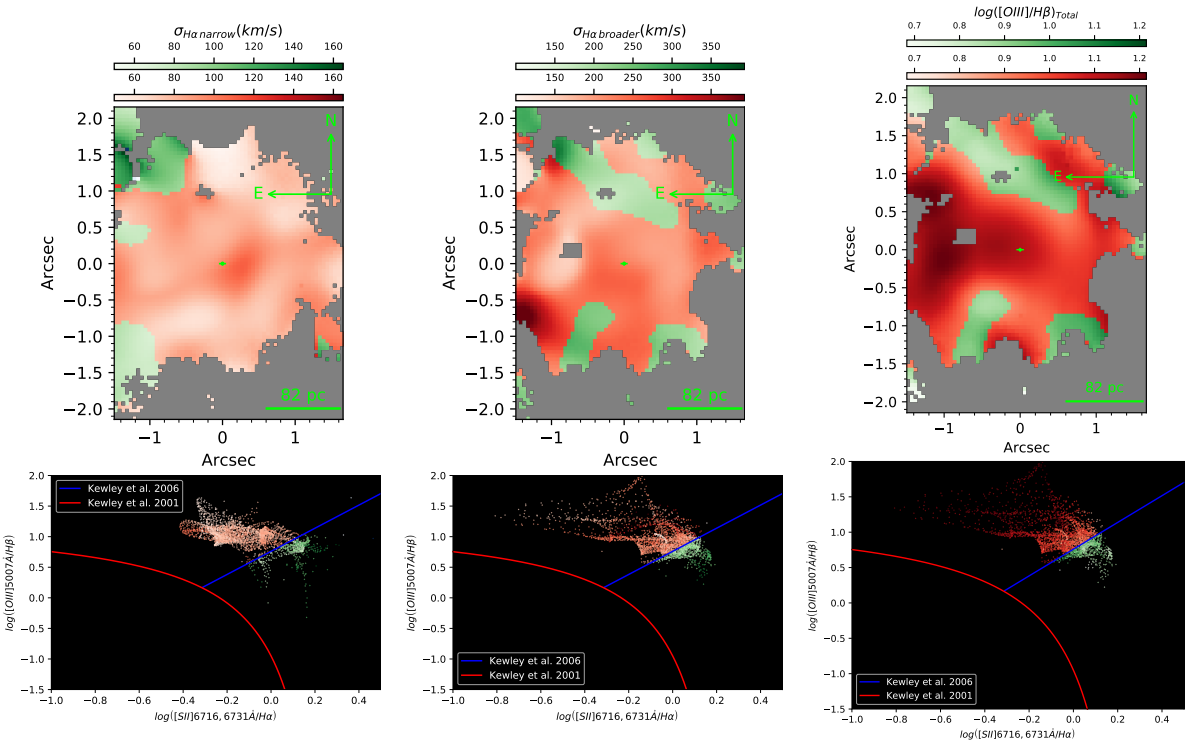

Figure 3.29: Spatially resolved S-BPT for the narrow (left) and broader (center and right panels) components. The Seyfert-like spaxels are indicated in red and LINER-like in green. The color gradient to both activities indicates, from left to right, the narrow and broader Hα velocity dispersion and the total [OIII]λ5007/Hβ. The color gradient ranges are shown in the upper color bars.

The broader component presents a wider range in line ratios, in comparison to the narrow, between -0.8 $<$ log($[SII]\lambda\lambda6716,6731/H\alpha$) $<$ 0.2. The lowest values were associated with the high excitation bicone. At the same time, they increase in the outskirts. The drop of the ionization degree is even more pronounced in the right diagram of figure 3.29. In the broader component, the LINER-like spaxels shown in green avoid the regions of higher total [OIII]λ5007/Hβ. This fact suggests that, besides the shock ionization contribution in the eastern cone edges, there is a drop of ionization in the outskirts, producing a partially ionized zone.

3.10 The Coronal Emission Lines

Coronal emission lines probe the most highly ionized gas in the narrow-line region, bringing information of regions closer to the AGN or also tracing, in an indirect way, the presence of shock ionization. In the optical spectra of NGC 5643, the emission lines of [Fe VII]λ5158,5721,6086 (Van Hoof, 2018) of IP $\approx$ 125 eV (Kramida et al., 2020) were clearly

detected. The [Fe X]λ6374 was identified but was too weak to be reliably measured. In the NIR, the emission line of [Ca VIII]λ23210 of IP $\approx$ 147 eV was observed in the K-band.

The [Ca VIII]λ23210 image is shown in figure 3.30 and the fitted emission-line parameters are presented on table 3.1. The blue circle indicates the nuclear extraction of 0.46″ diameter. Such emission seems to be extended and elongated in the direction of the ionization cones. No more extractions were done since CO absorption bands contamination is present even after the stellar subtraction. The estimated parameters were fitted with two Gaussian components, with a broader blueshifted one. Their flux is 45% of the Brγ and luminosity in the order of 10^{39} erg/s, making this coronal line brighter than [Fe VII]λ6086.

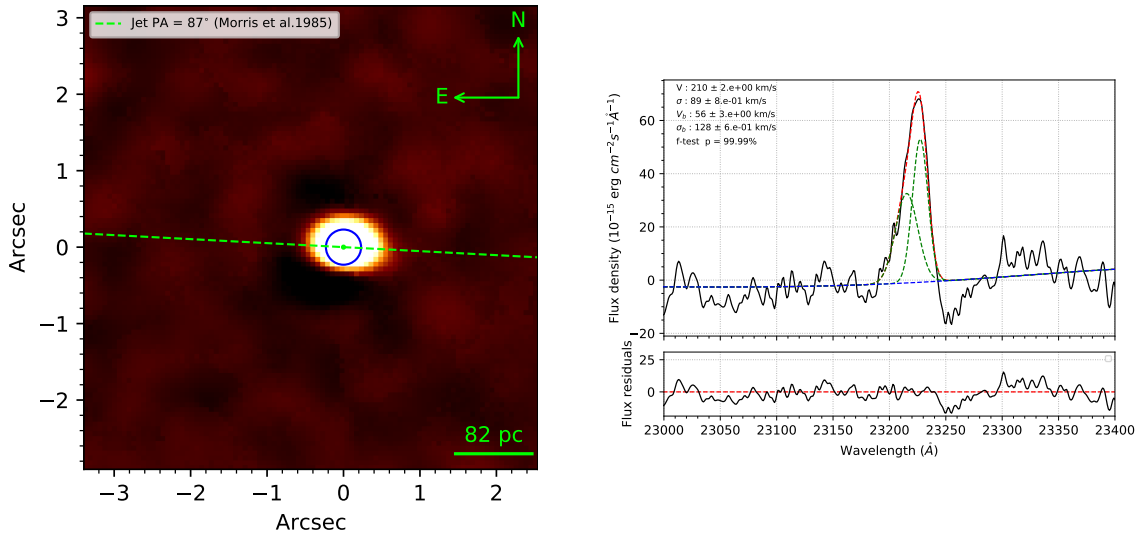

Figure 3.30: [Ca VIII]λ23210 image and nuclear spectrum extraction of 0.46″ diameter.

Table 3.1 - The [Ca VIII]λ23210 nuclear spectrum fit parameters. The kinematics of the narrow (n) and broader (b) components are shown in terms of the velocities (v_X) and velocity dispersion (σ_X). Other columns show the flux measured for the [Ca VIII]λ23210 and Brγ and their respective luminosities.

v_n([CaVIII])	σ_n([CaVIII])	v_b([CaVIII])	σ_b([CaVIII])	[CaVIII](10^{-16}ergs^{-1}cm^{-2})	Brγ(10^{-16}ergs^{-1}cm^{-2})	$L_{[CaVIII]}$(erg/s)	$L_{Br\gamma}$(erg/s)
131 ± 1.46	88.2 ± 0.843	-23.3 ± 3.48	127 ± 0.715	1.88e+03 ± 31.1	4.22e+03 ± 33.7	2.91e+39 ± 2.68e+39	6.52e+39 ± 6e+39

The [Fe VII]λ6086 is the more extended coronal line observed in the NGC 5643 nucleus. Figure 3.31 shows its flux, velocity, and velocity dispersion. Such emission is extended along with the ionization cones. Towards the eastern side, the velocity dispersion is higher in spatially coincident regions with the bright knots seen in [OIII]λ5007 high velocity gas. However, the highest dispersion values are achieved on the western side and may be related to the cone edges in that direction.

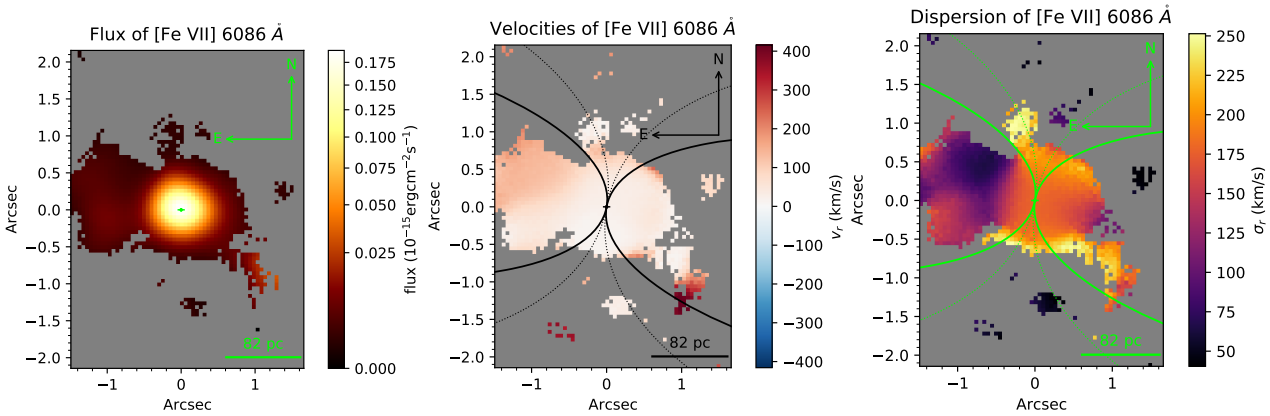

Figure 3.31: Flux, velocity, and velocity dispersion resulting for a decomposition of [Fe VII]λ6086 emission-line using one Gaussian component. The ionization bicone walls are indicated in the velocity and velocity dispersion maps.

The [Fe VII]λ6086 is possibly associated with outflows. A blueshift wing image from 6077-6085 $\mathring{A}$ is presented in figure 3.32. There is off-nuclear emission on both sides, but more prominent at the eastern cone. Nuclear and 0.97″ to east extractions are presented in the right upper and bottom panels of figure 3.32. The Table 3.2 show that the nuclear wing is broader, achieving FWHM $\approx$ 539 km/s, while the extraction towards 0.97″ to the east has about FWHM $\approx$ 200 km/s. This region 0.97″ from the nucleus is almost aligned with the radio emission orientation and with a bright emission of [OIII]λ5007 in high velocities as shown in figure 3.11.

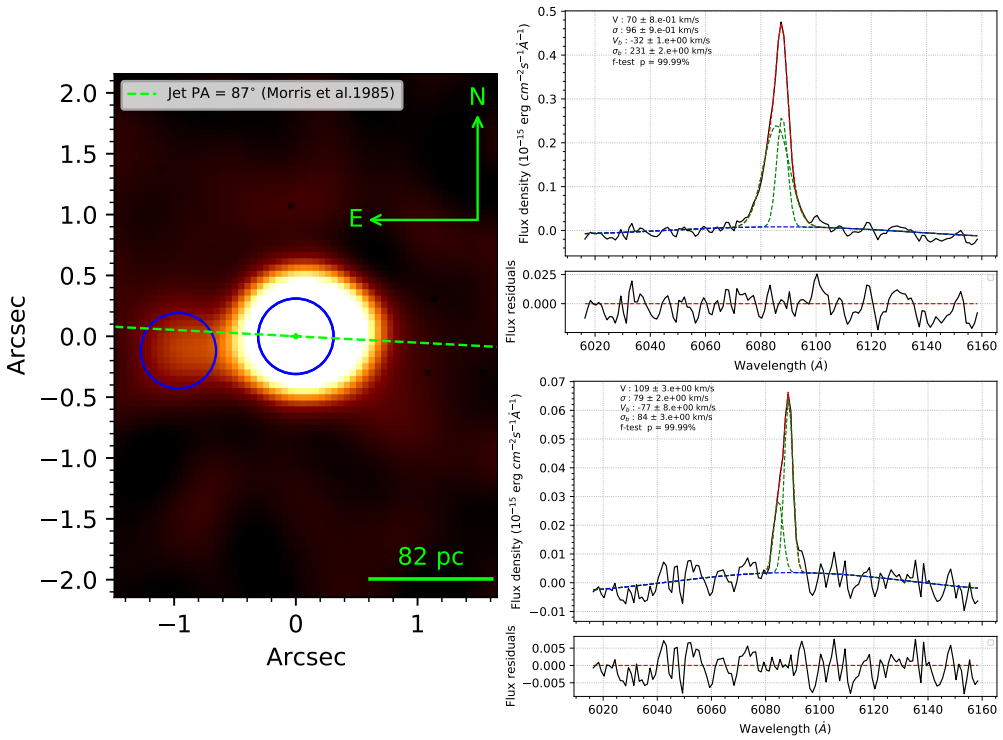

Figure 3.32: On the left, image of the blueshift component of [FeVII]λ6086, with extraction areas indicated by the blue circles. On the right side, the emission line profile for the nuclear (top) and 0.97″ towards east extraction (bottom). The radio emission with PA = 87° is shown as a dashed line.

Table 3.2 - The [Fe VII]λ6086 fit parameters for the nuclear spectra and 0.97″ towards east. The kinematics of the narrow (n) and broader (b) components are shown in terms of the velocities (v_X) and velocity dispersion (σ_X). Other columns show the extinction corrected flux and luminosities of [Fe VII]λ6086. Additionally, the final column presents the [Fe VII]λ6086/Hβ ratio.

r(as)	v_n([FeVII])(km/s)	σ_n([FeVII])(km/s)	v_b([FeVII])	σ_b([FeVII])	[FeVII]$_0$(10^{-15}ergs^{-1}cm^{-2})	$L_{[FeVII]}$(erg/s)	[FeVII]/Hβ
Nuclear	65.9 ± 0.854	97.1 ± 6.51	-41.6 ± 31.6	229 ± 9.51	11.8 ± 0.872	1.83e+38 ± 1.69e+38	0.118 ± 0.00891
0.973	104 ± 12.9	78.3 ± 7.33	-72.5 ± 25.3	85.8 ± 11	0.7 ± 0.136	1.08e+37 ± 1.02e+37	0.121 ± 0.0236

From the extractions defined in figure 3.8 we can analyze the high-velocity gas kinematics to constrain better the [Fe VII]λ6086 outflows. Figure 3.33 presents the velocities and velocity dispersion values for the [Fe VII]λ6086 broader component. Beyond the nucleus, subjacent regions towards the south, southeast, southwest, and north presented outflows with FWHM $\approx$ 500-560 km/s. The north and southwest extractions seem to be in redshift. On the other hand, the outflows are in blueshift in the nucleus and towards the south and southeast. This pattern in the kinematics resembles the outflows found previously for [OIII]λ5007 and Hα, although more concentrated in the vicinity of the nuclear region.

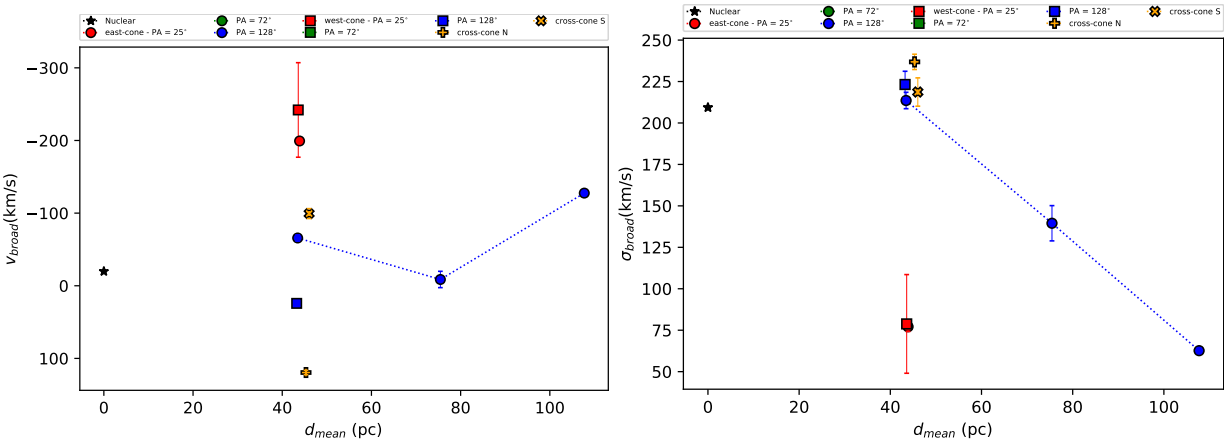

Figure 3.33: Radial profile of [Fe VII]λ6086 broader component velocities v_b and velocity dispersion σ_b. Upper plots legend indicate where the extraction is localized in the scheme of figure 3.8.

The emission-line ratio [Fe VII]λ6086/Hβ made for spaxels and for some areas of extraction are shown in figure 3.32. Apparently, [Fe VII]λ6086 drops more slowly than Hβ in some regions. Towards the east, the same bright region shown in figure 3.32 has a higher ratio than in the nucleus. Such region is aligned with the radio jet orientation. The west side regions at the northwest and southwest also exceed the ratio found in the nucleus. Integrated spectra confirm these results, showing a radial increase at PA = 72 ° in the central east cone. Towards the southwest at PA = 128 °, there is the maximum ratio of [Fe VII]λ6086/H$\beta \approx 0.134$.

Besides the alignment with the radio emission, [Fe VII]λ6086/Hβ enhanced regions are associated or in the vicinity of outflows. Towards the east, the bright high velocity component of [Fe VII]λ6086 shown in figure 3.32 is co-spatial to the high velocity emission of [OIII] seen in figure 3.12. Towards the west the [Fe VII]λ6086/Hβ enhanced regions are on the direction of ionization cone edges. The southwest [Fe VII]λ6086/Hβ excess also show a diffuse emission in the [Fe VII]λ6086 high velocity map of figure 3.32.

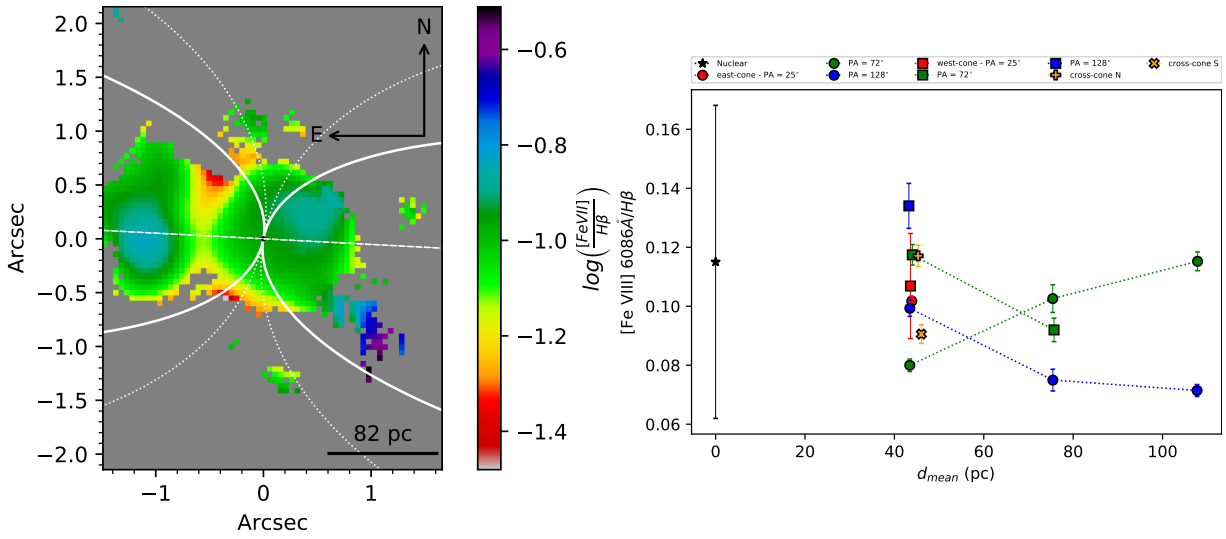

Figure 3.34: The [Fe VII]λ6086/Hβ emission-line ratio made for spaxels (left) and their radial profile for the spectra extractions (right). Ionization cone edges are shown as white curves and the radio jet orientation as a white dashed line.

A test can be made fitting the emission lines radial profiles. This method was adopted in recent works (Singh et al., 2013; Negus et al., 2021). The assumption here is that, in the absence of other energy sources, being the unresolved AGN continuum as a point source, the luminosity of the emission lines fluxes should decay with the inverse square law with the distance, a R^{-2} profile. Negus et al. (2021) used this argument to determine the ionization source behind coronal emission in a sample of galaxies from the MANGA survey. They found shallower profiles, with power-law indexes between $|\alpha| \approx 0.6$ to 1.8 for the AGNs, suggesting a mixing between ionization mechanisms. Our profiles are presented in figure 3.35. The R^{-2} expected profile is shown as a black dashed line, while the average radial profile of the different directions is indicated as a red dashed one. A shallower decrease was found for all of them, with similar slopes in the range $\alpha = 0.69$-0.74. Even after convolving the R^{-2} profile with a Gaussian of FWHM $= 0.62''$ representing the PSF, as shown in the green dashed line in figure 3.35, the data is not likely compatible with them. This result suggests that an additional source, likely due to shocks that may be are driven by a radio jet or winds, can be impacting the [Fe VII]λ6086 emission. More than that, the current plots imply that [Fe VII]λ6086 is not being impacted isolated. Nearly the same slopes were derived for [OIII]λ5007, [Fe VII]λ6086, and Hα. This result points to the same mechanisms acting on [Fe VII]λ6086 are also affecting the other lines.

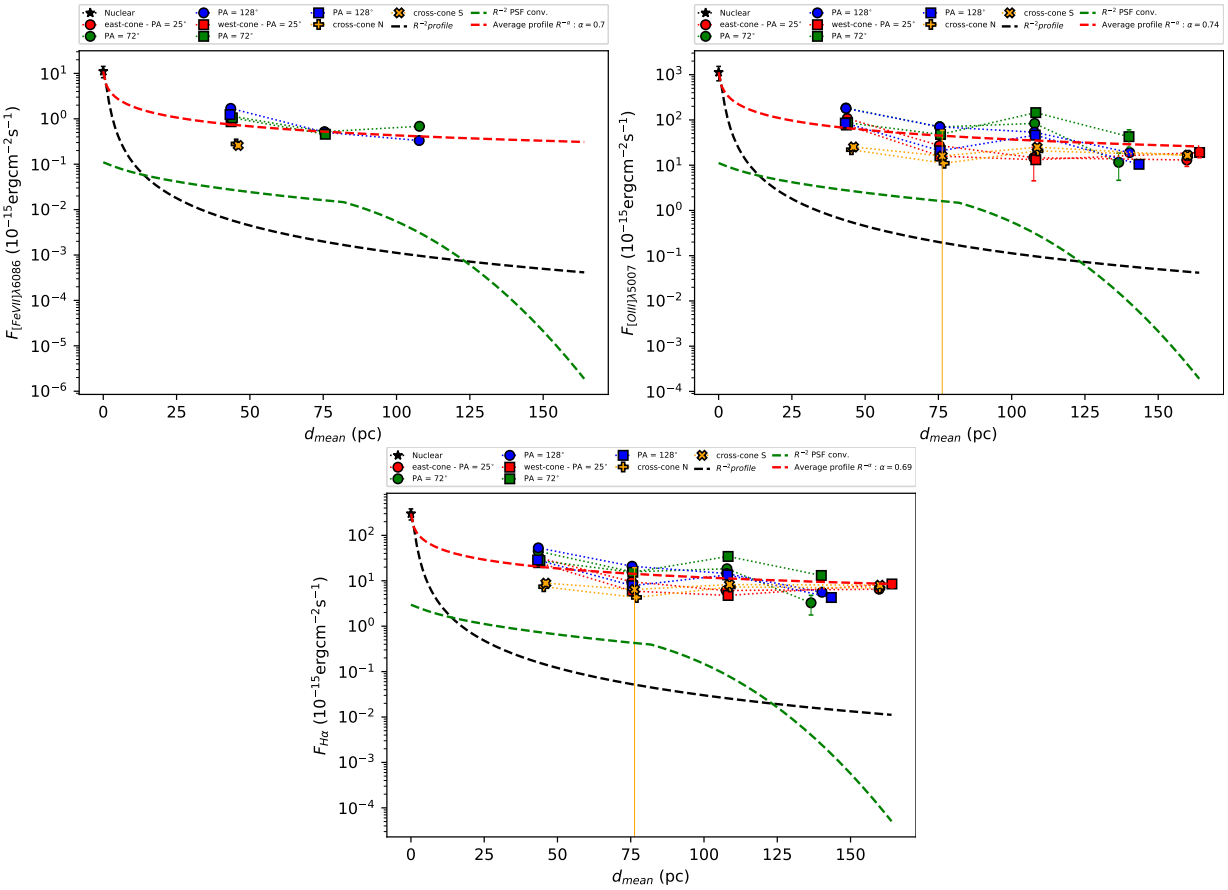

Figure 3.35: Flux profiles of [Fe VII]λ6086, [OIII]λ5007, and Hα. The expected inverse square law profile is shown as a black dashed line, while the convolved with the PSF as a green dashed line. The average fitted profile of the different orientations is shown as a red dashed line.

Chapter 4

Discussion

4.1 Narrow Line Region

Our results unveil how the narrow line region gas is distributed in the few hundred central parsecs of NGC 5643. Most of the ionized gas is emitted along a double-sided ionization bicone, shown from the neutral up to highly ionized gas. The emission line channel maps of [Fe II]λ16440, seen in figure 4.1, represent well the general gas behavior. Besides the emission closer to the ionization axis, an hourglass morphology is seen far beyond. We interpreted this morphology as the ionization bicone walls. Previous studies also found this kind of structure to other galaxies (May and Steiner, 2017; da Silva et al., 2020; Riffel et al., 2021). The general trend towards the eastern side is the redshifted gas filling the cone and the blueshifted one emitted on the cone edges. On the other hand, the blueshifted gas fills the cones towards the west, and the walls are redshifted. Extinction corrected optical lines often follow a similar pattern. The extended emission is in agreement with what was found for [OIII]λ5007 in Mingozzi et al. (2019), presented in figure 1.10. While they do not show clear signs of being the bicone edges, the arc shape is present on both sides. A similar map for [OIII]λ5007 was published in Venturi et al. (2021) and resembles our [Fe II]λ16440 observations. The inner bicone kinematics and probably hints of the bicone edges were also observed for [SIII]λ9069 in Riffel et al. (2018).

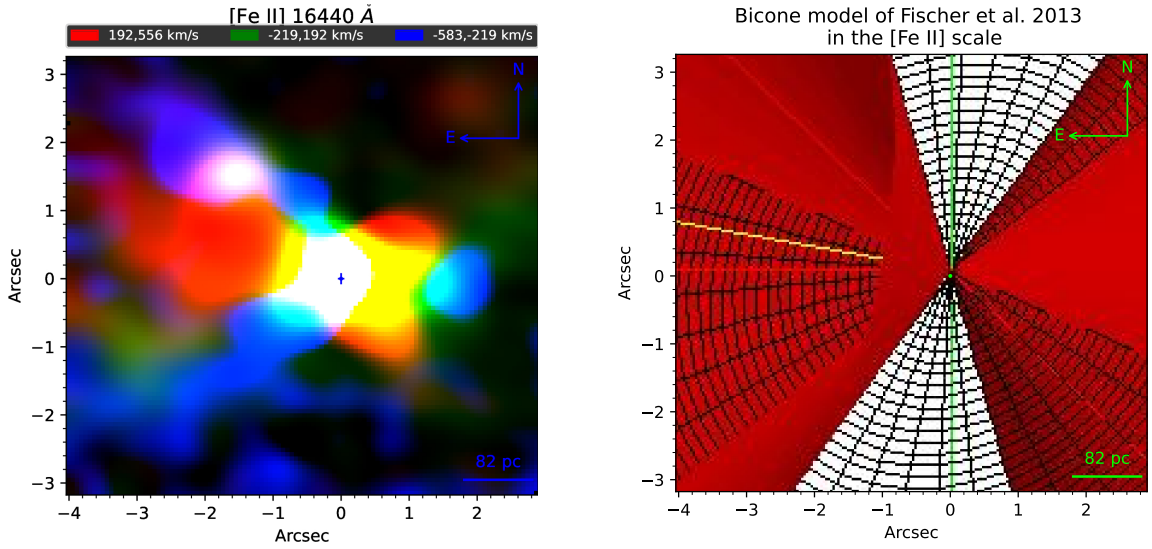

Figure 4.1: On the left is our [Fe II]λ16440 RGB. To the right is the adapted figure of the cone model from Fischer et al. (2013) in the [Fe II]λ16440 physical scales. The ionization cone is seen in red. The galaxy disc is represented as the black grid. Regions of the cones below the disc are predicted to be in redshift. Regions of the cones above the disk will be mainly in blueshift.

The ionization cones modeled in Fischer et al. (2013) qualitatively agree with our observations. Figure 4.1 show the [Fe II]λ16440 velocity RGB and the ionization bicone model of Fischer et al. (2013) adapted to the same scale. The galaxy disc is not face on, but inclined i $\approx 30°$, being the northeast region the far side. The Fischer et al. (2013) ionization cone, on the other hand, is tilted across the disc. The authors found an i $\approx 25°$ against the plane of the sky with the southeast side in our direction. The model predicts blueshifted emission coming from the eastern cone edges and on the western cone top wall. Also, most of the western cone edges are going into the disc, therefore, redshifted. Redshifted emission is also expected to fill the cone on the east side. All these patterns can explain, to some extent, the ionization bicone structure observed on the emission lines.

We found different behaviors in the distribution of gas of different ionization degrees and kinematics. As seen in figure 3.11, while the [OIII]λ5007 shows emission more concentrated towards the bicones, the low-ionization lines are more regularly distributed, until much farther out. This result indicates a drop in the ionization degree in the outskirts. Low-ionization lines presented gas emission of high velocity, traced by the broader component, mostly in the cone edges and cross-cone region, as shown in figure 3.13. In contrast, the narrow component dominates the inner area of the cones on both sides. A different scenario was seen for [OIII]λ5007. The [OIII]λ5007 emission was seen much more

concentrated, with the low and high-velocity gas emitted across the bicone. Figures 3.12 and 3.13 show that the high-velocity gas of [OIII]λ5007 presented two bright nodes of emission towards the east and also presented some excess towards the west cone.

The H_2 1-0 S(1)λ21218 molecular gas shown in figure 3.14 is distributed along a circumnuclear spiral also found in previous works, for the cool molecular gas (Alonso-Herrero et al., 2018) and hot molecular gas and dust (Davies et al., 2014; Menezes et al., 2015). In addition, the emission of H_2 1-0 S(1)λ21218 was seen associated with the ionization bicone walls towards the east side. The more extended emission inside the cones is towards the southeast, where the highest velocity ionized outflows were detected.

The dust extinction traced in the ionized phase shown in figure 3.20 reveals values between 0.06 mag $\leq$ Av $\leq$ 4.4 mag. Regions towards the north, south, and west sides were strongly attenuated by dust. Our results seem compatible with Simpson et al. (1997) that find a dust lane with an arc shape at 1″ from the nucleus towards the west side. Also, our extinction map resembles the dusty structure found for Cresci et al. (2015), that presents Av $>$ 3 magnitudes towards the west side, achieving a maximum of Av $\approx$ 4.8 magnitudes. We found the peak of extinction, measured from their radial profile, around 1.32″ from the nucleus in different directions. An exception was found towards the northeast side, where the extinction presented a decreasing radial behavior.

Our results for the stellar extinction, shown in figure 3.20 presented similar structures than seen in the ionized gas extinction. The overall shape of the stellar extinction is a perturbed dusty ring. Towards northeast and around the east cone, the ionized extinction becomes lower than measured from the stellar extinction. A possible reason can be seen in the color index map of figure 1.7 from Davies et al. (2014). While the whole ring structure is attenuating the stars in the background, the east cone gas, mainly at the northeast, is in front of the dust ring, not being highly obscured by it. This possible explanation supports the ionization bicone being tilted relative to the galaxy plane, which was proposed in several studies (Schmitt et al., 1994; Simpson et al., 1997; Fischer et al., 2013; Cresci et al., 2015).

There is important to mention that, even if the impact of dust is smaller for the gas on the eastern side, part of the emission comes from gas being obscured by dust in the disc. The extinction of the eastern cone becomes as high as $A_v \approx 1.5$ mag between -1″ and 1″ in the north-south direction. The same region presents the highest electron density

values inside the eastern cone, which also suggests that part of the emission originates closer to the disc.

In addition, the dusty ring that we found in the stellar extinction have similar dimensions than a molecular gas ring proposed in Davies et al. (2014). Davies et al. (2014) used a hydrodynamic simulation to understand the molecular kinematics and found that the circumnuclear spiral arms are possibly feeding a molecular ring, represented in figure 1.7. Since the molecular gas and the dust are coupled, how demonstrated in Alonso-Herrero et al. (2018) with figure 1.9, our dusty ring found in the stellar extinction is possibly associated with the molecular ring predicted by Davies et al. (2014).

We obtain estimates for the electron temperatures and densities using [NII]$\lambda\lambda$ 5755,6548,6583 and [SII]$\lambda\lambda$6716,6731 emission lines as shown in figure 3.23. There are no previous electron temperature estimates for this galaxy in the literature. The electron temperatures present their highest values in the direction of the cone walls. High temperatures outside the ionization axis are suggestive of shocks contribution, as shown in Riffel et al. (2021). Large errors in the temperature determination, however, make their values compatible with the nuclear. The global electron temperatures were found around $T_e \approx 10^4$ K, typical of photoionized gas.

The electron density found in the nucleus was $n_e \approx 1230 \pm 60\ cm^{-3}$. Towards the west, the electron densities are much higher than seen on the east side. The peak was found at $0.2''$ towards the west achieving $n_e \approx 1350 \pm 150\ cm^{-3}$, but the measurement is compatible with the nuclear value, given the uncertainties. The density remains as high as the nuclear until $0.5''$ towards the west. Although there is a drop in densities farther out, electron densities remain as high as $n_e \approx 960 \pm 160\ cm^{-3}$ at least until $0.7''$ towards the west. Electron densities at constant $T_e = 10^4$ K suggested an even more extended high-density region, but the uncertainties make these results not reliable. On the east side, densities are high just along the ionization axis of the cone, reaching $n_e \approx 830 \pm 70\ cm^{-3}$ at $0.47''$ from the nucleus.

The electron densities found in our work are in disagreement with the literature. Schmitt et al. (1994), presented long-slit spectroscopy of $0.9''$/pixel from the CTIO 4m-telescope, using the [SII]$\lambda\lambda$6716,6731 emission lines to estimate the densities. The authors found higher densities towards the west, but lower values than our work, of about $n_e \approx 200\ cm^{-3}$ in the nucleus and $n_e \approx 450\ cm^{-3}$ in regions $1.8''$ and $3.6''$ towards the west

side. Cresci et al. (2015) used a MUSE data cube to estimate the densities using the [SII]$\lambda\lambda$6716,6731 emission lines and assuming a constant electron temperature of $T_e = 10^4$ K. The authors found a density in the nucleus higher than the critical density of the lines. Measurement that they argue to be very uncertain. In agreement with our measurements, the authors found densities often lower than $n_e \approx 1000\ cm^{-3}$. Their map, however, suggests the largest densities extended towards the east side, which was not verified in our results. Our better spatial resolution and sensitivity to some previous works in the central regions can be the reason behind the disagreements.

4.2 Kinematics and Outflows

Emission lines were fitted for the individual spaxels with a narrow plus a slightly broader Gaussian component. We often assume that this broader one, if shifted from the narrow bulk velocities, is tracing outflows. For fainter emission lines and the H_2 1-0 S(1)λ21218, just a Gaussian component was fitted. Individual spectral extractions were fitted with support of an F-test described in appendix A.3. From that results, we ensured the necessity of at least two Gaussian components for most of the ionized emission lines.

The ionized gas narrow component showed the large-scale rotation towards the PA $\approx 138°$ and clear deviations from these motions inside the ionization bicone. We interpret these deviations as low-velocity biconical outflows in the inner cones. The kinematics shows redshifted motions inside the east cone and blueshifted towards the west one. This behavior is also present in the hot molecular gas of H_2 1-0 S(1)λ21218, in agreement with the kinematics shown in Davies et al. (2014). The authors explained this rotation deviation in the molecular gas with a hydrodynamical simulation, including a molecular ring fed by the circumnuclear spiral. However, the authors also found outflows in the molecular gas, with the most important towards the northeast, as we also found. These low-velocity bipolar outflows may be related to outflows in the torus. Alonso-Herrero et al. (2018) analyzed the ALMA cold molecular gas and found a 26 pc diameter nuclear disc almost edge-on towards the north-south direction. The nuclear disc, almost perpendicular to the ionization cones, shows a radial velocity component towards the direction of the cones, redshifted towards the east and blueshifted towards the west. The authors suggested that these could be outflows coming from the nuclear disc. This scenario could also be

responsible for the low-velocity outflows observed inside the ionization cones.

We found the narrow component kinematics for the Hα and the low-ionization emission lines are similar to the H_2 1-0 S(1)λ21218. Their velocity and velocity dispersion maps, shown in figure 3.18, presented almost the same structures and similar regions enhanced. This connection between the lines can suggest that the Hα and low-ionization lines narrow component are co-spatial to the molecular phase and probably coming from the disc.

The low-velocity biconical outflows in the ionized and molecular gas are more prominent towards the northeast-southwest direction. The Hα presented -317 km/s $\leq v_{H\alpha} \pm 2\sigma_{H\alpha} \leq$ 496 km/s and FWHM $\leq$ 476 km/s. Similarly, in [OIII]λ5007 we found -326 km/s $\leq v_{[OIII]} \pm 2\sigma_{[OIII]} \leq$ 402 km/s and FWHM $\leq$ 389 km/s. The hot molecular gas of H_2 1-0 S(1)λ21218 shows similar values inside the GMOS FoV, but exhibit higher outflow velocities towards northeast farther out, reaching -661 km/s $\leq v_{H_2} \pm 2\sigma_{H_2} \leq$ 596 km/s and FWHM $\leq$ 542 km/s.

We find out high-velocity outflows, more often in blueshift. Redshifted outflows were seen inside the eastern cone and on the edges of the western cone. The highest velocity outflow is in blueshift mainly towards the southeast, associated with the walls in the eastern ionization cone. Similar blueshifted outflow towards the southeast was already found in Cresci et al. (2015). Especially for [OIII]λ5007, we find a similar high-velocity blueshifted outflow inside the western cone.

With our improved spatial and spectral resolution, it was possible to better constrain the outflow distribution and velocities. The Hα exhibited -950 km/s $\leq v_{H\alpha} \pm 2\sigma_{H\alpha} \leq$ 621 km/s and FWHM $\leq$ 926 km/s. For [OIII]λ5007 we found -1028 km/s $\leq v_{[OIII]} \pm 2\sigma_{[OIII]} \leq$ 665 km/s and FWHM $\leq$ 824 km/s. The velocities range is much more asymmetric for blueshift than found in the low-velocity outflows. The main reason is the highest blueshift velocities on the edge of the eastern cone and inside the western cone. The reached velocities are much higher than the maximum velocity of 500 km/s proposed in the model of Fischer et al. (2013).

In the [Fe VII]λ6086, the spectral extractions show a broader component inside the cones in the vicinity of the nuclear region towards the south, southeast, southwest, and north. The velocity range found was -537 km/s $\leq v_{[FeVII]} \pm 2\sigma_{[FeVII]} \leq$ 593 km/s and FWHM $\leq$ 560 km/s.

The fact that the highest velocities outflows were found in blueshifted can be, at least to some extent, a matter of orientation. Assuming that the narrow component is tracing the gas closer to the galaxy disc, almost face-on implies a small fraction of the deprojected velocity in the radial velocity component. For the gas emitted in the tilted outflowing bicone proposed by Fischer et al. (2013) and with the gas coming towards our direction, the radial component presents a higher fraction of the deprojected velocity of the outflow.

Towards the cross-cone region, there are some velocity dispersion enhanced regions. Part of them can be associated with outflows not limited to the ionization cones, but some can reveal turbulence. Venturi et al. (2021) showed, for a sample including NGC 5643, that low-power jets at low inclinations respective to the galaxy plane can produce turbulence in the galaxy disc perpendicular to the cones towards kiloparsec-scales. They detected the signature as a line broadening without bulk velocities too much deviated from the ordinary rotating component. Turbulent gas is not outflowing in some direction, and the perturbation is just increasing the local velocity dispersion. For NGC 5643, they found signatures of turbulence until 3 kiloparsecs in the perpendicular direction to the cones.

4.3 Excitation and Coronal Emission Lines

Diagnostic diagrams indicated the AGN as the primary source of ionization. A few regions, mainly towards the cone edges on the northeast and southeast sides, show LINER-like line ratios. These results were also found in recent works (Cresci et al., 2015; Mingozzi et al., 2019; Ma et al., 2021).

Cresci et al. (2015) presented, looking at scales of tens of arc seconds perpendicular to the cones, that there are LINER-like regions around the Seyfert-like spaxels. Ma et al. (2021) found these LINER cocoons and suggested being caused by the diminished AGN radiation or shocks when jets are present. Possibly, part of this LINER structure was found in our field. The highest low-ionization line ratios in the edges of the cones, when associated with large velocity dispersion values, are suggestive of shocks according to the models used in Mingozzi et al. (2019). However, a large contribution from the partially ionized zone due to an attenuation of the AGN continuum on the outskirts is possibly also present.

Another argument that favors the drop of ionization degree is the radial increase seen in the low-ionization line ratios, when the opposite occurs for the high-ionization ratios. We find the lowest [SII]$\lambda\lambda$6716,6731/Hα ratios were associated with the ionization cones, while the highest values were found at the edges of the cones. This trend was also reported in Mingozzi et al. (2019). The authors argued for a NLR composed of matter-bounded and ionization-bounded clouds, first proposed by Binette et al. (1996).

We also find an unusual enhancement of Hα and [OIII]λ5007 relative to low-ionization lines in the cross-cone region. Some line ratio values found were similar to what was observed in the direction of the cones. Their distribution and line ratios suggest a link with the west cone. One possible hypothesis is the photoionization by radiation leaking from the torus found in the work of Jones et al. (2021). The authors analyzed Chandra observations and found extended hard x-rays emission until 360 pc or $\approx 4''$ in the cross-cone region.

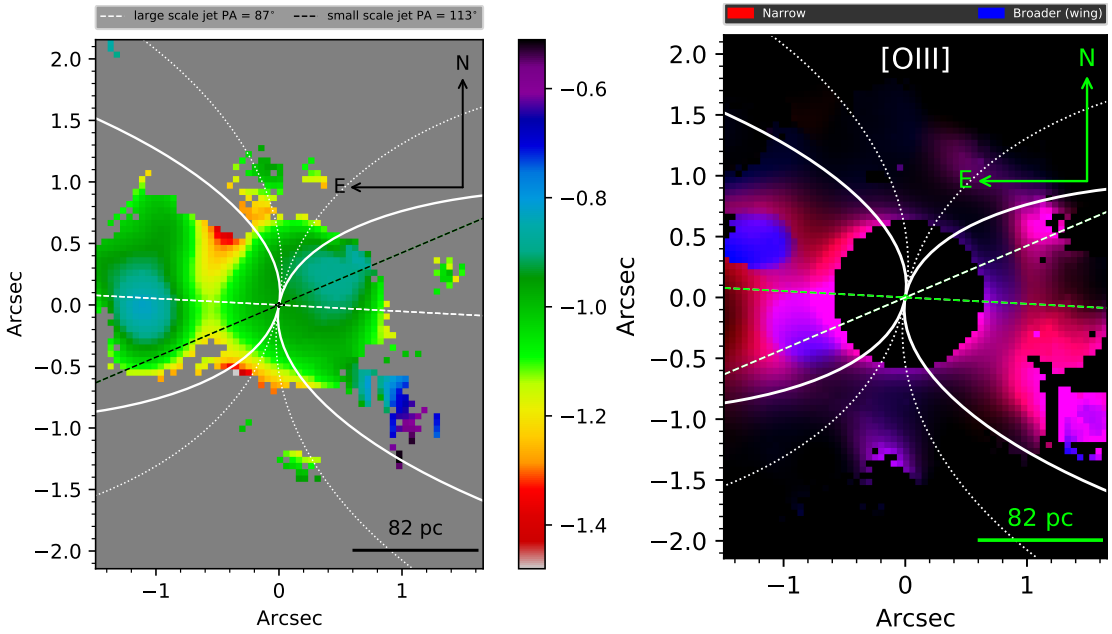

Figure 4.2: [Fe VII]λ6086/Hβ and, narrow and the broader [OIII]λ5007 distribution. Curves indicate the ionization cones walls derived with [Fe II]. The maps also indicate the orientation of the large scale radio jet at PA = 87° (Morris et al., 1985) and the small scale one at PA = 113° (Simpson et al., 1997).

The more substantial evidence of an additional ionization source comes from the coronal emission lines. Enhanced regions in [Fe VII]λ6086/Hβ were found on both sides of the cones, as shown in figure 4.2. Higher ratios than seen in the nucleus were observed until up to $\approx$ 100 parsecs away. This high ionization far from the nucleus may suggest fast

shock ionization. The enhanced regions are in the inner east ionization cone and two areas towards the west side directed to the cone edges. Fonseca-Faria et al. (2021) using MUSE observations, found [Fe VII]λ6086 extended until 800 pc and 900 pc towards the east and west side. The authors relate the enhanced regions on their sample with the passage of radio jets.

We then tested the jet orientation relative to the [Fe VII]λ6086/Hβ enhanced regions. Simpson et al. (1997) found that the jet at small scales has a different orientation. The small-scale jet is pointing towards PA = 113 ° as seen in figure 1.5. At that time, they found the jet aligned with a high excitation region across the cones, with higher [OIII]λ5007/Hβ, which the authors suggested was evidence for jet-ISM interaction. The large and small-scale jet orientations are shown in figure 4.2 superposed on our [Fe VII]λ6086/Hβ ratio map and the RB map of [OIII]λ5007. High [Fe VII]/Hβ in the inner east cone is aligned with the large-scale jet and the northwest with the small-scale one. Our results point to a connection between the ionization and the radio jet, as suggested in Fonseca-Faria et al. (2021) and Simpson et al. (1997).

We also find further reasons to link the radio jet with the production of outflows. The [OIII]λ5007 RB map in the figure 4.2 shows that bright regions in blue, tracing outflows, are aligned to the small-scale jet on both sides at PA = 113°. Besides that, the regions of larger FHWM in figure 4.3 for the outflowing gas, especially towards the southeast, are aligned with the jet found in Simpson et al. (1997). The jet impact was previously suggested in the literature. Cresci et al. (2015) suggested that the eastern blueshifted outflow is related to the soft X-rays and the radio emission. García-Bernete et al. (2021) make a deep analysis of the energetics of the outflows in different phases, and found that it is likely that the jet is playing a role in them. These results suggest that at least part of the outflows observed can be associated with the jet.

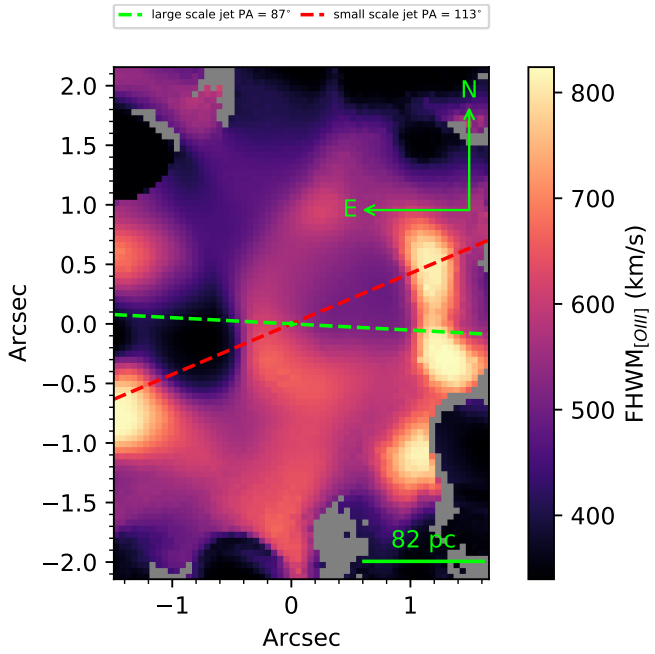

Figure 4.3: [OIII]λ5007 broader component FWHM. The dashed lines indicate the orientation of the radio jet as found from Morris et al. (1985) and Simpson et al. (1997).

Another important find comes from the fluxes of emission lines. Flux profiles of Hα, [OIII]λ5007 and [Fe VII]λ6086 presented power indexes in the range $|\alpha|$ = 0.69-0.74 respective to the distance. The obtained profiles showed a shallower decline relative to the R^{-2} profile expected for a pure AGN photoionization (Singh et al., 2013; Negus et al., 2021). This result points to an additional and extended ionization source, likely winds or a radio jet, that are also affecting other emission lines besides [Fe VII]λ6086.

Chapter 5

Conclusions and perspectives

This work presented a detailed analysis of the few central hundreds of parsecs of NGC 5643. Our primary focus was on the emission line properties in the nuclear and circumnuclear region. Optical and NIR IFU spectroscopy of high spatial resolution were used to produce a very accurate description of the NLR of this galaxy. The optical data cube has a high spatial resolution, which is an advantage to similar works as Cresci et al. (2015), and higher spectral resolution than presented in the literature (Simpson et al., 1997; Davies et al., 2014; García-Bernete et al., 2021). We examined the gas distribution, kinematics, and excitation at different gas phases and ionization degrees. Special attention was given to the ionization cones emission distribution and kinematics, multiphase outflows, and the highly ionized gas emission. Our main findings and conclusions are summarized as follows:

- Most of the ionized gas emission is seen along a double-sided ionization cone. The [Fe II]λ16440 emission line, less affected by dust, presented an hourglass morphology outside the ionization axis, what we interpret as the ionization bicone walls. The general emission pattern agrees with the Fischer et al. (2013) ionization cones model;

- We found the low-ionization gas emission more regularly distributed until far away from the ionization axis. The lines present the high-velocity gas (broader component) in the cone edges and cross-cone region. This finding suggests outflows and turbulence as possible causes. The narrow component dominates in the inner region of the cones on both sides. For [OIII]λ5007 both components were found concentrated across the cones;

- The stellar extinction appears to reveal a disturbed ring of dust, probably associated with a molecular gas ring that is being fed by a circumnuclear spiral, predicted by

(Davies et al., 2014);

- While towards the western side, ionized gas extinction reaches up to Av = 4.4 magnitudes, on the eastern cone the extinction is much smaller, almost not affected by dust towards the northeast side. This result can be explained if the main emission comes from gas above the dust that obscures the disc. This finding is compatible with the ionization cones tilted relative to the galaxy disc (Fischer et al., 2013);

- We obtain the first spatially resolved electron temperature estimates for NGC 5643. The highest temperatures are in the direction of the cone edges, suggesting the presence of shocks. The errors, although, make these values compatible with the nuclear ones. Electron temperatures were found around $T_e \approx 10^4$ K, values compatible with photoionized gas;

- Electron density presented $n_e \approx 1230 \pm 60\ cm^{-3}$ in the nucleus. Towards the east, densities exhibit a faster radial decline, achieving $n_e \approx 830 \pm 70\ cm^{-3}$ at $0.47''$ from the nucleus along the ionization axis. In contrast, towards the west densities showed a high density region, remained as high as $n_e \approx 1200 \pm 120\ cm^{-3}$ until $0.47''$ from the nucleus. The densities found in our work are in disagreement with previous works (Schmitt et al., 1994; Cresci et al., 2015). Our better spatial resolution may be the cause of these differences.

- At least two Gaussian components were required to fit the ionized gas kinematics. The narrow component seems to trace complex rotation superposed to low-velocity biconical outflows of FWHM (Hα) $\leq$ 476 km/s. We found the low-velocity outflows are more prominent crossing the nucleus, in the northeast-southwest direction. Similar kinematics were found in the H_2 molecular gas, also reported in Davies et al. (2014), reaching until FWHM (H_2) $\leq$ 542 km/s outside the GMOS FoV.

- We find similar structures in the Hα narrow component and the H_2 kinematics. This suggests that both phases are almost co-spatial and likely closer to the galaxy disc;

- We also find high-velocity outflows. The highest-velocity ones were found in blueshift, associated with the eastern cone walls and in the inner west cone. The former one was first reported in Cresci et al. (2015). We constrain the outflow kinematics, finding

FWHM (Hα) $\leq$ 926 km/s. The gas reaches velocities of -1000 km/s in [OIII], much higher than predicted in previous models (Fischer et al., 2013);

- The coronal emission line of [Fe VII]λ6086 also presented outflows. The highest velocity outflows were found in the vicinity of the nucleus, with FWHM $\leq$ 560 km/s;
- Our analysis suggests that the AGN continuum is likely the primary ionization source. However, a strong indication of an additional energy source was found. We find evidence of fast shocks mainly in the bicone region, revealed by enhanced [Fe VII]λ6086/Hβ line ratios aligned with the radio jet. Fonseca-Faria et al. (2021) already associated the [Fe VII]λ6086 emission in NGC 5643 with the radio jet. The enhanced regions are also associated with bright [OIII]λ5007 emission regions tracing outflows. These results suggest the compact jet as a driver of fast shocks, impacting the ionization and kinematics of the gas;
- Flux profiles of [OIII]λ5007, Hα and [Fe VII]λ6086 presented a shallower decline than expected for pure AGN photoionization. The lines exhibited similar power indexes of $|\alpha|$ = 0.69-0.74. This result also suggests the necessity of an additional source of ionization.

The results presented show how complex is the central region of NGC 5643. Our findings suggest that although of low power, the radio jet can substantially impact the gas ionization and kinematics in NGC 5643, at least at scales of a few hundreds of parsecs. This work helps us confirm previous literature findings and brings new insights about the central region of NGC 5643. Comprehensive studies of nearby galaxies, like this one, allowed us to unveil the interface between the AGN domain and their hosts, with quality yet not accessible for the high redshift Universe.

5.1 Perspectives

Up to the moment, one event proceeding from the International Astronomical Union (IAU) was published with the Master's first semester results (Cezar et al., 2021). Our complete findings are expected to be published this year in a high-impact international journal. A couple of things possibly will be done to finalize this work. We intend to use

photoionization and shock models to explain the line ratios. The focus is to complement evidence and give us support to interpret the results better.

Our work reveals how complex the central regions of galaxies are. Indeed, for NGC 5643 and other galaxies, the future could not be brighter. The new generation of giant telescopes, beginning this year with the JWST first light, will open our eyes to other wavelength windows to be explored. For nearby AGNs, the increased spatial resolution and detailed studies at longer wavelengths can be the key to further understanding the impact of AGNs on their hosts.

Bibliography

Allen M. G., Groves B. A., Dopita M. A., Sutherland R. S., Kewley L. J., The MAPPINGS III Library of Fast Radiative Shock Models, The Astrophysical Journal Supplement Series, 2008, vol. 178, p. 20

Allington-smith J., Content R., Spectroscopy I. F., Sampling and Background Subtraction in Fiber - Lenslet Integral Field Spectrographs Author (s): Jeremy Allington - Smith and Robert Content Source : Publications of the Astronomical Society of the Pacific , Vol . 110 , No . 752 (October Published by :, 1998, vol. 110, p. 1216

Almeida C. R., Ricci C., Nuclear obscuration in active galactic nuclei, Nature Astronomy, 2017, vol. 1

Alonso-Herrero A., Pereira-Santaella M., García-Burillo S., Davies R. I., Combes F., Asmus D., Bunker A., Díaz-Santos T., Gandhi P., González-Martín O., Hernán-Caballero A., Hicks E., Hönig S., Labiano A., Levenson N. A., Packham C., Almeida C. R., Ricci C., Rigopoulou D., Rosario D., Sani E., Ward M. J., Resolving the Nuclear Obscuring Disk in the Compton-thick Seyfert Galaxy NGC 5643 with ALMA, The Astrophysical Journal, 2018, vol. 859, p. 144

Annuar A., Gandhi P., Alexander D. M., Lansbury G. B., Arévalo P., Ballantyne D. R., Baloković M., Bauer F. E., Boggs S. E., Brandt W. N., Brightman M., Christensen F. E., Craig W. W., Moro A. D., Hailey C. J., Harrison F. A., Hickox R. C., Matt G., Puccetti S., Ricci C., Rigby J. R., Stern D., Walton D. J., Zappacosta L., Zhang W., NuSTAR OBSERVATIONS OF THE COMPTON-THICK ACTIVE GALACTIC NUCLEUS AND ULTRALUMINOUS X-RAY SOURCE CANDIDATE IN NGC 5643, The Astrophysical Journal, 2015, vol. 815, p. 36

Antonucci R., Unified models for active galactic nuclei and quasars., Annual Rev. Astron. Astrophys, 1993, vol. 31, p. 473

Baldwin J., Phillips M., Terlevich R., Classification parameters for the emission-line spectra of extragalactic objects., PASP, 1981, vol. 93, p. 5

Binette L., Wilson A., Storchi-Bergmann T., Excitation and temperature of extended gas in active galaxies. II. Photoionization models with matter-bounded clouds., A&A, 1996, vol. 312, p. 365

Calzetti D., Kinney A. L., Storchi-Bergmann T., Dust Extinction of the Stellar Continua in Starburst Galaxies: The Ultraviolet and Optical Extinction Law, ApJ, 1994, vol. 429, p. 582

Cann J. M., Satyapal S., Abel N. P., Ricci C., Secrest N. J., Blecha L., Gliozzi M., The Hunt for Intermediate-mass Black Holes in the JWST Era , The Astrophysical Journal, 2018, vol. 861, p. 142

Cappellari M., Improving the full spectrum fitting method: accurate convolution with Gauss-Hermite functions, Monthly Notices of the Royal Astronomical Society, 2017, vol. 466, p. 798

Cappellari M., Emsellem E., Parametric Recovery of Line-of-Sight Velocity Distributions from Absorption-Line Spectra of Galaxies via Penalized Likelihood, PASP, 2004, vol. 116, p. 138

Cardelli J. A., Clayton G. C., Mathis J. S., The Relationship between Infrared, Optical, and Ultraviolet Extinction, ApJ, 1989, vol. 345, p. 245

Cerqueira-Campos F. C., Rodríguez-Ardila A., Riffel R., Marinello M., Prieto A., Dahmer-Hahn L. G., Coronal-line forest active galactic nuclei-I. Physical properties of the emission-line regions, Monthly Notices of the Royal Astronomical Society, 2021, vol. 500, p. 2666

Cezar P. H., Steiner J. E., Menezes R. B., Gas kinematics and stellar archaeology of the Seyfert galaxy NGC 5643. In Galaxy Evolution and Feedback across Different Environments , vol. 359, 2021, p. 452

Cid Fernandes R., Mateus A., Sodré L., Stasińska G., Gomes J. M., Semi-empirical analysis of Sloan Digital Sky Survey galaxies – I. Spectral synthesis method, Monthly Notices of the Royal Astronomical Society, 2005, vol. 358, p. 363

Cid Fernandes R., Stasińska G., Schlickmann M. S., Mateus A., Vale Asari N., Schoenell W., Sodré L., Alternative diagnostic diagrams and the 'forgotten' population of weak line galaxies in the SDSS, Monthly Notices of the Royal Astronomical Society, 2010, vol. 403, p. 1036

Cresci G., Marconi A., Zibetti S., Risaliti G., Carniani S., Mannucci F., Gallazzi A., Maiolino R., Balmaverde B., Brusa M., Capetti A., Cicone C., Feruglio C., Bland-Hawthorn J., Nagao T., Oliva E., Salvato M., Sani E., Tozzi P., Urrutia T., Venturi G., The MAGNUM survey: positive feedback in the nuclear region of NGC 5643 suggested by MUSE, A&A, 2015, vol. 582, p. A63

Davies R. I., Maciejewski W., Hicks E. K. S., Emsellem E., Erwin P., Burtscher L., Dumas G., Lin M., Malkan M. A., Müller-Sánchez F., Orban de Xivry G., Rosario D. J., Schnorr-Müller A., Tran A., Fueling Active Galactic Nuclei. II. Spatially Resolved Molecular Inflows and Outflows, The Astrophysical Journal, 2014, vol. 792, p. 101

da Silva P., Menezes R. B., Steiner J. E., The nuclear region of NGC 613 – I. Multiwavelength analysis, Monthly Notices of the Royal Astronomical Society, 2020, vol. 492, p. 5121

Dopita M. A., Vogt F. P. A., Sutherland R. S., Seitenzahl I. R., Ruiter A. J., Ghavamian P., Shocked Interstellar Clouds and Dust Grain Destruction in the LMC Supernova Remnant N132D, The Astrophysical Journal Supplement Series, 2018, vol. 237, p. 10

Dors O. L., Maiolino R., Cardaci M. V., Hägele G. F., Krabbe A. C., Pérez-Montero E., Armah M., Chemical abundances of Seyfert 2 AGNs – III. Reducing the oxygen abundance discrepancy, Monthly Notices of the Royal Astronomical Society, 2020, vol. 496, p. 3209

Fabbiano G., Paggi A., Siemiginowska A., Elvis M., Chandra Detection of the Circumnuclear Molecular Torus of the Compton-thick Active Galactic Nucleus in NGC 5643, ApJ, 2018, vol. 869, p. L36

Fabian A. C., Observational Evidence of AGN Feedback, 2012

Fischer T. C., Crenshaw D. M., Kraemer S. B., Schmitt H. R., Determining Inclinations of Active Galactic Nuclei via their Narrow-line Region Kinematics. I. Observational Results, ApJS, 2013, vol. 209, p. 1

Fonseca-Faria M. A., Rodríguez-Ardila A., Contini M., Reynaldi V., The ionized gas outflow in the Circinus galaxy: kinematics and physical conditions, Monthly Notices of the Royal Astronomical Society, 2021, vol. 506, p. 3831

Freund J., How many spectral lines are statistically significant?, Annalen der Physik, 1992, vol. 504, p. 380

García-Bernete I., Alonso-Herrero A., García-Burillo S., Pereira-Santaella M., García-Lorenzo B., Carrera F. J., Rigopoulou D., Ramos Almeida C., Villar Martín M., González-Martín O., Hicks E. K., Labiano A., Ricci C., Mateos S., Multiphase feedback processes in the Sy2 galaxy NGC 5643, Astronomy and Astrophysics, 2021, vol. 645, p. 1

Gonzalez R. C., Digital image processing. Pearson education india, 2009

Goulding A. D., Alexander D. M., Lehmer B. D., Mullaney J. R., Towards a complete census of active galactic nuclei in nearby galaxies: the incidence of growing black holes, Monthly Notices of the Royal Astronomical Society, 2010, vol. 406, p. 597

Guainazzi M., Rodriguez-Pascual P., Fabian A. C., Iwasawa K., Matt G., Unveiling the nature of the highly obscured active galactic nucleus in NGC 5643 with XMM-Newton, Monthly Notices of the Royal Astronomical Society, 2004, vol. 355, p. 297

Guolo-Pereira M., Ruschel-Dutra D., Storchi-Bergmann T., Schnorr-Müller A., Cid Fernandes R., Couto G., Dametto N., Hernandez-Jimenez J. A., Exploring the AGN-merger connection in Arp 245 I: Nuclear star formation and gas outflow in NGC 2992, MNRAS, 2021, vol. 502, p. 3618

Harrison C. M., , 2016 Integral Field Spectroscopy and Spectral Energy Distributions. Springer International Publishing Cham pp 37–46

Heckman T. M., Best P. N., The coevolution of galaxies and supermassive black holes: Insights from surveys of the contemporary universe, Annual Review of Astronomy and Astrophysics, 2014, vol. 52, p. 589

Hickox R. C., Alexander D. M., Obscured Active Galactic Nuclei, Annual Review of Astronomy and Astrophysics, 2018, vol. 56, p. 625

Hicks E. K. S., Davies R. I., Maciejewski W., Emsellem E., Malkan M. A., Dumas G., Müller-Sánchez F., Rivers A., Fueling Active Galactic Nuclei. I. How the Global Characteristics of the Central Kiloparsec of Seyferts Differ from Quiescent Galaxies, The Astrophysical Journal, 2013, vol. 768, p. 107

Ho L. C., Nuclear activity in nearby galaxies., ARA&A, 2008, vol. 46, p. 475

Ho L. C., Radiatively Inefficient Accretion in Nearby Galaxies, ApJ, 2009, vol. 699, p. 626

Ho L. C., Filippenko A. V., Sargent W. L. W., A Reevaluation of the Excitation Mechanism of LINERs, ApJ, 1993, vol. 417, p. 63

Ho L. C., Li Z.-Y., Barth A. J., Seigar M. S., Peng C. Y., The Carnegie-Irvine Galaxy Survey. I. Overview and Atlas of Optical Images, ApJS, 2011, vol. 197, p. 21

Jones M. L., Parker K., Fabbiano G., Elvis M., Maksym W. P., Paggi A., Ma J., Karovska M., Siemiginowska A., Wang J., Extended X-Ray Emission in Compton Thick AGN with Deep Chandra Observations, ApJ, 2021, vol. 910, p. 19

Kauffmann G., Heckman T. M., Tremonti C., Brinchmann J., Charlot S., White S. D. M., Ridgway S. E., Brinkmann J., Fukugita M., Hall P. B., Ivezić Ž., Richards G. T., Schneider D. P., The host galaxies of active galactic nuclei, MNRAS, 2003, vol. 346, p. 1055

Kewley L. J., Dopita M. A., Sutherland R. S., Heisler C. A., Trevena J., Theoretical Modeling of Starburst Galaxies, ApJ, 2001, vol. 556, p. 121

Kewley L. J., Groves B., Kauffmann G., Heckman T., The host galaxies and classification of active galactic nuclei, MNRAS, 2006, vol. 372, p. 961

Kewley L. J., Nicholls D. C., Sutherland R. S., Understanding Galaxy Evolution through Emission Lines, Annual Review of Astronomy and Astrophysics, 2019, vol. 57, p. 511

Khachikian E. Y., Weedman D. W., An atlas of Seyfert galaxies., ApJ, 1974, vol. 192, p. 581

Kramida A., Yu. Ralchenko Reader J., and NIST ASD Team, 2020 NIST Atomic Spectra Database (ver. 5.8), [Online]. Available: `https://physics.nist.gov/asd` [2017, April 9]. National Institute of Standards and Technology, Gaithersburg, MD.

Leipski C., Falcke H., Bennert N., Hüttemeister S., The radio structure of radio-quiet quasars, Astronomy and Astrophysics, 2006, vol. 455, p. 161

Lucy L. B., An iterative technique for the rectification of observed distributions, AJ, 1974, vol. 79, p. 745

Luridiana V., Morisset C., Shaw R. A., PyNeb: A new tool for analyzing emission lines: I. Code description and validation of results, Astronomy and Astrophysics, 2015, vol. 573

Ma J., Maksym W. P., Fabbiano G., Elvis M., Storchi-Bergmann T., Karovska M., Wang J., Travascio A., Spatially Resolved BPT Mapping of Nearby Seyfert 2 Galaxies, ApJ, 2021, vol. 908, p. 155

Martini P., Regan M. W., Mulchaey J. S., Pogge R. W., Circumnuclear Dust in Nearby Active and Inactive Galaxies. I. Data, The Astrophysical Journal Supplement Series, 2003, vol. 146, p. 353

Matt G., Bianchi S., Marinucci A., Guainazzi M., Iwawasa K., Jimenez Bailon E., X-ray observations of the Compton-thick Seyfert 2 galaxy, NGC 5643, Astronomy and Astrophysics, 2013, vol. 556

May D., Rodríguez-Ardila A., Prieto M. A., Fernández-Ontiveros J. A., Diaz Y., Mazzalay X., Powerful mechanical-driven outflows in the central parsecs of the low-luminosity active galactic nucleus ESO 428-G14, Monthly Notices of the Royal Astronomical Society: Letters, 2018, vol. 481, p. L105

May D., Steiner J. E., A two-stage outflow in ngc 1068, Monthly Notices of the Royal Astronomical Society, 2017, vol. 469, p. 994

Mazzalay X., Rodríguez-Ardila A., Komossa S., Demystifying the coronal-line region of active galactic nuclei: spatially resolved spectroscopy with the Hubble Space Telescope, MNRAS, 2010, vol. 405, p. 1315

Menezes R. B., Espectroscopia 3D de núcleos ativos de galáxias: tratamento e análise de dados no óptico e infravermelho próximo, Universidade de São Paulo, 2012, Ph.D. Thesis

Menezes R. B., da Silva P., Ricci T. V., Steiner J. E., May D., Borges B. W., A treatment procedure for VLT/SINFONI data cubes: application to NGC 5643, Monthly Notices of the Royal Astronomical Society, 2015, vol. 450, p. 369

Menezes R. B., Ricci T. V., Steiner J. E., da Silva P., Ferrari F., Borges B. W., A treatment procedure for GMOS/IFU data cubes: application to NGC 2835, MNRAS, 2019, vol. 483, p. 3700

Menezes R. B., Steiner J. E., Ricci T. V., A treatment procedure for Gemini North/NIFS data cubes: application to NGC 4151, MNRAS, 2014, vol. 438, p. 2597

Menezes R. B., Steiner J. E., Ricci T. V., da Silva P., Nicolazzi D. M., First results of the DIVING^{3D} survey of bright galaxies in the local universe: The mini-DIVING^{3D} sample. In Galaxy Evolution and Feedback across Different Environments , vol. 359, 2021, p. 450

Mingozzi M., Cresci G., Venturi G., Marconi A., Mannucci F., Perna M., Belfiore F., Carniani S., Balmaverde B., Brusa M., Cicone C., Feruglio C., Gallazzi A., Mainieri V., Maiolino R., Nagao T., Nardini E., Sani E., Tozzi P., Zibetti S., The MAGNUM survey: different gas properties in the outflowing and disc components in nearby active galaxies with MUSE, A&A, 2019, vol. 622, p. A146

Moneti A., Ramo J., The Astrophysical Journal , 549:L203–L207, 2001 March 10 2001., 2001, pp 179–182

Morganti R., Oosterloo T., Raymond Oonk J. B., Frieswijk W., Tadhunter C., The fast molecular outflow in the Seyfert galaxy IC 5063 as seen by ALMA, Astronomy and Astrophysics, 2015, vol. 580

Morris S., Ward M., Whittle M., Wilson A. S., Taylor K., The velocity fields and radio structures of the active galaxies NGC 5643 and NGC 7582, Monthly Notices of the Royal Astronomical Society, 1985, vol. 216, p. 193

Morris S. L., Ward M. J., Spectrophotometry of active galaxies - I. The observations, Monthly Notices of the Royal Astronomical Society, 1988, vol. 230, p. 639

Negus J., Comerford J. M., Sánchez F. M., Barrera-Ballesteros J. K., Drory N., Rembold S. B., Riffel R. A., The Physics of the Coronal Line Region for Galaxies in MaNGA, 2021

Netzer H., The Physics and Evolution of Active Galactic Nuclei. Cambridge University Press, 2013

Netzer H., The Physics and Evolution of Active Galactic Nuclei. Cambridge University Press, 2013

Netzer H., , 2015 Revisiting the unified model of active galactic nuclei

Nurnberger D. Kaufer A. D. C., , 2011 Technical report Very Large Telescope - SINFONI - User Manual

Osterbrock D. E., Ferland G. J., Astrophysics of gaseous nebulae and active galactic nuclei, 2006

Padovani P., Alexander D. M., Assef R. J., De Marco B., Giommi P., Hickox R. C., Richards G. T., Smolčić V., Hatziminaoglou E., Mainieri V., Salvato M., , 2017 Active galactic nuclei: what's in a name?

Peterson B. M., An Introduction to Active Galactic Nuclei, 1997

Phillips M. M., Jenkins C. R., Dopita M. A., Sadler E. M., Binette L., Ionized gas in elliptical and SO galaxies. I. A survey for H alpha and N II emission., AJ, 1986, vol. 91, p. 1062

Ricci C., Trakhtenbrot B., Koss M. J., Ueda Y., Del Vecchio I., Treister E., Schawinski K., Paltani S., Oh K., Lamperti I., Berney S., Gandhi P., Ichikawa K., Bauer F. E., Ho L. C., Asmus D., Beckmann V., Soldi S., Baloković M., Gehrels N., Markwardt C. B., BAT AGN Spectroscopic Survey. V. X-Ray Properties of the Swift/BAT 70-month AGN Catalog, ApJS, 2017, vol. 233, p. 17

Ricci T. V., Análise da emissão nuclear e circumnuclear de gás de uma amostra de 10 galáxias elípticas e lenticulares, Universidade de São Paulo, 2013, Ph.D. Thesis

Ricci T. V., Steiner J. E., Menezes R. B., Bergmann T. S., Forman W., Overzier R., Riffel R., The DIVING3DProject: Analysis of the nuclear region of Early-type Galaxies, Proceedings of the International Astronomical Union, 2021, pp 454–456

Richardson W. H., Bayesian-Based Iterative Method of Image Restoration, Journal of the Optical Society of America (1917-1983), 1972, vol. 62, p. 55

Riffel R. A., Bianchin M., Riffel R., Storchi-Bergmann T., Schönell A. J., Dahmer-Hahn L. G., Dametto N. Z., Diniz M. R., Gemini NIFS survey of feeding and feedback in nearby active galaxies – IV. Excitation, Monthly Notices of the Royal Astronomical Society, 2021, vol. 503, p. 5161

Riffel R. A., Dors O. L., Armah M., Storchi-Bergmann T., Feltre A., Hägele G. F., Cardaci M. V., Ruschel-Dutra D., Krabbe A. C., Pérez-Montero E., Zakamska N. L., Freitas I. C., Chemical abundances in Seyfert galaxies - V. The discovery of shocked emission outside the AGN ionization axis, MNRAS, 2021, vol. 501, p. L54

Riffel R. A., Hekatelyne C., Freitas I. C., Outflows in the Seyfert 2 galaxy NGC 5643 traced by the [S iii] emission, Publications of the Astronomical Society of Australia, 2018, vol. 35, p. e040

Rodríguez-Ardila A., Fonseca-Faria M. A., Kiloparsec-scale jet-driven feedback in AGN probed by highly ionized gas: A MUSE/VLT perspective, Proceedings of the International Astronomical Union, 2021, pp 221–225

Rodríguez-Ardila A., Prieto M. A., Portilla J. G., Tejeiro J. M., The near-infrared coronal line spectrum of 54 nearby active galactic nuclei, Astrophysical Journal, 2011, vol. 743

Rose M., Elvis M., Tadhunter C. N., Coronal-line forest AGN: The best view of the inner edge of the AGN torus?, Monthly Notices of the Royal Astronomical Society, 2015, vol. 448, p. 2900

Ruschel-Dutra D., de Oliveira B. D., , 2020a danielrd6/ifscube: Modeling

Ruschel-Dutra D., de Oliveira B. D., , 2020b danielrd6/ifscube v1.0

Rybicki G. B., Lightman A. P., Radiative processes in astrophysics, 1979

Schmitt H. R., Storchi-Bergmann T., Baldwin J. A., Anisotropic High-Excitation Emission and Chemical Abundances in the Seyfert 2 Galaxy NGC 5643, The Astrophysical Journal, 1994, vol. 423, p. 237

Shen Q., Faraway J., AN F TEST FOR LINEAR MODELS WITH FUNCTIONAL RESPONSES, Statistica Sinica, 2004, vol. 14, p. 1239

Simpson C., Wilson A. S., Bower G., Heckman T. M., Krolik J. H., Miley G. K., A One-sided Ionization Cone in the Seyfert 2 Galaxy NGC 5643, The Astrophysical Journal, 1997, vol. 474, p. 121

Singh R., van de Ven G., Jahnke K., Lyubenova M., Falcón-Barroso J., Alves J., Cid Fernandes R., Galbany L., García-Benito R., Husemann B., Kennicutt R. C., Marino R. A., Márquez I., Masegosa J., Mast D., Pasquali A., Sánchez S. F., Walcher J., Wild V., Wisotzki L., Ziegler B., The nature of LINER galaxies:, Astronomy Astrophysics, 2013

Smith R. C., Astrophysical Techniques, Sixth Edition, by C.R.Kitchin. vol. 55, 2014, 359

Steiner J. E., Menezes R. B., Ricci T. V., da Silva P., Cid Fernandes R., Vale Asari N., Carvalho M. S., May D., Coelho P. R. T., de Amorim A. L., The DIVING3D survey – Deep Integral Field Spectrograph View of Nuclei of Galaxies – I. Definition and sample presentation, Monthly Notices of the Royal Astronomical Society, 2022, vol. 510, p. 5780

Steiner J. E., Menezes R. B., Ricci T. V., DIVING^{3D} Team The DIVING^{3D} Survey - Deep IFS View of Nuclei of Galaxies. In Galaxy Evolution and Feedback across Different Environments , vol. 359, 2021, p. 402

Steiner J. E., Menezes R. B., Ricci T. V., Oliveira A. S., Mapping low- and high-density clouds in astrophysical nebulae by imaging forbidden line emission, MNRAS, 2009, vol. 396, p. 788

Steiner J. E., Menezes R. B., Ricci T. V., Oliveira A. S., PCA Tomography: How to extract information from data cubes, Monthly Notices of the Royal Astronomical Society, 2009, vol. 395, p. 64

Taylor J., Introduction to Error Analysis, the Study of Uncertainties in Physical Measurements, 2nd Edition, 1997

Tully R. B., Fisher J. R., Catalog of Nearby Galaxies, 1988

van Dokkum P. G., Cosmic-Ray Rejection by Laplacian Edge Detection, Publications of the Astronomical Society of the Pacific, 2001, vol. 113, p. 1420

Van Hoof P. A. M., Recent Development of the Atomic Line List, Galaxies, 2018, vol. 6

Vazdekis A., Sánchez-Blázquez P., Falcón-Barroso J., Cenarro A. J., Beasley M. A., Cardiel N., Gorgas J., Peletier R. F., Evolutionary stellar population synthesis with MILES - I. The base models and a new line index system, Monthly Notices of the Royal Astronomical Society, 2010, vol. 404, p. 1639

Veilleux S., A Study of the Structure and Kinematics of the Narrow-Line Region in Seyfert Galaxies. III. Individual Objects, ApJ, 1991, vol. 369, p. 331

Veilleux S., Cecil G., Bland-Hawthorn J., Galactic Winds, Annual Review of Astronomy and Astrophysics, 2005, vol. 43, p. 769

Veilleux S., Osterbrock D. E., Spectral Classification of Emission-Line Galaxies, ApJS, 1987, vol. 63, p. 295

Venturi G., Cresci G., Marconi A., Mingozzi M., Nardini E., Carniani S., Mannucci F., Marasco A., Maiolino R., Perna M., Treister E., Bland-Hawthorn J., Gallimore J., MAGNUM survey: Compact jets causing large turmoil in galaxies. Enhanced line widths perpendicular to radio jets as tracers of jet-ISM interaction, A&A, 2021, vol. 648, p. A17

Véron-Cetty M. P., Véron P., A catalogue of quasars and active nuclei: 13th edition, A&A, 2010, vol. 518, p. A10

Westmoquette M. S., Exter K. M., Christensen L., Maier M., Lemoine-Busserolle M., Turner J., Marquart T., The integral field spectroscopy (IFS) wiki, 2009

Winge C., Riffel R. A., Storchi-Bergmann T., The Gemini Spectral Library of Near-IR Late-Type Stellar Templates and Its Application for Velocity Dispersion Measurements, The Astrophysical Journal Supplement, 2009, vol. 185, p. 186

Yang X., Shen Q., Xu H., Shoptaw S., Functional regression analysis using an F test for longitudinal data with large numbers of repeated measures, Statistics in Medicine, 2007, vol. 26, p. 1552

York D. G., Adelman J., John E. Anderson J., Anderson S. F., Annis J., Bahcall N. A., Bakken J. A., Barkhouser R., Bastian S., Berman E., Boroski W. N., Bracker S., Briegel C., Briggs J. W., Brinkmann J., Brunner R., Burles S., Carey L., Carr M. A., Castander F. J., Chen B., Colestock P. L., Connolly A. J., Crocker J. H., Csabai I., Czarapata P. C., Davis J. E., Doi M., Dombeck T., Eisenstein D., Ellman N., Elms B. R., Evans M. L., Fan X., , 2000, vol. 120, p. 1579

Appendix

Appendix A

Uncertainties, SNR and Centroid Estimates

A.1 Error Propagation

As output of the code `IFSCUBE` we had amplitude (A), velocity (v), velocity dispersion (σ) and their errors. Additionally, the integrated flux is also given. To estimate the flux errors and propagate the error for other relevant physical measurements, we summarize the procedure adopted in the following lines.

Considering the function $F(x_1, x_2, x_3, ..., x_N)$ with independent variables, the standard error propagation equation (Taylor, 1997) is :

$$\delta_F^2 = \sum_{i=1}^{N} \left(\frac{\partial F}{\partial x_i} \sigma_{x_i} \right)^2 \tag{A.1}$$

The uncertainty in the flux of a Gaussian considering that $Area_{Gaussian} = A\sqrt{2\pi}\sigma(\AA)$, is:

$$\delta_F = \sqrt{2\pi[(\sigma\delta_A)^2 + (A\delta_\sigma)^2]} \tag{A.2}$$

For the case of two gaussian components the uncertainty becomes $\delta_{F+} = \sqrt{\delta_{F_1}^2 + \delta_{F_2}^2}$. For the extinction corrected fluxes of section 2.2.2, $F_{\lambda 0} = F_\lambda \cdot 10^{cf(\lambda)}$, the propagated errors are :

$$\delta_{F_{\lambda 0}} = \sqrt{\left(\frac{\partial F_{\lambda 0}}{\partial F_\lambda} \delta_{F_\lambda} \right)^2 + \left(\frac{\partial F_{\lambda 0}}{\partial c} \delta_c \right)^2} = \sqrt{10^{2cf(\lambda)} \left\{ \delta_{F_\lambda}^2 + \left[\left(\frac{F_\lambda f(\lambda)}{f(H\alpha) - f(H\beta)} \right)^2 \left(\frac{\delta_{H\alpha}^2}{H\alpha^2} + \frac{\delta_{H\beta}^2}{H\beta^2} \right) \right] \right\}} \tag{A.3}$$

Given the distance modulus of NGC 5643 as $\mu = (m - M) = 31 \pm 1$ magnitude implies a distance of $d \pm \delta d \approx 16 \pm 7$ Mpc. From that we can calculate the overall luminosity. Considering a circle of infinitesimal thickness, subtending an solid angle $w = 2\pi$, the luminosity is given by $L_\lambda \approx 2\pi d^2 F_{\lambda 0}$. The error in their determination is them :

$$\delta_{L_\lambda} = 2\pi d\sqrt{(d\delta_{F_{\lambda 0}})^2 + (2F_{\lambda 0}\delta_d)^2} \tag{A.4}$$

A.2 SNR Estimates

For channel maps, the SNR, as shown in figure A.1 was estimated as follows. The procedure used the pure emission line and stellar data cubes. A wavelength window, often with at least 40 spectral pixels, is defined closer to the emission line. The region in question cannot have strong emissions or absorptions in the data cubes. Then in this wavelength window is taken the average of the stellar spectra for each spaxel and considered as the signal. In the pure emission lines, the standard deviation of the window closer to the emission line is taken to estimate the noise. Finally, the ratio between the estimated signal and noise for each spaxel is taken. The threshold adopted for channels was that spaxels with SNR < 10 should be masked.

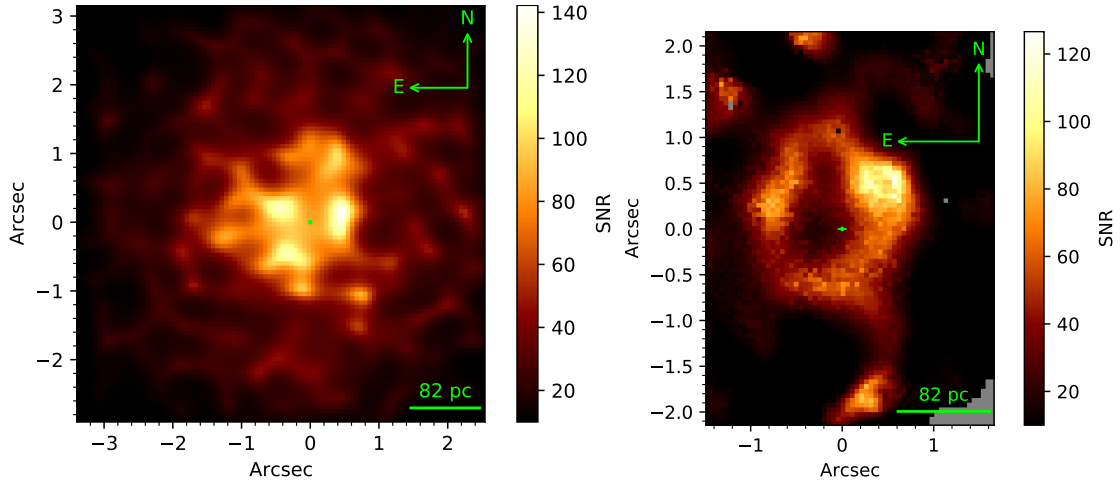

Figure A.1: Examples of SNR maps adopted to mask channel maps for the emission lines of H_2 λ21218 and [OIII]λ 5007.

For the integrated fluxes, the spaxels used were selected based on the uncertainties of the emission line fitting. The threshold adopted was that spaxels with $F/\delta F < 3$ were masked following the procedure presented on Phillips et al. (1986).

A.3 F-test

An additional procedure was made for the spectra extractions. To evaluate if there are required more Gaussian components for the fits, an f-test was implemented. A

similar procedure was adopted in Guolo-Pereira et al. (2021). Freund (1992) applied the test for spectral lines fitting when adding a second Gaussian component or more 3 degrees of freedom. From the test result, when F exceeds the F-table under some probability level p, we can say that the addition of a secondary Gaussian is statistically significant with a probability p. We adopt p = 99.9% or higher for the fits considered, which means 1/1000 or less the chance of not being a real second component.

In our case, we need more free parameters since we fitted, in some cases, many emission lines at the same time. The equation to compare two models of a generic number of degrees of freedom was given in Shen and Faraway (2004); Yang et al. (2007) and can be written as:

$$F = \frac{\chi^2_{red1} - \chi^2_{red2}/(p-q)}{\chi^2_{red2}/(n-p)} \tag{A.5}$$

Where the $\chi^2_{\rm redx}$ is the reduced chi-squared of the x model, p and q the degrees of freedom of models 1 and 2, and n the number of the observation data points. An example of fit for $H\alpha$ is given in figure A.2. For all strong emission lines, at least two components were required across all the FoV. An exception was for [Fe VII]λ6086, that while presenting many regions in outflow, some extractions did not require an additional component.

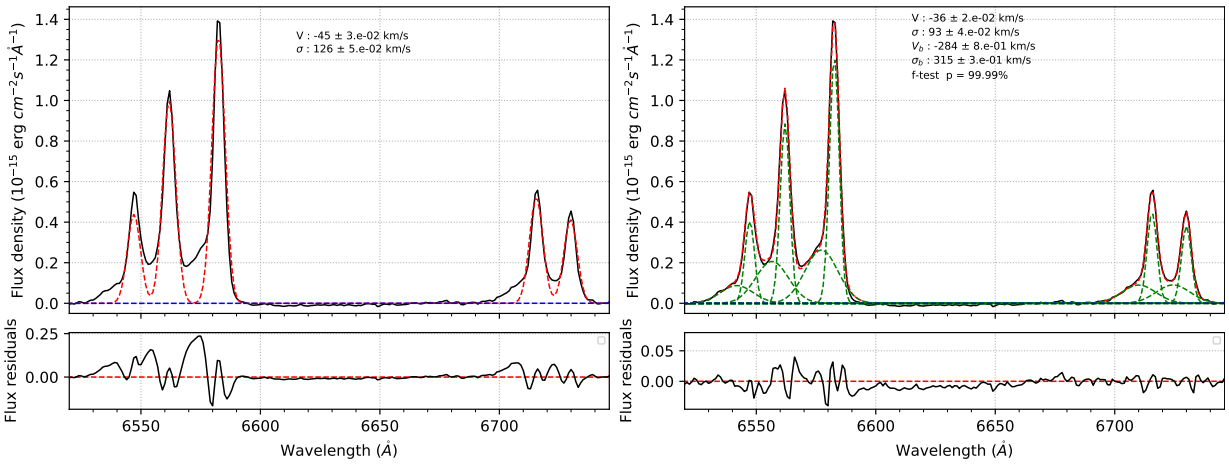

Figure A.2: Example of spectra extractions fit. On the right is a simple fit, and on the right are the two Gaussian components. There is a statistically significant need for the second component. The extraction comes from the $PA = 128°$ at an average distance of $1.32''$ from the nucleus.

A.4 Centroid Determination and Spatial Resolution

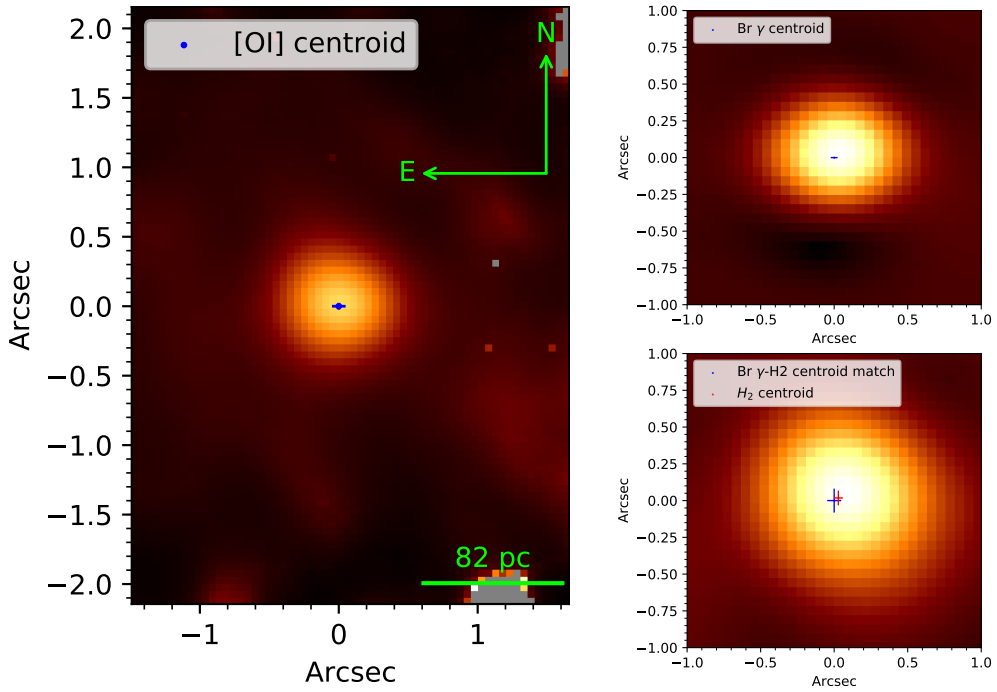

Figure A.3: Emission line maps of [OI]λ6300, Brγ and $H_2\lambda$17480. The central peak and uncertainty are marked as a blue dot and cross. The red dot marks the $H_2\lambda$17480 peaks in the H-band. The corresponding H-band center was found based on the K-band $H_2\lambda$ 21218 peaks.

The peak emission of specific lines was measured to find the centroid and match between the different data cubes. The peak of [OI]λ6300 in the optical and Brγ in the K-band was measured. To find the equivalent center on the H-band, a match between the peaks of H_2 λ 21218 and H_2 λ17480, from K and H-bands, was obtained. The positions are shown in figure A.3. All the measurements were performed in emission line channels maps, considering their standard deviation to estimate the position uncertainty.

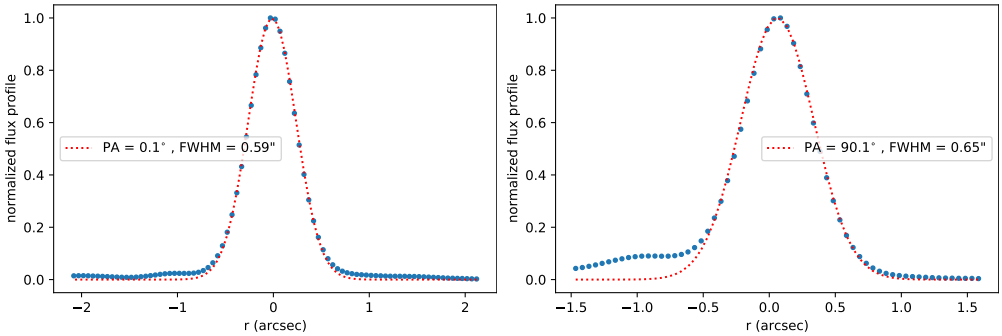

Figure A.4: [Fe VII]λ6086 profiles across PA = 0.1° and PA = 90.1°. The Gaussian fits indicate FWHM = 0.59″ and FWHM = 0.65″.

Gaussian fits were applied to the spatial profile of some emission lines to obtain estimates of each data cube spatial resolution. In the optical data cube, the coronal line [Fe VII]λ6086 was used since their emission is often more concentrated in the nuclear region. For the H and K-band, the Brγ and Br_{10} was considered. A code was written to extract the spatial profile of the lines under 24 different PA between 0.1°-172.6°. Each profile was fitted with a Gaussian, and their FWHM was measured. We find for the optical data cube FWHM([Fe VII]λ6086) = $0.62'' \pm 0.02''$. For K and H-band the values of FWHM(Brγ) = $0.46'' \pm 0.04''$ and FWHM(Br_{10}) = $0.56'' \pm 0.06''$. The spatial resolution estimates are probably an upper limit since the code also included regions where the lines are possibly extended, as shown in figure A.4 the PA = 90.1° show emission extended across the east ionization cone.

Appendix B

Stellar Populations and Kinematics

Stellar archaeology

The stellar population synthesis was made for the nuclear and circumnuclear spectra shown in figure B.1. Further details can be found in the section 2.2.1.

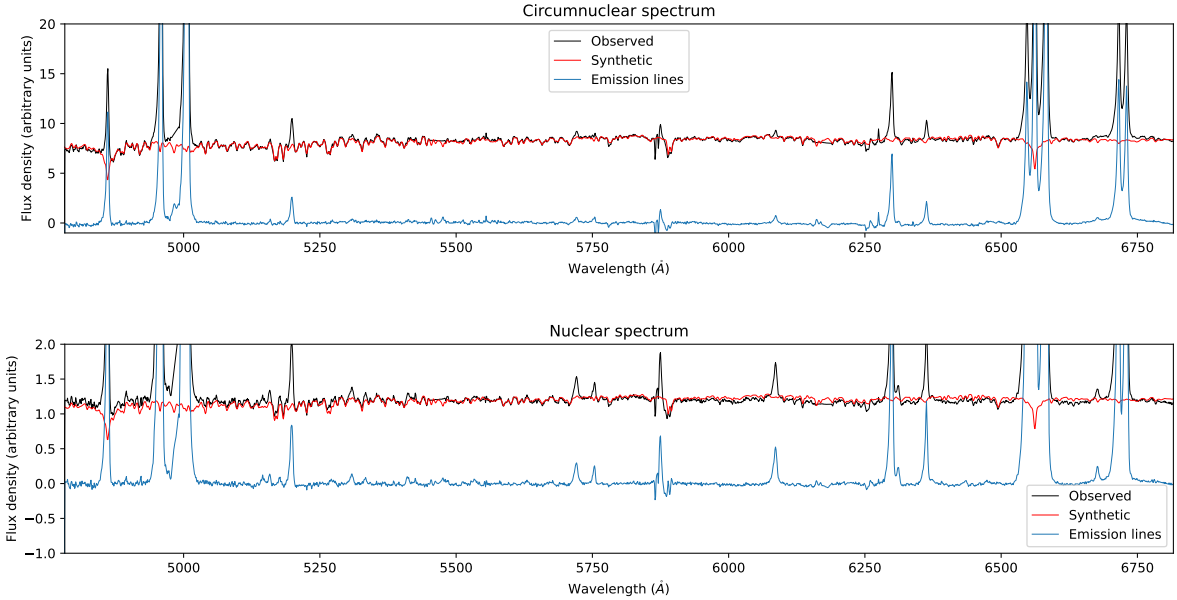

Figure B.1: Nuclear (bottom) and circumnuclear (top) observed spectra (black line) from GMOS data cube. The synthesis fit (red line) and the pure emission line spectra (blue line) are shown for both regions.

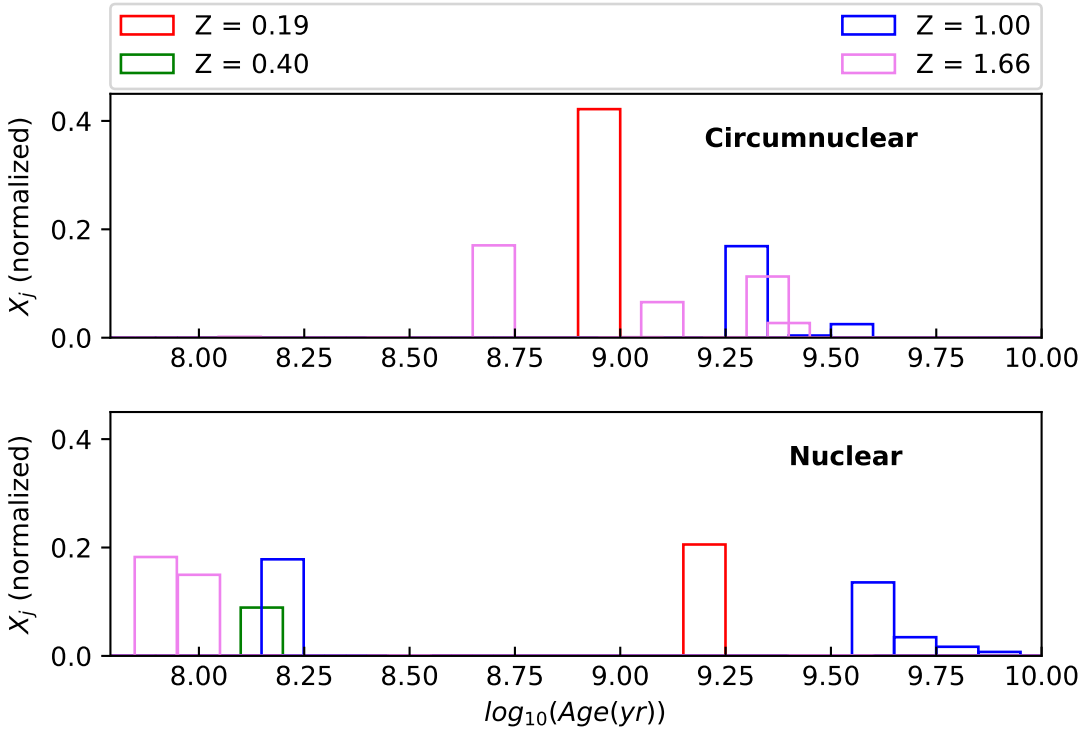

Figure B.2: Star formation history for the nuclear and circumnuclear spectra. The colors represent the metallicity of the stellar population as indicated in solar units at the top panel. The light fraction contribution of each SSP to the stellar spectra is indicated in the vertical axis X_j.

Figure B.2 shows a histogram containing the flux fractions for each stellar population detected in the spectral synthesis, which reveals the star formation history (SFH) of the nuclear and circumnuclear regions of NGC 5643. The circumnuclear region does not present star formation in the last 500 Myr. Another result shows that such a region does not have flux fractions attributed to populations older than 3.5 Gyrs. In contrast, results for the nuclear region show a 20% contribution of older SSPs between ages 3.5 Gyr $\leq t \leq$ 8 Gyr. Another contrast against the circumnuclear spectra is the high contribution of young stars in the nucleus. Around 60% of the flux of that region comes from stars younger than 320 Myr. Both regions, however, also exhibit a low metallicity stellar population (red bar), whose contributions were 40% and 20% for the circumnuclear and nuclear regions. The events are closer in time, occurring around 1.6 Gyr in the nucleus and 900 Myr ago in the circumnuclear region. Towards the circumnuclear region, this population at 900 Myr dominated the flux, while the populations are more diverse in the nucleus.

Stellar kinematics

The stellar kinematics in the optical and NIR K-band were modeled with Gauss-Hermite

functions, using the code pPXF. Further details can be found in section 2.2.1. The results are presented in figures B.3 and B.4. Regions with SNR < 10 were masked according to the procedure described in appendix A.2.

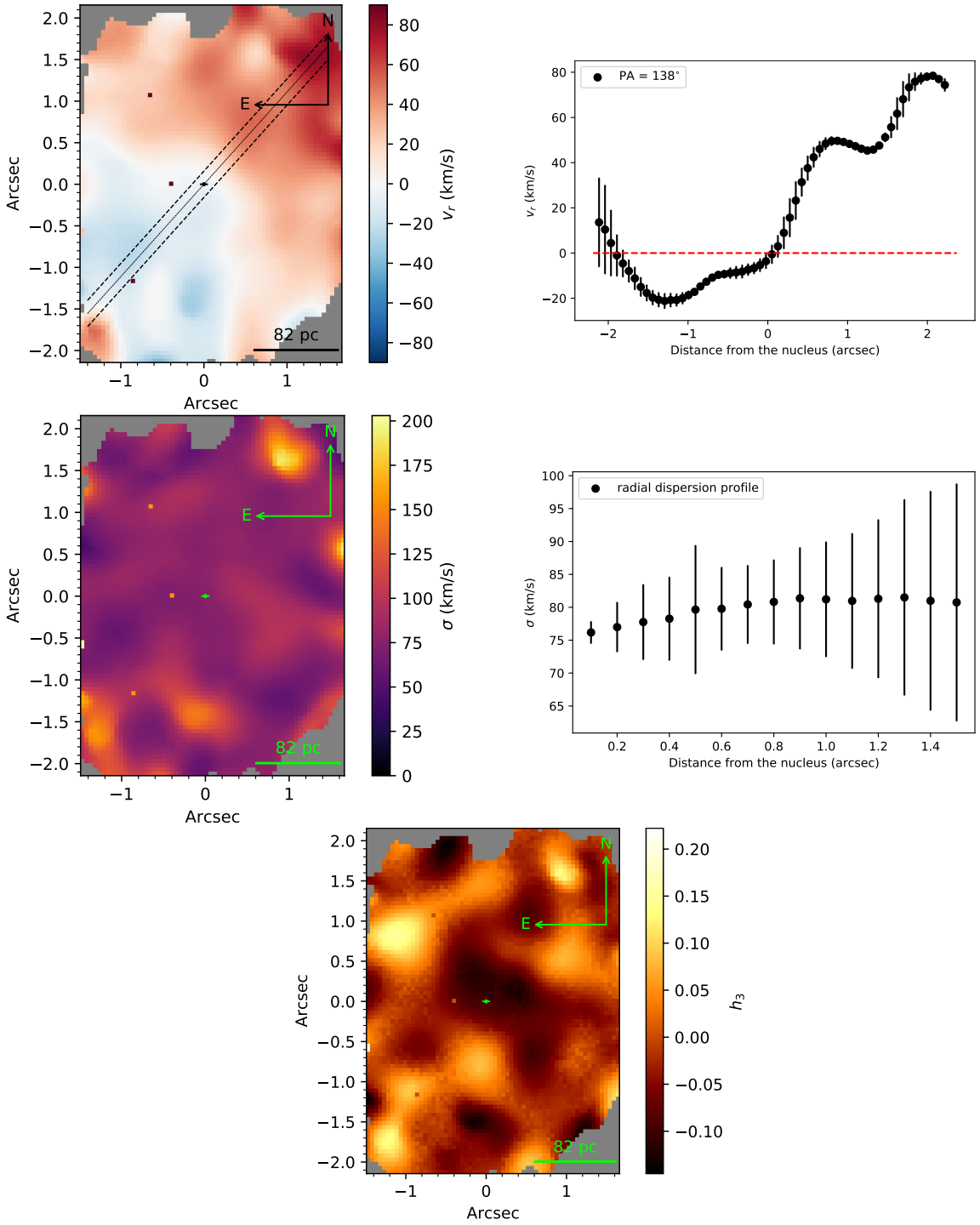

Figure B.3: Results obtained with the pPXF from the optical data cube. The top panel shows the measured projected velocities and their profile along PA = 138°. The central PA = 138° line segment is indicated in the map as a black line. The more distant parallel profiles taken are indicated as dashed lines. In the center is exhibit the stellar velocity dispersion map and its radial profile. The bottom map shows the h_3 coefficient. Low SNR spaxels were masked.

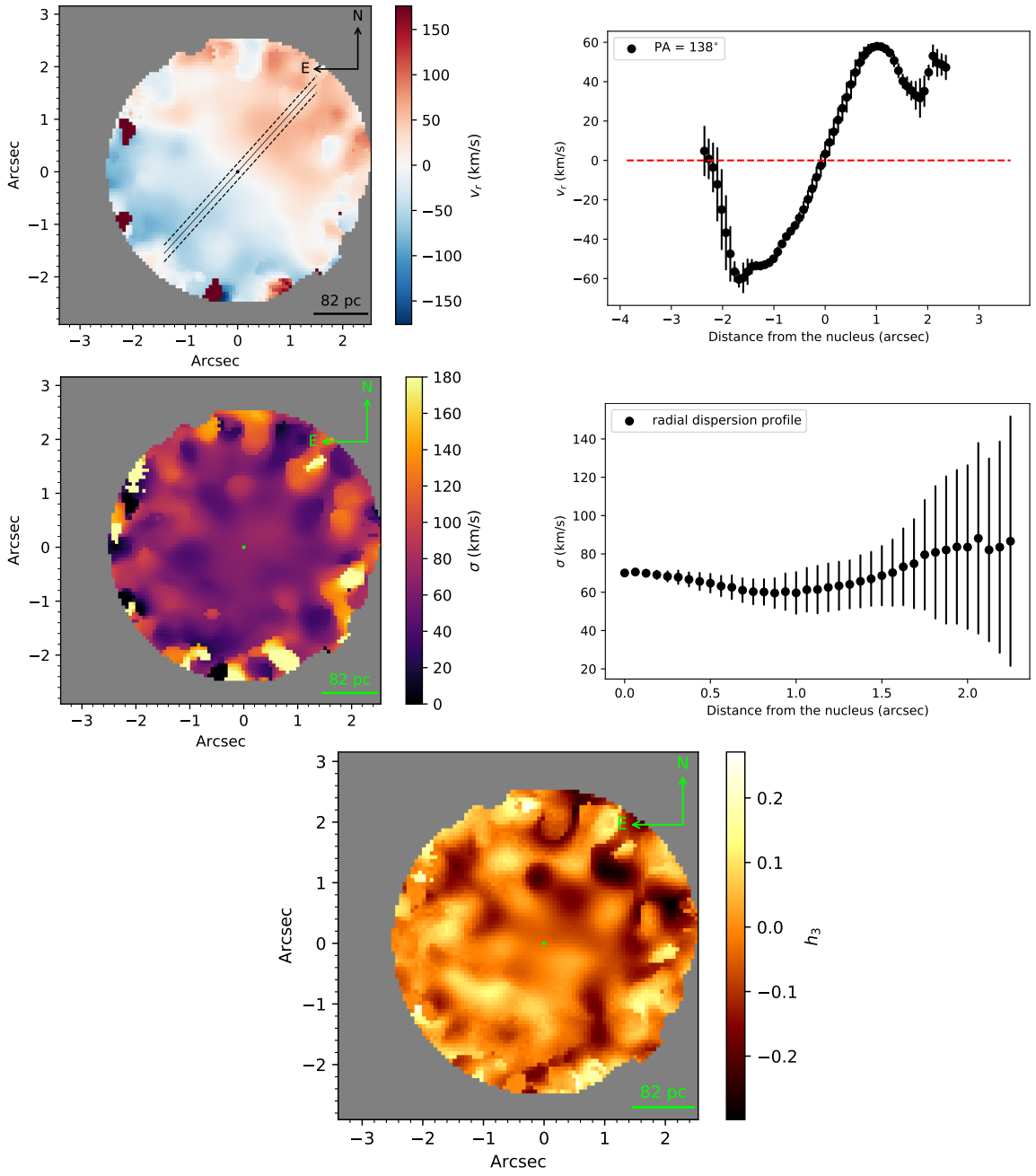

Figure B.4: The same information of figure B.3 for the NIR H-band data cube.

For each obtained map from the spectral synthesis, profiles along the PA = 138° (velocity) and a radial profile (stellar velocity dispersion) were made. The velocity profile was made considering the direction perpendicular to the line of zero velocity. The errors were estimated using the other four profiles distinct by one spaxel and parallel to the former. Then, an average profile was computed, and their error bars were obtained from the standard deviation. A similar procedure was adopted for the velocity dispersion. In contrast, the radial profile comes from concentric rings of thickness 0.0625″ (K-band) and

0.1″ (optical).

The optical stellar kinematics results presented in figure B.3 show a stellar rotation disk with a velocity profile -34 km/s $\leq \langle v_r \rangle \leq$ 34 km/s. Higher velocities can be seen northwest of the nucleus, achieving velocities of $\langle v_r \rangle \approx$ 60 km/s. Lower velocities were found 2″ towards the southeast of the nucleus, results also shown in the NIR. There is not an increase of values of stellar velocity dispersion towards the nucleus. The average dispersion computed across the FoV is similar to the average dispersion weighted by an intensity map of the data cube, with $\langle \sigma \rangle \approx$ 70 km/s.

For the K-band the stellar disk exhibit an average velocity profile of -66 km/s $\leq \langle v_r \rangle \leq$ 56 km/s. The average stellar velocity dispersion weigthed by an intensity map of this data cube was $\langle \sigma \rangle \approx$ 80 km/s.